2012

NUMERICAL SIMULATION OF FUEL SPRAYS IN DIESEL ENGINES

Kohei Fukuda
University of Windsor

NUMERICAL SIMULATION OF FUEL SPRAYS IN DIESEL ENGINES

by
Kohei Fukuda

A Thesis
Submitted to the Faculty of Graduates Studies
through Mechanical, Automotive and Material Engineering
in Partial Fulfillment of the Requirements for
the Degree of Master of Applied Science at the
University of Windsor

Windsor, Ontario, Canada
2012

NUMERICAL SIMULATION OF FUEL SPRAYS IN DIESEL ENGINES

by

Kohei Fukuda

APPROVED BY:

_____

Dr. R. Carriveau
Department of Civil and Environmental Engineering

_____

Dr. B. Zhou
Department of Mechanical, Automotive and Material Engineering

_____

Dr. R. Barron, Co-Advisor
Department of Mathematics and Statistics, Department of Mechanical, Automotive and Material Engineering

_____

Dr. R. Balachandar, Co-Advisor
Department of Civil and Environmental Engineering, Department of Mechanical, Automotive and Material Engineering

_____

Dr. V. Stoilov, Chair of Defense
Department of Mechanical, Automotive and Material Engineering

May 16th, 2012

Declaration of Co-Authorship / Previous Publication

I. Co-Authorship Declaration

I hereby declare that this thesis incorporates the outcome of a joint research undertaken in collaboration with A. Ghasemi under the co-supervision of Dr. Barron and Dr. Balachandar. The collaboration is covered in Chapter 2, 3 and 4 of the thesis. In all cases, the key ideas, primary contributions, numerical simulation designs, data analysis and interpretation were performed by the author, and the contribution of co-authors in the associated publications for annual meetings, congress and conference were primarily through the provision of the numerical analysis.

I am aware of the University of Windsor Senate Policy on Authorship and I certify that I have properly acknowledged the contribution of other researchers to my thesis and have obtained written permission from each of the co-authors to include the above materials in my thesis.

I certify that, with the above qualifications, this thesis, and the research to which it refers, is the product of my own work.

II. Declaration of Previous Publication

This thesis includes three original papers that have been previously published/ submitted for publication in peer-reviewed journals and conference proceedings as indicated below:

Thesis Chapter	Publication title/full citation	Publication status
Chapter 2, 3, and 4	Fukuda, K., Ghasemi, A., Barron, R., and Balachandar, R., An Open Cycle Simulation of DI Diesel Engine Flow Field Effect on Spray Processes. SAE Technical Paper 2012-01-0696, 2012.	Published
Chapter 3	Ghasemi, A., Fukuda, K., Balachandar, R., and Barron, R., Numerical Investigation of Spray Characteristics of Diesel Alternative Fuels. SAE Technical Paper 2012-01-1265, 2012.	Published
Chapter 3	Fukuda, K., Barron, R., and Balachandar, R., Numerical Simulation of a Vertical Valve Port Diesel Engine. *Green Auto Power Train 1st Annual General Meeting*, Waterloo, ON, Canada, November, 2010.	Poster presented
Chapter 4	Fukuda, K., Ghasemi, A., Barron, R., and Balachandar, R., Numerical Simulation of a Vertical Valve Port Diesel Engine. *Green Auto Power Train 2nd Annual General Meeting*, Hamilton, ON, Canada, November, 2011.	Poster presented
Chapter 4	Fukuda, K., Barron, R.M., and Balachandar, R., In-Cylinder Flow Analysis with Different Turbulence Models. *20th Annual Conference of the CFD Society of Canada*, CFD2012, Canmore, Alberta, Canada, May, 2012.	Accepted

I certify that I have obtained a written permission from the copyright owners to include the above published materials in my thesis. I certify that the above material describes work completed during my registration as a graduate student at the University of Windsor.

I declare that to the best of my knowledge, my thesis does not infringe upon anyone's copyright nor violate any proprietary rights and that any ideas, techniques, quotations, or any other material from the work of other people included in my thesis, published or otherwise, are fully acknowledged in accordance with the standard referencing practices. Furthermore, to the extent that I have included copyrighted material that surpasses the bounds of fair dealing within the meaning of the Canada Copyright Act, I certify that I have obtained a written permission from the copyright owners to include such material(s) in my thesis.

I declare that this is a true copy of my thesis, including any final revisions, as approved by my thesis committee and the Graduate Studies office, and that this thesis has not been submitted for a higher degree to any other University or Institution.

Abstract

Engine simulations with diesel fuel spray at ultra-high injection pressures ranging from 100 to 300 MPa were conducted in a vertical valve engine geometry using ANSYS FLUENT 13.0. The in-cylinder flow was calculated by RANS models and DES and validated with the experimental data. The fuel spray characteristics such as Sauter mean diameter, spray cone angle, spray tip penetration and fuel/air mixture were studied under the presence of in-cylinder flow. The ultra-high injection pressures assist in the breakup of droplets into smaller size, accelerating atomization, dispersing the spray in a wide cone angle and mixing air/fuel effectively. However, the rate of change in droplet size was reduced by increasing the injection pressure. Also, high air density in the cylinder did not induce the breakup of droplets. The spray simulations failed for the RNG k-ε and standard k-ω models and the issue was found to be the sensitivity to of the calculations to grid size and type in the particle tracking methodology.

Dedication

To my parents, Kimitaka and Yuko Fukuda,
and my brothers, Kota and Koya.

Acknowledgements

This research is funded by the Ontario Ministry of Research and Innovation through the Ontario Research Fund for Research Excellence under the Green Auto Power Train project. This work is also made possible by the facilities of the Shared Hierarchical Academic Research Computing Network (SHARCNET: www.sharcnet.ca) and Compute/Calcul Canada.

I would like to express my thank you to my advisors, Dr. Barron and Dr. Balachandar, for their support, knowledge and input to my thesis work. Without their patience and understanding on the difficulties of this research, I would not have been able to successfully complete it.

I would also like to thank all my colleagues, Aaron Aczel, Shelagh Fackrell, Abbas Ghasemi, Mo Karimi, Ghassan Nasif, Mehrdad Shademan, Ali Salih, James Situ, and Yuanming Yu, for their time and knowledge that they shared during my study, especially Abbas Ghasemi for giving his input to spray modeling.

I would like to extend my thank you to all faculty and staff members of the Department of Mechanical, Automotive and Material Engineering and Faculty of Graduate Studies, and my friends for their help.

Table of Contents

List of Tables

List of Figures

List of Abbreviations, Symbols, Nomenclature

d	Diameter
ε	Dissipation rate
E	Energy
g	Gas Phase (subscript)
k	Turbulence Kinetic Energy/Specific Heat Ratio
l	Liquid Phase (subscript)/Length of Nozzle Hole
L	Liquid Core Length
Λ	Wave Length
μ	Dynamic Viscosity
σ	Surface Tension
ν	Kinematic Viscosity
P	Pressure
ρ	Density
r	Radius
Re	Reynolds Number
t	Time
T	Temperature/Taylor Number
τ	Shear Stress
U	Relative Velocity
ω	Turbulence Frequency or Specific Dissipation Rate
Ω	Wave Growth Rate
We	Weber Number
Z	Ohnesorge Number
ASOI	After Start of Injection
ATDC	After Top Dead Centre
BDC	Bottom Dead Centre
CA	Crank Angle
CFD	Computational Fluid Dynamics
DES	Detached Eddy Simulation
DNS	Direct Numerical Simulation

HCCI	Homogeneous Charge Compression Ignition
INJ	Injector
IVC	Intake Valve Close
IVO	Intake Valve Open
KH-RT	Kelvin-Helmholtz Rayleigh-Taylor
LES	Large Eddy Simulation
NA	Naturally Aspirated
RANS	Reynolds Averaged Navier-Stokes
RNG	Renormalization Group
SMD	Sauter Mean Diameter
TAB	Taylor Analogy Breakup
TDC	Top Dead Centre

Chapter 1. Introduction

The diesel engine is regarded as a thermodynamically efficient engine marketed for automotive use. However, due to the non-homogeneous mixture of fuel and air, diesel engines are also acknowledged as 'dirty', since they produce extensive soot. Years of development has made the diesel engine controllable and effective, resulting in better fuel consumption and a cleaner engine. Nevertheless, due to the potential impact on the automotive industry, developing a clean diesel engine has been in the forefront of research for the past decade.

A new emission standard has recently been proposed by the State of California to reduce the combined emissions of non-methane organic gas (NMOG) and nitric oxide (NO_x) by 20% and particulate matter (PM) by 52% from the current standard (LEV II), active from 2014 through 2022 [1]. The California emission standard is one of the strictest in the world and has been widely accepted in many other states in the USA. Automotive manufacturers will have to meet this regulation for all new vehicles sold in the coming era. To achieve this requirement, the industry must investigate a range of factors that can potentially reduce engine emissions, including fuels, combustion process, chemical-kinetics, in-cylinder flow, fuel-air mixture formation, sprays, engine geometries, etc.

One of the solutions advanced in diesel engine applications is better fuel droplet atomization and air-fuel mixture. The evolution of high-pressure-injection technology will result in fine atomization and will provide for better air-fuel mixture [2]. Recently, the pressure of the injection systems has reached 300 MPa or more, and a number of researchers are showing interest in the performance of the ultra-high pressure injectors. To study the effect of the ultra-high injection pressure spray, characteristics such as spray penetration, Sauter mean diameter (SMD) and fuel distribution should be carefully investigated.

Nowadays, computational simulations have been adopted as a key analysis tool in engine research to establish correlation with experimental studies and provide new information for designers. A significant advantage of using Computational Fluid Dynamics (CFD) is the flexibility of simulation setups and the time and cost efficiencies

compared to experiments. The present research is being carried out to investigate the physical phenomena associated with diesel engine combustion. Major CFD commercial codes that are available in the market currently include ANSYS CFX, ANSYS FLUENT, AVL FIRE and CD-adapco STAR-CD and STAR-CCM+, whereas KIVA and OpenFOAM are becoming popular as open source codes. FLUENT has been chosen in this study to take advantage of its ability to simulate general flow problems. It offers different kinds of models to evaluate engine characteristics.

At the first stages of this study, different submodels of the engine, especially turbulence and spray models, were configured and the flow field was simulated in an effort to gain a deeper understanding of these complex flows. In the next stage, the spray model was integrated into the in-cylinder flow to observe the outcome of the interaction between the spray and the flow.

The motivations of this thesis are: 1) to understand the functionality and utility of the CFD code FLUENT in engine and spray simulations and 2) to study the effect of the ultra-high injection pressure sprays injected into a vertical-valve diesel engine.

The thesis consists of five chapters. In Chapter 2, the literature about in-cylinder flow and high injection pressure sprays and their interaction are reviewed. Further insights into the methodologies of turbulence submodels are discussed. The numerical setups of the simulations are then explained in the third chapter and the results are analyzed in the following chapter. Finally, the conclusions are drawn in the fifth chapter. The in-cylinder flow development time series for each turbulence model is presented in Appendix A and the parameters that are utilized in the simulations are listed in Appendix B at the end of this thesis.

Chapter 2. Literature Review

2.1. Introduction

The mechanisms of turbulent flow, fuel atomization, and the interaction between fuel and air in a diesel engine are yet to be fully understood. A number of researchers are presently studying the characteristics of flow and fuel properties by using currently available techniques and technologies. In this chapter, the characteristics of in-cylinder flow and entrainment of air, the use of high injection pressure spray, and its application in actual engine apparatus will be highlighted and summarized. The reviews are followed by the discussion of numerical submodels which are implemented in CFD codes.

2.2. Previous Studies

Kato et al. [3] and Yokota et al. [4] have reported on experiments in the ultra-high injection system at the primal stage of its technology. They examined the effects of the injection pressure ranging from 55 to 250 MPa and also the variations of nozzle orifice and injection duration. From their studies they concluded that the Sauter mean diameter is correlated with the average injection pressure and also the change of the injection pressure in time. Moreover, a shorter combustion process and reduced soot formation are realized by utilizing the ultra-high injection pressure and smaller orifice diameter.

Nishida's research group at the University of Hiroshima has conducted numerous experiments utilizing various ultra-high injection pressures, micro-hole nozzles, spray wall-impingement setup, and diesel and alternative diesel fuels [5-11]. The combination of 300 MPa injection pressure and 0.08 mm nozzle-hole diameter reportedly gave the best performance in terms of turbulent mixture rate and droplet size reduction to decrease the mixture process and lean mixture formation, which also agrees with the findings of Kato et al. [3] and Yokota et al. [4].

Lee et al. [12] experimentally and numerically investigated free sprays at ultra-high injection pressure in the range of 150 to 355 MPa. No significant change in the Sauter mean diameter on attaining an injection pressure of 300 MPa, and a reduced growth rate of the penetration length were reported.

Tao and Bergstrand [13] studied the effect of ultra-high injection pressures on engine ignition and combustion using three-dimensional numerical simulations. The advantage of high pressure injection in producing reduced ignition delay, short combustion phase and fast flame propagation was reported. Additionally, three different rates of injection profiles were examined. Rate falling injection, for which the injection rate is decreasing during the injection process, was found to shorten fuel burn duration at the early stage of combustion and expand at the later stage, and rate rising injection performed inversely. On the other hand, rate rising injection estimated a wider flame area at high temperature and reduced the NO formation due to faster cooling after combustion. Flame lift-off lengths were observed to be constant at different injection pressures in contrast to the case of injection in a constant volume chamber.

To study the characteristics of ultra-high injection pressure sprays numerically, it is also important to understand the role of different types of spray models. Comprehensive reviews of droplet phenomena have been presented by Lin and Reitz [14] and Jiang et al. [15]. The differences between popular breakup models have been discussed by Djavareshkian and Ghasemi [16] and Hossainpour and Binesh [17]. They reported on the implementation of WAVE (or Kelvin-Helmholtz) and KH-RT (Kelvin-Helmholtz Rayleigh-Taylor) models, and found better agreement with experimental data using KH-RT. The interaction of the mesh, turbulence model and spray has been studied by Karrholm and Nordin [18] in a constant volume chamber.

The effect of spray-in-cylinder-flow interaction is realized in the combustion process [19] and has been studied by a number of researchers. Choi et al. [20] found that the flow pattern around the spray is similar at different injection pressures. However, strong flow recirculation was observed at higher injection pressure. Spray characteristics in cross-flow was studied by Desantes et al. [21], McCracken and Abraham [22], and Park et al. [23] to observe the effect on particle size and mixing process. Correlation of penetration and dispersion of a gas jet and sprays was examined by Iyer and Abraham [24]. The effects of gas density and vaporization on penetration, injection condition and dispersion of spray have been discussed by Naber and Siebers [25], Kennaird et al. [26], and Post et al. [27]. Jagus et al. [28] assessed injection and mixing using LES turbulence modeling.

2.3. Governing Equations

The mathematical model of fluid flow and heat transfer in general is developed from the conservation laws of physics: conservation of mass, Newton's second law, and first law of thermodynamics [29]. These laws are expressed as:

Conservation of mass (Continuity equation)

$$\frac{\partial \rho}{\partial t} + \nabla \cdot (\rho \vec{u}) = 0 \tag{1}$$

Momentum equation

$$\frac{\partial}{\partial t}(\rho \vec{u}) + \nabla \cdot (\rho \vec{u}\vec{u}) = -\nabla p + \nabla \cdot \bar{\bar{\tau}} \tag{2}$$

Conservation of energy

$$\frac{\partial}{\partial t}(\rho E) + \nabla \cdot (\rho E \vec{u}) = -\nabla \cdot (p\vec{u}) + \nabla(k \text{ grad } T) + \nabla(\vec{u} \cdot \bar{\bar{\tau}}) \tag{3}$$

2.3.1. Reynolds Averaged Navier-Stokes (RANS) Equations

The random nature of turbulent flow contains a large number of phenomena. To reduce the cost of calculation, the solution of instantaneous (exact) Navier-Stokes equations are decomposed into time-averaged (mean) and fluctuating components [30]. For velocity,

$$\vec{u} = \bar{\vec{u}} + \vec{u}' \tag{4}$$

and for pressure, energy, species and other quantities,

$$\phi = \bar{\phi} + \phi' \tag{5}$$

Substituting the above into the continuity and momentum equations and taking time-averaged results to obtain the time-averaged equations yields

$$\frac{\partial \bar{\rho}}{\partial t} + \nabla \cdot \left(\bar{\rho}\vec{\bar{u}}\right) = 0 \tag{6}$$

$$\begin{aligned} \frac{\partial}{\partial t}\left(\bar{\rho}\vec{\bar{u}}\right) + \nabla \cdot \bar{\rho}\bar{u}\vec{\bar{u}} \\ = -\nabla \bar{p} + \mu\nabla\left(\text{grad } \vec{\bar{u}}\right) \\ + \left[-\frac{\partial}{\partial x}\left(\overline{\bar{\rho}\vec{u}'u'}\right) - \frac{\partial}{\partial y}\left(\overline{\bar{\rho}\vec{u}'v'}\right) - \frac{\partial}{\partial z}\left(\overline{\bar{\rho}\vec{u}'w'}\right)\right] \end{aligned} \tag{7}$$

To capture the characteristics of turbulence in the flow, a number of turbulence models have been formulated and are commonly used. Three common approaches to

simulate turbulent flows include Reynolds Averaged Navier-Stokes (RANS) equations, Large-Eddy Simulations (LES) and Direct Numerical Simulation (DES) [30]. Though LES has become popular, RANS is still favoured in the industry due to its economy, robustness and reasonable accuracy in a wide range of turbulent flows. Further, three different turbulence models are commonly used in RANS modeling and are briefly described below.

2.3.1.1. Standard k-ε model

The standard k-ε is a classical model which is based on transport equations for the turbulence kinetic energy (k) and its dissipation rate (ε):

$$\frac{\partial}{\partial t}(\rho k) + \nabla \cdot \rho k \vec{u} = \nabla \left[\left(\mu + \frac{\mu_t}{\sigma_k} \right) \text{grad } k \right] + G_k - \rho \varepsilon \tag{8}$$

$$\frac{\partial}{\partial t}(\rho \varepsilon) + \nabla \cdot \rho \varepsilon \vec{u} = \nabla \left[\left(\mu + \frac{\mu_t}{\sigma_\varepsilon} \right) \text{grad } \varepsilon \right] + C_{1\varepsilon} \frac{\varepsilon}{k} G_k - C_{2\varepsilon} \rho \frac{\varepsilon^2}{k} \tag{9}$$

where the turbulent (or eddy) viscosity, μ_t, and the production of turbulence kinetic energy, G_k, are given as

$$\mu_t = \rho C_\mu \frac{k^2}{\epsilon} \tag{10}$$

$$G_k = -\rho \overline{u_i' u_j'} \frac{\partial u_j}{\partial x_i}. \tag{11}$$

By default, the model constants $C_{1\varepsilon}$, $C_{2\varepsilon}$, C_μ, and the turbulent Prandtl numbers σ_k and σ_ε are determined as follow to accommodate a variety of flow problems.

$C_{1\varepsilon} = 1.44$, $C_{2\varepsilon} = 1.92$, $C_\mu = 0.09$, $\sigma_k = 1.0$ and $\sigma_\varepsilon = 1.3$.

2.3.1.2. Renormalization Group (RNG) k-ε model

RNG k-ε is a more refined model than the standard k-ε model, developed using a statistical technique. The differences between the two models are:

- An additional term is introduced in the dissipation equation to improve the accuracy in rapidly strained flows.
- The accuracy of the swirl flow is improved.
- An analytical formula for turbulent Prandtl numbers (inverse effective Prandtl numbers, α_k and α_ε) is added where the standard k-ε uses adjustable constants.

- Effective viscosity, μ_{eff}, is also analytically derived to handle the low-Reynolds number case.

The equations for the RNG k-ε model are:

$$\frac{\partial}{\partial t}(\rho k) + \nabla \cdot \rho k\vec{u} = \nabla\left[\alpha_k \mu_{eff} \text{ grad } k\right] + G_k - \rho\varepsilon \tag{12}$$

$$\frac{\partial}{\partial t}(\rho\varepsilon) + \nabla \cdot \rho\varepsilon\vec{u} = \nabla\left[\alpha_\varepsilon \mu_{eff} \text{ grad } \varepsilon\right] + C_{1\varepsilon}\frac{\varepsilon}{k}G_k - C_{2\varepsilon}\rho\frac{\varepsilon^2}{k} - R_\varepsilon \tag{13}$$

where

$$\mu_{eff} = \mu + \mu_t \tag{14}$$

$$R_\varepsilon = \frac{C_\mu \rho \eta^3 (1 - \eta/\eta_0)}{1 + \beta\eta^3}\frac{\varepsilon^2}{k}. \tag{15}$$

$$\eta = S\frac{k}{\varepsilon} \tag{16}$$

The dissipation equation can be rewritten as

$$\frac{\partial}{\partial t}(\rho\varepsilon) + \nabla \cdot \rho\varepsilon\vec{u} = \nabla\left[\alpha_\varepsilon \mu_{eff} \text{ grad } \varepsilon\right] + C_{1\varepsilon}\frac{\varepsilon}{k}G_k - C_{2\varepsilon}^*\rho\frac{\varepsilon^2}{k} \tag{17}$$

where

$$C_{2\varepsilon}^* = C_{2\varepsilon} + \frac{C_\mu \rho \eta^3 (1 - \eta/\eta_0)}{1 + \beta\eta^3}. \tag{18}$$

The model constants of the RNG k-ε model, $C_{1\varepsilon}$, $C_{2\varepsilon}$, C_μ, α_k, α_ε, η_0 and β, are given as below.

$C_{1\varepsilon} = 1.42$, $C_{2\varepsilon} = 1.68$, $C_\mu = 0.0845$, $\alpha_k = \alpha_\varepsilon = 1.393$, $\eta_0 = 4.38$ and $\beta = 0.012$.

2.3.1.3. Standard k-ω model

The standard k-ω model (or Wilcox k-ω model) is another two-equation RANS turbulence model which replaces the rate of dissipation of turbulent kinetic energy in the k-ε model by the turbulence frequency (or specific dissipation rate), $\omega = \varepsilon/k$. The equations have forms similar to the k-ε model:

$$\frac{\partial}{\partial t}(\rho k) + \nabla \cdot \rho k\vec{u} = \nabla\left[\left(\mu + \frac{\mu_t}{\sigma_k}\right) \text{ grad } k\right] + P_k - \beta^*\rho k\omega \tag{19}$$

$$\frac{\partial}{\partial t}(\rho\omega) + \nabla \cdot \rho\omega\vec{u} = \nabla\left[\left(\mu + \frac{\mu_t}{\sigma_\omega}\right) \text{grad } \omega\right] + \gamma_1\left(2\rho S_{ij} \cdot S_{ij} - \frac{2}{3}\rho\omega\frac{\partial\vec{u}}{\partial y}\delta_{ij}\right) - \beta_1\rho\omega^2 \quad (20)$$

where the eddy viscosity is given by

$$\mu_t = \frac{\rho k}{\omega} \quad (21)$$

and the rate of production of turbulent kinetic energy is

$$P_k = \left(2\mu_t S_{ij} \cdot S_{ij} - \frac{2}{3}\rho k\frac{\partial\vec{u}}{\partial y}\delta_{ij}\right) \quad (22)$$

The standard k-ω model has the model constants, the turbulent Prandtl numbers σ_k and σ_ω, and non-dimensional constants γ_1, β^* and β_1, which are given as below.

$$\alpha_k = \alpha_\varepsilon = 2.0,\ \gamma_1 = 5.53,\ \beta^* = 0.09 \text{ and } \beta_1 = 0.075$$

2.3.2. Detached Eddy Simulation (DES) Model

Detached Eddy Simulation (DES) is also explored in this research to benchmark the flow inside a cylinder. The DES model is a three-dimensional unsteady numerical algorithm which incorporates RANS and Large-Eddy Simulation (LES) into the flow calculation [31]. It is generally referred to as a hybrid RANS/LES method as the LES mode (subgrid-scale or SGS function) is utilized in the separated region whereas the RANS mode prevails in the boundary-layer region. In this study, the DES model based on the one-equation Spalart-Allmaras RANS model has been used. In RANS mode, DES replaces the length scale of the model, the distance to the closest wall, d, by the following equation:

$$\tilde{d} \equiv min(d,\ C_{DES}\Delta) \quad (23)$$

where Δ is the largest grid spacing in a cell and the empirical constant C_{DES} is taken as 0.65. The method determines the modes by comparing the grid spacing and the wall distance to the thickness of the turbulent layer, δ. In case the layer is thin compared to the grid spacing ($\delta \ll \Delta$) and the wall distance ($\delta \ll d$), DES is in RANS mode. If the grid is fine ($\delta \geq \Delta$), then DES is operated in LES mode [32].

2.4. Meshing

In the case of engine applications, due to its complex geometry, the flow domain is meshed by several different approaches. An engine model to be simulated in ANSYS FLUENT 13.0 [33] is meshed with a hybrid topology. A multi-block methodology is exploited to split the calculation domain into four major zones; chamber, piston layer, ports and valve layer, as seen in Fig. 2.1. The zones adjacent to reciprocating boundaries such as the piston and valves are meshed with quadrilateral cells (structured mesh) and layered. Tetrahedral cells (unstructured mesh) are used in the chamber zone because the valves move into this zone and its cells deform and must be remeshed. Interfaces must be created between the chamber and valve layer zones to transfer nodal values from one side to the other. Understanding the concepts of meshing facilitates users to mesh the geometry efficiently.

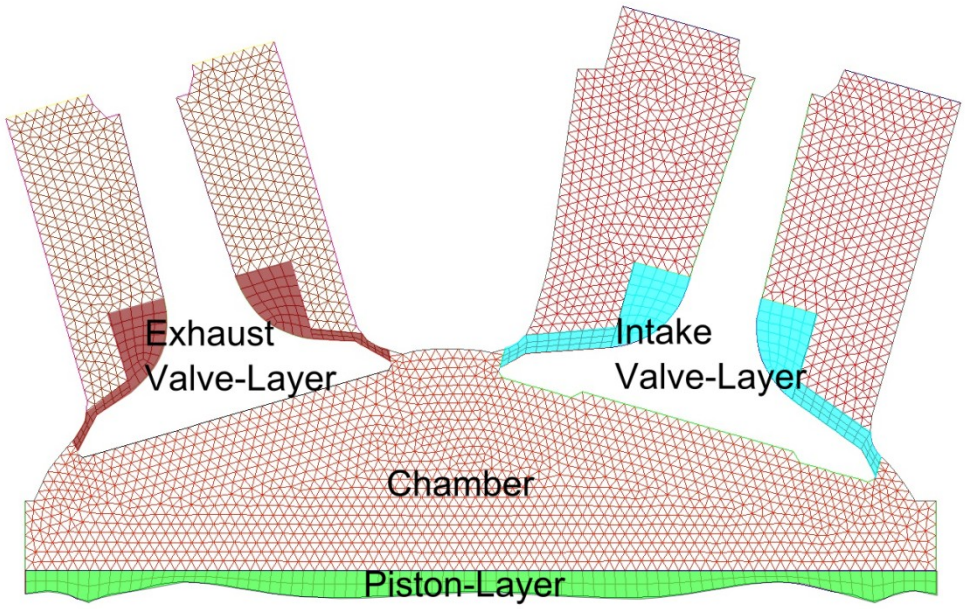

Figure 2.1 – Example of face sections in two-dimensional spark ignition engine acquired from FLUENT tutorial

2.4.1. Dynamic Mesh

Dynamic meshing is one of the methods which adapt the deformation of cells affected by the motion of moving boundaries. Several dynamic mesh methods are available in FLUENT: smoothing, layering and remeshing. For engine models, layering dynamic mesh is applied for piston and valve layer zones which experiences one-

directional reciprocation and smoothing and remeshing are implemented for the chamber zone where the domain undergoes intricate deformations.

2.4.2. Smoothing Method

Smoothing method is a mesh deformation procedure that uses connecting edges as a spring. By the motion of a moving boundary, meshes are squeezed or stretched by the spring factor (see Fig. 2.2). The number of cells does not change during the process. Note that this method may cause high skewness and may lead to error in calculation. Also, this method can only be applied to an unstructured mesh.

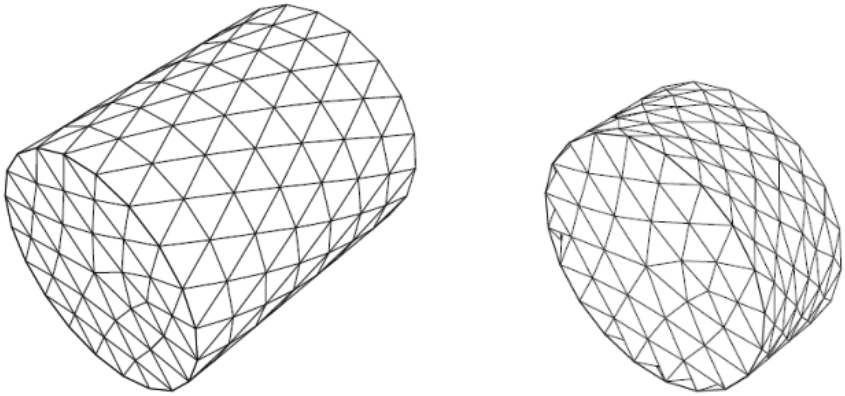

Figure 2.2 – Smoothing method [33]

2.4.3. Layering Method

Layering method splits and merges layers when a moving boundary reaches the neighbouring nodes by a factor of height or by a ratio specified in the dynamic mesh zone. Figure 2.3 shows an example of the method. For instance, let height be h and the collapse factor be specified as 0.5. When a moving boundary crosses the line of 0.5·h from the neighbouring layer, Layer 1 will be merged into the moving boundary. The equations for handling the split and collapse cases are given as:

$$\text{Split:} \qquad h > (1 + \alpha_s) \cdot h_{min}$$

$$\text{Collapse:} \qquad h < \alpha_c \cdot h_{min}$$

where α_s is split factor, α_c is collapse factor and h_{min} is the ideal size of cell height. Note that the layering method only works with a structured mesh.

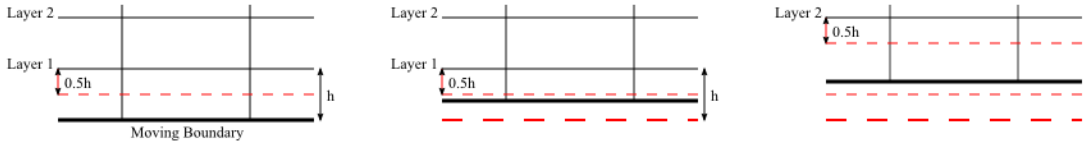

Figure 2.3 – Layering method [33]

2.4.4. Remeshing Method

The remeshing method works on top of the smoothing method. Quality of the cell skewness or length scale is used to determine whether to generate or unite the mesh next to a moving boundary (Fig. 2.4). The issue of skewness in the smoothing method can be avoided by using this method.

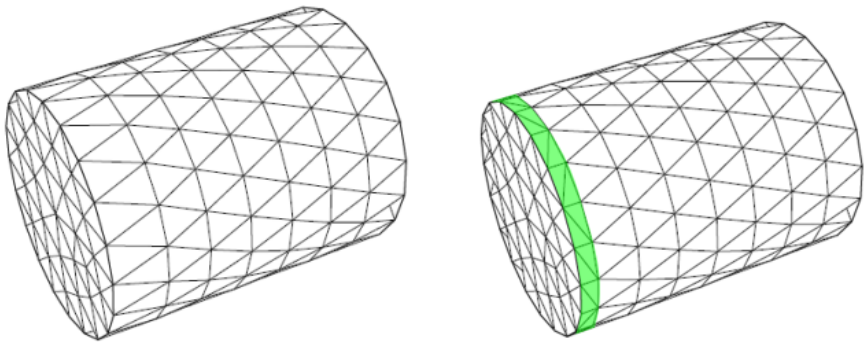

Figure 2.4 – Remeshing method [33]

2.4.5. Interface

Each zone shares the nodes on the common edges or faces; however, the interfaces of the valve-layer and chamber zones experience different grid reallocation utilized by different dynamic meshing methods on each zone. Valve-layer zone cells are either created or merged with neighbouring cells in the chamber zone being deformed while the valves travel. Interaction between two different faces in the dynamic mesh and remeshing zones is processed as shown in Fig. 2.5 in every time-step [3]. For example, at one of the time steps, variables at node “E” of cell zone 2 are interpolated from node “b” and “c” which is transported from node “B” and “C” in cell zone 1, respectively. The interfaces are physically separated by some small distance within a tolerance; therefore, no common node or edge generally exists between the interfaces. Boolean operation may be used to split the volumes to obtain detached interfaces.

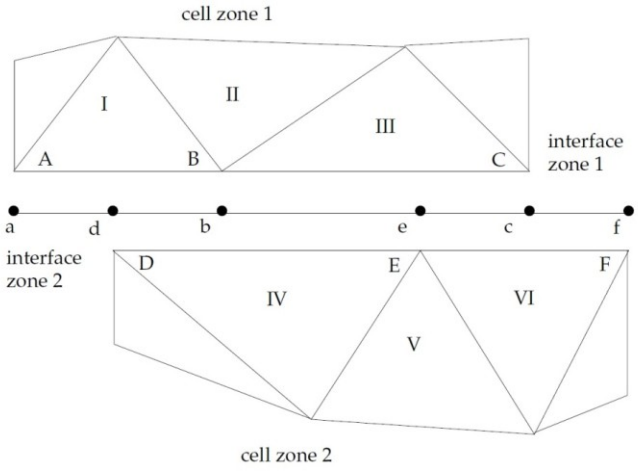

Figure 2.5 – Interface method [33]

2.4.6. Meshing Summary

In this research, GAMBIT, a pre-processor of FLUENT, is used to generate geometries and meshes. In the next section, several points are highlighted as to how to appropriately model boundaries and dynamic zones.

First of all, a multi-dimensional engine model is created in a CAD software, e.g., CATIA, Pro/ENGINEER, etc., saved in IGES format (.igs) and imported into GAMBIT. The FLUENT In-Cylinder model requires a piston and valves at Top-Dead Center (TDC) position if a simulation is an open loop cycle. Valves should not be fully closed and a small gap (at least one layer of cells) should be set between a valve and valve seat because of topology. For a closed loop cycle case, the engine geometry (or simply piston crown) should be set to crank-angle (CA) at the starting point. For the closed loop cycle case, the valves are disregarded and a chamber head is generally represented by a pancake shape for diesel engine models. After importing the geometry created in the CAD software, the engine model is split into several volume sections as discussed at the beginning of this section and meshed accordingly.

2.5. Spray and Breakup Models

In CFD, spray mechanisms are represented by mathematical models. Two approaches, Euler-Lagrange and Euler-Euler, are used in multiphase flows. In both of these approaches, the fluid phase is regarded as a continuum and modeled by the Navier-Stokes equations. For the Euler-Lagrangian approach, the Lagrangian discrete phase model is introduced in general CFD codes to calculate the disperse phase by tracking

particles, droplets or parcels [34]. The trajectories of particles in a turbulent flow field are predicted by the turbulent dispersion models. To reduce the computational time of the particle collision calculation, the O'Rourke algorithm is employed [35]. The outcomes of collisions are also determined by this algorithm, i.e., whether the droplets coalesce or reflect apart [27].

The mathematical model of the droplet evaporation is mostly concerned about the phase of fuel vapour diffusion from the surface of the droplet into the ambient gas. Two models are often utilized by researchers. The hydrodynamic model focuses on the diffusion of droplet to control its vaporization and the kinetic model is concerned with the molecules' detachment from the surface of a droplet [36]. The disintegration of existing droplets is modeled to numerically simulate different kinds of breakup modes. The Taylor Analogy Breakup (TAB) model, a classical breakup model proposed by O'Rourke and Amsden [37] using the analogy of an oscillating spring-mass system, is used in low Weber number cases and is appropriate in low speed sprays.

WAVE or Kelvin-Helmholtz (KH) instability model [38] and Kelvin-Helmholtz Rayleigh-Taylor (KH-RT) instability model [39], known as a hybrid model, are favoured in high speed high Weber number (We >100) fuel-injection models. KH-RT incorporates the effects of aerodynamic breakup and instabilities of droplet acceleration; thus, it is capable of handing both TAB and WAVE models. Recently, there have been many hybrid models developed by combining different breakup models to estimate the spray characteristics accurately over a variety of Weber number [23, 40]. In ANSYS FLUENT 13.0, TAB, WAVE and KH-RT models are available. The two latter options are the most suitable in this study due to the high Weber number condition. In the next subsections, both of these models are discussed in detail to estimate the coefficients of the models.

2.5.1. WAVE Model

Reitz [38] developed a model called WAVE based on droplet breakup due to the relative velocity between the gaseous and liquid phase. The model is formulated from the Kelvin-Helmholtz instability's wavelength and growth rate to determine the size of the droplets. The model is limited by Weber number, We, which must be larger than 100 so that Kelvin-Helmholtz instability is dominant in the droplet breakup. The maximum wave

growth rate (also the most unstable surface wave), Ω, and corresponding wavelength, Λ, are defined as,

$$\frac{\Lambda_{KH}}{r_0} = 9.02\frac{(1+0.45Z^{0.5})(1+0.4T^{0.7})}{(1+0.87We_l^{1.67})^{0.6}} \tag{24}$$

$$\Omega_{KH}\left(\frac{\rho_l r_0^3}{\sigma}\right)^{0.5} = \frac{\left(0.34+0.38We_l^{1.5}\right)}{(1+Z)(1+1.4T^{0.6})} \tag{25}$$

where $Z = \frac{We_l^{0.5}}{Re_l}$, $T = Z \cdot We_g^{0.5}$, $We_l = \frac{\rho_l U^2 r_0}{\sigma}$, $We_g = \frac{\rho_g U^2 r_0}{\sigma}$ and $Re_l = \frac{U r_0}{\nu_l}$. Here Z is the Ohnesorge number, T is the Taylor number, U is the relative velocity between droplet and gas and r_0 is the radius of the undisturbed jet. *We* and *Re* are the Weber number and the Reynolds number and subscripts *l* and *g* represent liquid and gas phase, respectively. The radius of a newly formed droplet from a parent droplet during the breakup process is assumed proportional to the wavelength Λ_{KH},

$$r = B_0\Lambda_{KH} \tag{26}$$

The constant B_0 is set equal to the experimentally determined value of 0.61. Additionally, the rate of change of the parent droplet is defined by

$$\frac{dr}{dt} = -\frac{r_0 - r}{\tau_{KH}}, \qquad r < r_0 \tag{27}$$

where the breakup time, τ_{KH}, is given by

$$\tau_{KH} = 3.726\frac{B_1 r}{\Lambda_{KH}\Omega_{KH}} \tag{28}$$

The breakup time constant B_1 is an adjustable variable which is recommended to be in the range of 1.73 to 60 [38, 41, 42]. Larger values of B_1 produce fewer breakups and more penetration. An estimation of the B_1 factor has been proposed by Liu et al. [43]:

$$B_1 = k\Omega_{KH}\Lambda_{KH}\frac{\rho_l}{(\Delta P\rho_a)^{0.5}} \tag{29}$$

where ΔP is pressure difference in the nozzle hole and ρ_a is the density of ambient air.

However, Liu et al. [43] conclude that Eq. (29) does not determine the value of this constant qualitatively and recommend that it should be used only as a first guess.

2.5.2. Kelvin-Helmholtz Rayleigh-Taylor (KH-RT) Model

The KH-RT instability model is a combination of Kelvin-Helmholtz (KH) instability and Rayleigh-Taylor (RT) instability models. Both Kelvin-Helmholtz and

Rayleigh-Taylor models decide droplet breakup by detecting the fastest growing surface wave on the droplets. The source of the Kelvin-Helmholtz wave is induced by aerodynamic forces between gas and liquid phases, whereas the Rayleigh-Taylor wave is the result of acceleration of shed drops ejected into free-stream conditions. Hwang et al. [39] showed in their experiments the occurrence of a sequential breakup process in the catastrophic breakup regime. A droplet first gets flattened by the aerodynamic force on it and breaks up due to the deceleration of the sheet droplet by means of Rayleigh-Taylor instability model. Further breakups proceeded by the smaller wavelength of Kelvin-Helmholtz wave found at the edge of the fragments. In high Weber number cases with high droplet acceleration, Rayleigh-Taylor instability grows faster and dominates the breakup of droplets. For the numerical model, both instability models are utilized simultaneously and breakups are determined by the fastest growth rate of waves. In the Rayleigh-Taylor model, the fastest growing wave's growth rate and its corresponding wavelength are given by

$$\Omega_{RT} = \sqrt{\frac{2\left[a\left(\rho_l - \rho_g\right)\right]^{3/2}}{3\sqrt{3\sigma}\left(\rho_l - \rho_g\right)}} \tag{30}$$

$$\Lambda_{RT} = 2\pi \frac{C_{RT}}{K_{RT}} \tag{31}$$

where a is the droplet acceleration, C_{RT} is the Rayleigh-Taylor breakup constant and K_{RT} is the wave number given by

$$K_{RT} = \sqrt{\frac{a\left(\rho_l - \rho_g\right)}{3\sigma}}. \tag{32}$$

Breakup time in the Rayleigh-Taylor model is defined as

$$\tau_{RT} = \frac{C_\tau}{\Omega_{RT}} \tag{33}$$

where C_τ is the breakup time constant and the liquid core length, L_{RT}, is obtained from Levich theory [44] as a function of gas and liquid densities and effective nozzle hole diameter, d_0:

$$L_{RT} = C_L d_0 \sqrt{\frac{\rho_l}{\rho_g}}. \tag{34}$$

The radius of the new droplets is calculated as half of the wavelength obtained above $\left(r = \frac{\Lambda_{RT}}{2} = \frac{\pi C_{RT}}{K_{RT}}\right)$.

Based on their experiments, Hiroyasu and Arai [45] proposed the correlation of density and diameter to the Levich constant, C_L, experimentally as,

$$C_L = 7.0\left(1 + 0.4\frac{r}{d_0}\right)\left(\frac{P_a}{\rho_l U_l^2}\right)^{0.05}\left(\frac{l_0}{d_0}\right)^{0.13}. \tag{35}$$

where P_a is ambient pressure.

Moreover, Senecal [46] analytically determined the relationship of the Levich constant, C_L, and the breakup time constant of the WAVE model, B_1. Considering the breakup length of the WAVE model to be $L_{KH} = U \cdot \tau_{KH}$ and assuming that the viscosity is zero, Eq. (28) reduces to

$$\tau_{KH} = \frac{B_1}{U}\sqrt{\frac{\rho_l}{\rho_g}}\frac{d_0}{2} \tag{36}$$

and therefore,

$$L_{KH} = B_1\sqrt{\frac{\rho_l}{\rho_g}}\frac{d_0}{2}. \tag{37}$$

Comparing Eq. (34) and (37), the correlation of the coefficients is given by

$$C_L = \frac{B_1}{2}. \tag{38}$$

As this relation shows, the Levich constant is also adjustable and ranges from 5 to 20. In addition, Patterson and Reitz [41] investigated the effects of Rayleigh-Taylor breakup constant, C_{RT}, in the range $1.0 \leq C_{RT} \leq 5.33$.

2.6. Summary

In this chapter, the literature on in-cylinder flow, the spray process and their correlation are reviewed. Not many numerical studies have been conducted with ultra-high injection pressures. The objective of this research is to take advantage of numerical simulation to investigate the effect of high pressure injection on atomization and fuel

mixture with in-cylinder flow and to optimize the numerical setup. The appropriate submodels are carefully investigated and each parameter is estimated ahead of modeling the engine simulation.

Chapter 3. Numerical Setup

3.1. Introduction

The grid independency test of the spray model is first achieved by considering a constant volume vessel with different grid sizes. To this end, the experimental results from Wang et al. [8] are used. Then, an engine model with vertical ports is meshed and the flow structure is verified. Finally, the spray models are introduced into the engine simulation, with three different injection pressures and two port inlet pressure cases. The spray configurations are presented and the model setup is discussed.

All simulations, from this point on, are conducted utilizing SIMPLEC (Semi-Implicit Method for Pressure-Linked Equations Consistent) algorithm for pressure-velocity coupling and first- and second-order upwind schemes for spatial discretization scheme. Standard and second-order scheme are used for pressure discretization scheme and first-order implicit formulation is used for time marching scheme in all the simulations. Details of the setup are also found in Appendix B.

3.2. Grid Independence

Initially, grid independency tests were conducted to optimize the grid size in the engine simulation. The simulations were performed on a 60 mm (D) × 60 mm (W) × 80 mm (H) fixed chamber with similar condition as the experiments of Wang et al. [8]. Five different sets of grids, with 70 × 70 × 105 (0.5 million), 87 × 87 × 130 (1.0 million), 93 × 93 × 140 (1.2 million), 100 × 100 × 150 (1.5 million), and 106 × 106 × 160 (1.8 million) nodes, were generated. Figure 3.1 shows the results for a 300 MPa spray injection pressure with the five different meshes. It is seen that 0.5 million cells over-estimates the penetration significantly. Moreover, the domain with 1.0 million cells slightly over-predicts the penetration in comparison with the rest of the grids. From this information, we concluded that in the case of the ultra-high injection spray model, the domain should be meshed with 93 × 93 × 140 cells or finer to avoid any effects of grid size on penetration length. For our subsequent calculations, the optimal grid size is chosen to be 93 × 93 × 140, with the largest grid size set at 0.65 mm in the chamber of the engine model.

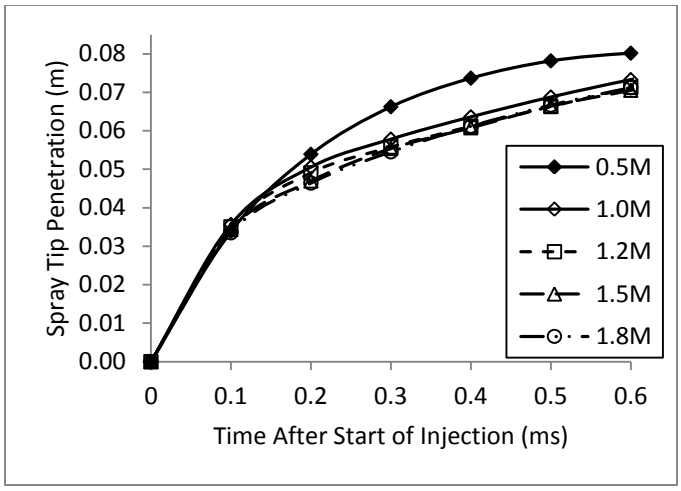

Figure 3.1 – Spray tip penetration results for the grid independency tests

3.3. Mesh Pre-processing in the Vertical Valve Engine Geometry

The geometry utilized in this study is obtained from the KIVA3V manual [47], and illustrated in Fig. 3.2. The geometry is appropriately meshed with a hybrid mesh and sized by the optimum grid size obtained from the previous section. The maximum number of cells for the engine geometry is 166,500 cells at TDC and 570,000 cells when the piston surface reaches the bottom dead centre (BDC).

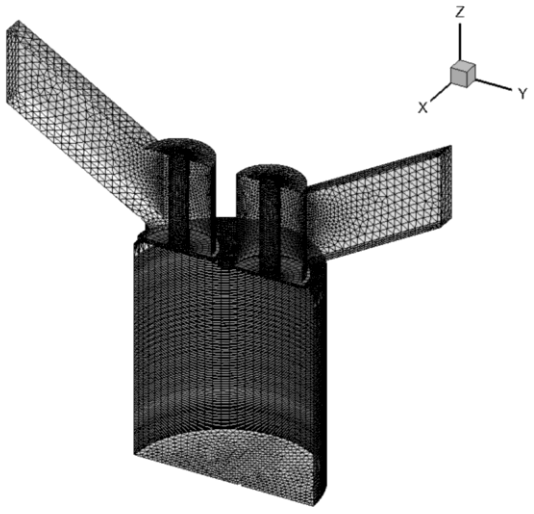

Figure 3.2 – Vertical ports engine geometry and mesh at BDC

Note that during the simulations conducted using the RNG k-ε and the standard k-ω turbulence models in the next chapter, divergence in the continuity equation was detected following the closure of the inlet valve. The divergence in the calculation results in very high in-cylinder pressure of about 1,000 bar at the beginning of the compression

process. The cause of this issue was found to be the quality of the mesh at the valve-layer zone. The original mesh has 40 nodes in the tangential direction and 7 nodes in the radial direction, as shown in Fig. 3.3. To overcome the non-convergence problem, the valve-layer zone mesh has been refined by doubling the number of nodes in the tangential direction (80 nodes) and by increasing the radial nodes to 20 (see Fig. 3.4).

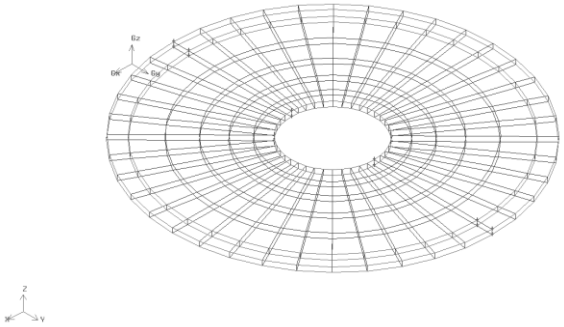

Figure 3.3 – Valve-layer zone with coarse mesh

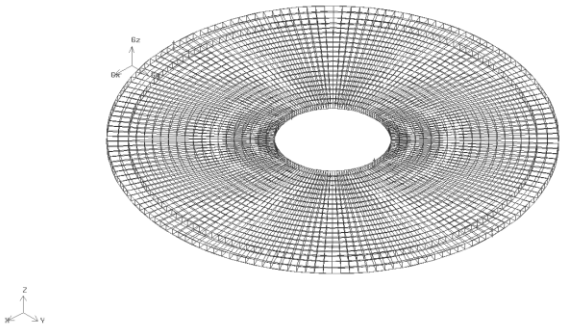

Figure 3.4 – Valve-layer zone with fine mesh

Due to the refinement of the valve-layer zone, the neighbouring zones, the chamber and ports, are also refined at the same time. Eventually, the total cell size at BDC becomes 0.77 million cells with the refined mesh. After the modification, all the RANS models successfully completed the engine simulation.

In addition to the refined original mesh, another refinement at the piston layer zone was carried out for using the Detached Eddy Simulation (DES), which requires a finer mesh size. The number of grid points was changed from 80 nodes to 160 nodes on outer edge of the piston-layer and from 20 nodes to 60 nodes in the radial direction, as shown in Fig. 3.5. This refinement eventually makes the size of grids smaller in the

chamber zone which is adjacent to the piston-layer zone. By this mesh manipulation, the total number of cells at the BDC becomes 2.46 million cells which is about four times larger than the coarse mesh, which has 0.57 million cells.

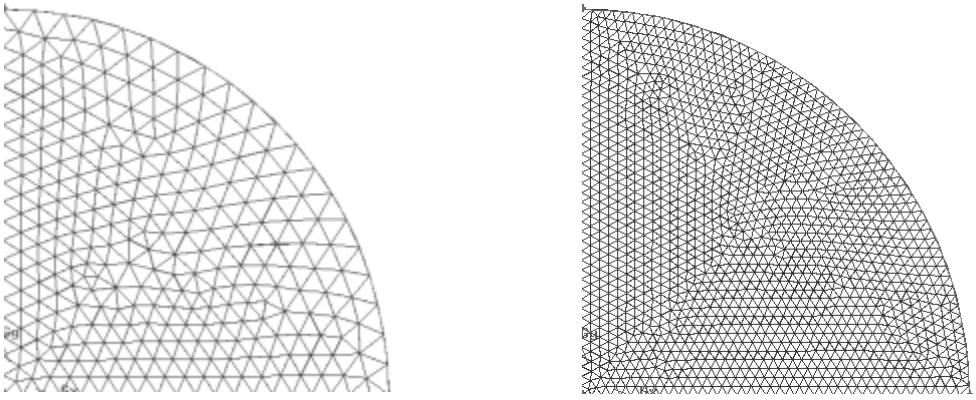

Figure 3.5 – Mesh refinement in piston-layer zone

From this point forward, the original mesh with coarse valve-layer mesh is referred to as the "coarse" mesh, whereas the mesh with fixed valve-layer mesh and with refined piston-layer mesh is regarded as "refined" and "fine" mesh, respectively.

3.4. Computational Domain Setup

The engine geometry is 82.55 mm in bore and 92.075 mm in stroke. Further, a high compression ratio of 17.2:1 is used. The connecting rod length is 174 mm and the engine is operated at 1500 rpm. Other engine operating conditions are listed in Table 3.1. The engine model is set at top dead center (TDC) position initially by the requirement of FLUENT [33].

All wall boundaries including the moving boundaries such as piston and valves are kept at constant temperature of 360 K during the simulation. One of ports in the positive Y-direction is assigned as inlet port and the other side as exhaust port (see Fig 3.2). A pressure inlet is used at the inlet boundary. Two different inlet pressures, 1.0 and 1.5 atm, are applied at the inlet boundary representing a naturally aspirated (NA) case and a turbocharging-like case. Temperature of the inlet is maintained at 318 K. The flow direction at the inlet is set parallel to the intake runner walls. The outlet boundary (in the negative Y-direction) is set as a pressure outlet where the gauge pressure is zero. The internal interfaces between chamber and valve zones, as discussed before, do not contribute physically in the calculation; however, when the valves are fully closed, the

interfaces are treated as walls and the boundary conditions are determined from the adjacent wall boundaries.

The diesel fuel which is utilized in this simulation is n-decane ($C_{10}H_{22}$) with properties taken according to the experimental data listed in Table 3.2 [8]. Four injection points are set at the centre of the cylinder head, offset by 0.5 mm from the cylinder axis. The nozzle holes are 90 degrees apart and face towards positive X, positive Y, negative X, and negative Y directions. For convenience, the injectors are referred to as INJ-0, INJ-90, INJ-180 and INJ-270, respectively. Nozzle geometry and injection conditions are summarized in Table 3.3.

Table 3-1 – Engine operation conditions and initial setups

Engine speed	1500 rpm
Stroke	92.075 mm
Bore	82.55 mm
Connecting rod	174 mm
Compression ratio	17.2:1
Number of valves	2
Intake valve open (IVO)	-15° ATDC
Intake valve close (IVC)	200° ATDC

Table 3-2 – Diesel fuel properties

Fuel type	n-decane ($C_{10}H_{22}$)
Density	830 kg/m^3
Kinematic viscosity	3.36 mm^2/s
Surface tension	0.0255 N/m
Heating value	43.1 MJ/kg

Table 3-3 – Nozzle configurations and spray injection parameters

Number of holes	4
Hole diameter	0.16 mm
L/D ratio of nozzle hole	7.5
Angle of fuel-jet axis	152°
Injection pressure	100, 200, 300 MPa
Start of injection	-25.5° ATDC
Injection duration	2.2, 1.4, 1.3 ms

Chapter 4. Results and Discussion

In this chapter, the results of in-cylinder flows and spray development in the chamber are presented. First, the flow characteristics inside the chamber are investigated and discussed in comparison with the work conducted by other researchers. Various turbulence models are examined to study their performance. Secondly, spray models are built into the engine simulations and a diesel fuel is injected into the cylinder at ultra-high pressures. The spray characteristics and mixture processes of fuel and air under different flow conditions inside the cylinder are analyzed.

4.1. In-cylinder Flow Validation, Investigation and Analysis using RANS and DES Turbulence Models

4.1.1. Mean In-cylinder Pressure Validation

Initially, the in-cylinder flow validation and the role of the various turbulence models are analyzed. The purpose of examining the turbulence model is to observe the performance of each RANS model in predicting engine parameters. For this purpose, the RNG k-ε and the standard k-ω turbulence models have been chosen. The RNG k-ε model is popular in simulations where the engine model and spray injection model interact [48, 49], whereas the standard k-ω model is very rarely used. Additionally, DES is conducted in the same environment to set a benchmark for the RANS models.

Due to the simplified geometry of the engine used in this study, limited experimental data is available for validation. Therefore, the mean in-cylinder pressure of the model in this study is compared with another numerical simulation which use the same geometry (Jonnalagedda et al., [50]). In that study, an HCCI model with the same simplified vertical valves engine geometry was used with RANS and LES models in KIVA3V. Figure 4.1 shows the difference in the volume-averaged in-cylinder pressure between the turbulence models [30]; standard k-ε model with coarse mesh in this study and RANS and LES models of Jonnalagedda et al. [50]. In addition, Figure 4.2 shows the mean in-cylinder pressure curves for different combinations of turbulence models and mesh sizes used in the current study. In Table 4.1, the pressure difference between the previous simulations [50] and the various turbulence models with refined meshes are

summarized. The maximum pressure difference (at the peak) between the coarse mesh standard k-ε and LES model is 8.34 % while the difference between the RANS and LES models is -5.73 %. The maximum difference of the peak pressure of the standard k-ε model with the fine mesh compared with the coarse mesh standard k-ε model is -2.08 %. The pressure difference between the standard k-ε with fine mesh and LES model becomes 6.09 %, which indicates a 2.25 % improvement. The results show that all the turbulence models with refined meshes estimate a lower peak pressure than the coarse mesh result. However, even the result of the standard k-ε model with the coarse mesh is favourably close to the simulations of Jonnalagedda [50], so one can conclude that there is no significant dependence of turbulence model and mesh size on the prediction of the chamber pressure.

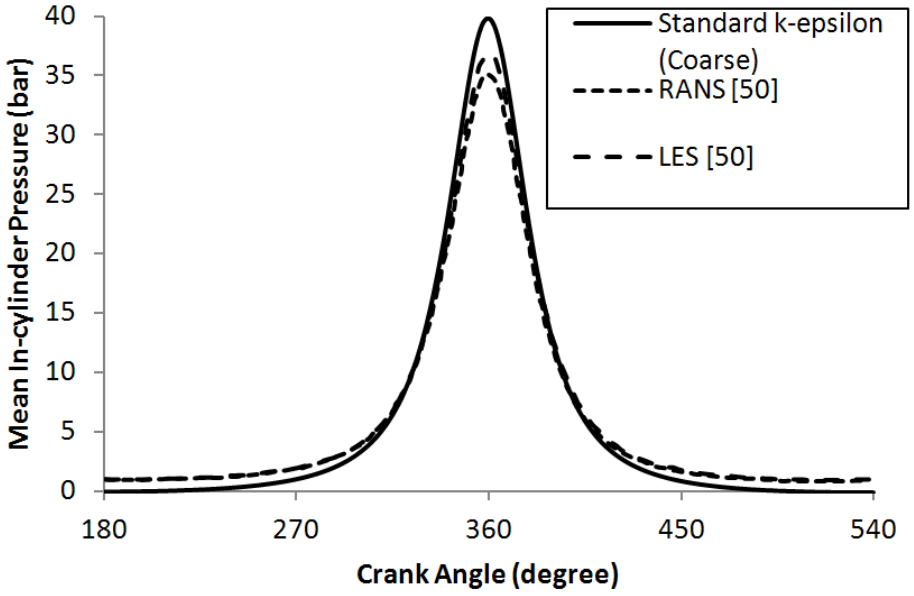

Figure 4.1 – Mean in-cylinder pressure variation for the coarse standard k-ε model in present work, and RANS and LES models [50]

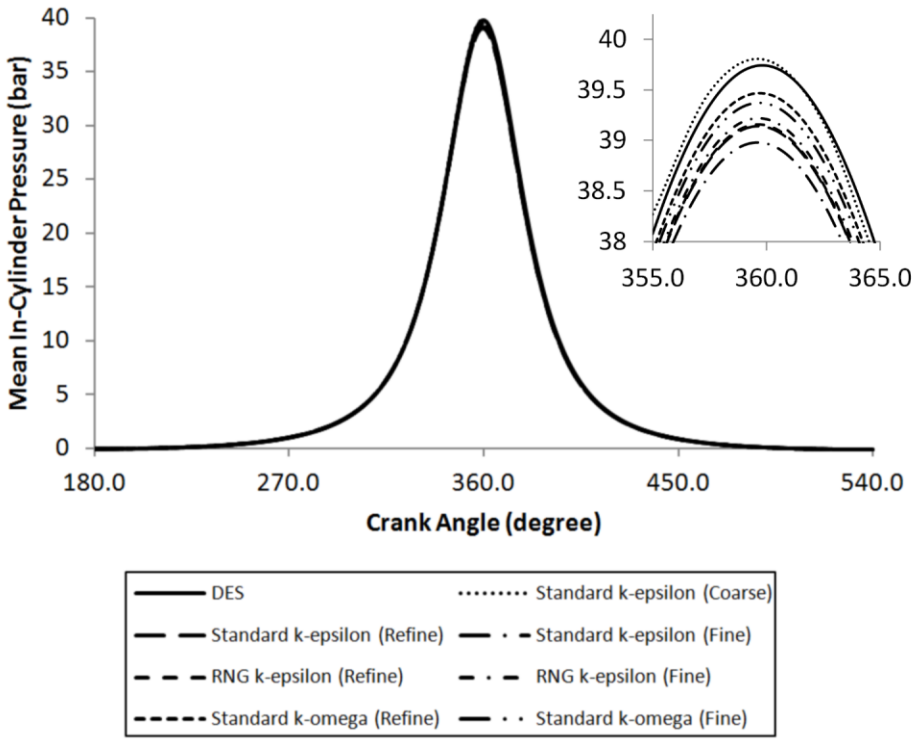

Figure 4.2 – Mean in-cylinder pressure variation of naturally aspirated case with different turbulence models and mesh sizes

Table 4-1 – Differences of mean in-cylinder pressure at TDC for each turbulence model

	Standard k-ε (Coarse)	LES [50]
Standard k-ε (Coarse)		8.34 %
Standard k-ε (Refine)	-1.67 %	6.53 % (-1.81)
Standard k-ε (Fine)	-2.08 %	6.09 % (-2.25)
RNG k-ε (Refine)	-1.63 %	6.58 % (-1.76)
RNG k-ε (Fine)	-1.48 %	6.74 % (-1.60)
Standard k-ω (Refine)	-0.84 %	7.43 % (-0.91)
Standard k-ω (Fine)	-1.09 %	7.16 % (-1.18)

4.1.2. Discussion of General Flow Development in Engine Cylinder

For a better understanding of the general flow development inside the cylinder, the experimental work of Jeng et al. [51] is considered. They conducted experiments using a two-valve engine with bowl-in-piston and pancake piston to capture the tumble motion. The engine was operated at 400 and 1100 rpm of engine speed and the intake valve was either shrouded or non-shrouded. In-cylinder flow was visualized using a Particle Image Analyzer (PIA). In their study, the pancake piston engine with non-

shrouded intake valve at operating engine speed of 1100 rpm is of particular interest here because of similar engine operation conditions. A schematic of the in-cylinder flow is shown in Fig. 4.3.

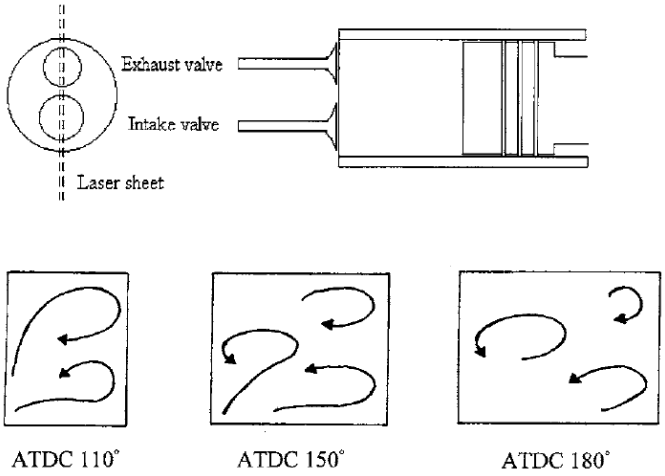

Figure 4.3 – Schematic of in-cylinder flow field at different crank angle [51]

At the early stage of the intake process (ATDC 110° in Fig. 4.3), fresh air is dragged into the cylinder through the gap of the inlet valve in a jet flow manner. Two major flows are immediately deflected by the cylinder walls before engaging to the piston. The deflected flows subsequently generate two larger-scale opposing vortices which grow along the downward motion of the piston. These two opposing vortices are relatively of the same strength. Therefore, the tumble flow motion does not develop in the chamber. The counter-clockwise vortex exiting from the intake valve near Bottom Dead Centre (BDC) period (ATDC 150° in Fig. 4.3) is forced to remain in the upper region of the cylinder due to the presence of the two vortices discussed above. The similar process of in-cylinder flow development has been captured in each turbulence model and is presented in Appendix A. Further discussions of the flow features are made in the next section.

4.1.3. In-cylinder Flow Validation

The flow structure predicted by each model can be examined. For the flow structure validation, the experimental work of Krishna and Mallikarjuna [52, 53] is used, although the experiment was conducted at different conditions than in the present simulations. The engine was operated at a lower speed (1000 RPM) and different valve

timings (IVC at 210 CA ATDC). The cylinder head wall between intake and exhaust valve was smooth. The field-of-view of their experiments is only one-third of the engine stroke (35 mm/105 mm). Even though the experiment was operated at different conditions, the similarity in engine geometries by having two vertical valves and a flat pancake piston is still beneficial to validate the in-cylinder flow. Figure 4.4 captures the stream traces on the cut plane through the middle of the ports (YZ plane) at 180 CA (BDC). The size of the field-of-view of the present study is matched to that of Krishna and Mallikarjuna [52, 53]. In the experimental flow field (central image in Fig. 4.4), three main flow structures can be identified; a large eddy in the middle (denoted as "A"), a small eddy at the corner of the intake valve and cylinder wall (denoted as "B"), and the flow dragged by the large eddy from the exhaust side (denoted as "C"). In the simulation results, the above features are present but at somewhat different locations. Firstly, the large eddy, which is situated in the middle of the field-of-view of the experiment, is shifted beneath the intake valve in the simulations. In the experiment, the large eddy "A" is generated by the flow sucked in from the intake port and redirected by the slanted wall of the intake valve, whereas the redirected flow by the flat valve in the simulation is blocked by the cylinder head wall between the intake and exhaust valve. Eventually, the large eddy is forced to relocate beneath the intake valve and the size of the vortex is changed. In the DES results, the eddy is present with a complex shape but it can still be identified. Secondly, the flow (feature "C") attracted by the large eddy from the exhaust side is also captured by all turbulence models. The small eddy "B" at the corner of the intake valve and the cylinder wall is shown clearly in the experiment. On the other hand, in most of the simulations, the stream traces have a hairpin shape (highlighted by blue thick arrow) due to the shift of the large eddy towards the intake side. The shift makes the eddy size small; hence, there is a larger space between the large vortex and the wall and the flow does not separate at the wall to generate the small eddy "B". In summary, the flow features in the experimental work can be identified in the simulations. One can conclude that the validation of the flow is satisfactory.

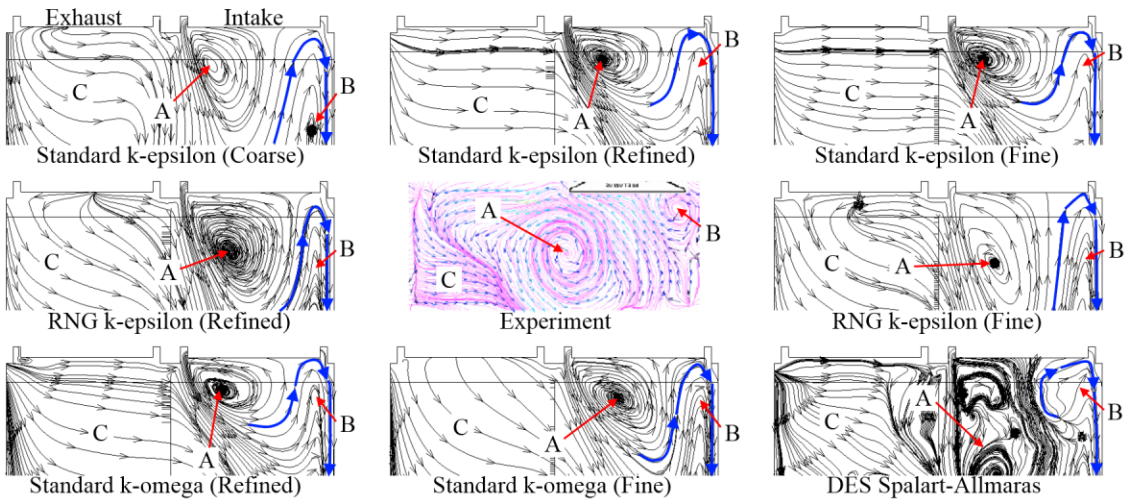

Figure 4.4 – Stream traces of naturally aspirated cases on YZ cut plane at 180 CA (BDC) in present work and the experimental result [52] (centre figure)

4.1.4. Flow Investigation in the Naturally Aspirated Case

Figure 4.5 shows the full size of the field-of-view for each of the turbulence models used. The graph corresponding to each turbulence model can be identified by the diagram in the bottom right-hand corner. Despite the flow similarity in the top one-third of the cylinder, the flow is developed differently in the bottom two-thirds of the domain. The coarse mesh standard k-ε model shows the largest eddies at the bottom right corner (denoted as "D"), the middle right ("E") and the flow dragged into the vortex from left-hand side ("F"). These key features are also identified in the refined RNG k-ε model, refined and fine mesh standard k-ω model and DES model. In the refined and fine mesh standard k-ε model cases, the large eddy at the right-bottom corner is pushed farther up and merged with the small eddy at the middle (denoted as "G"). In the case of the fine mesh RNG k-ε model, the large eddy is no longer observed and is shifted to the exhaust side (the eddy "H").

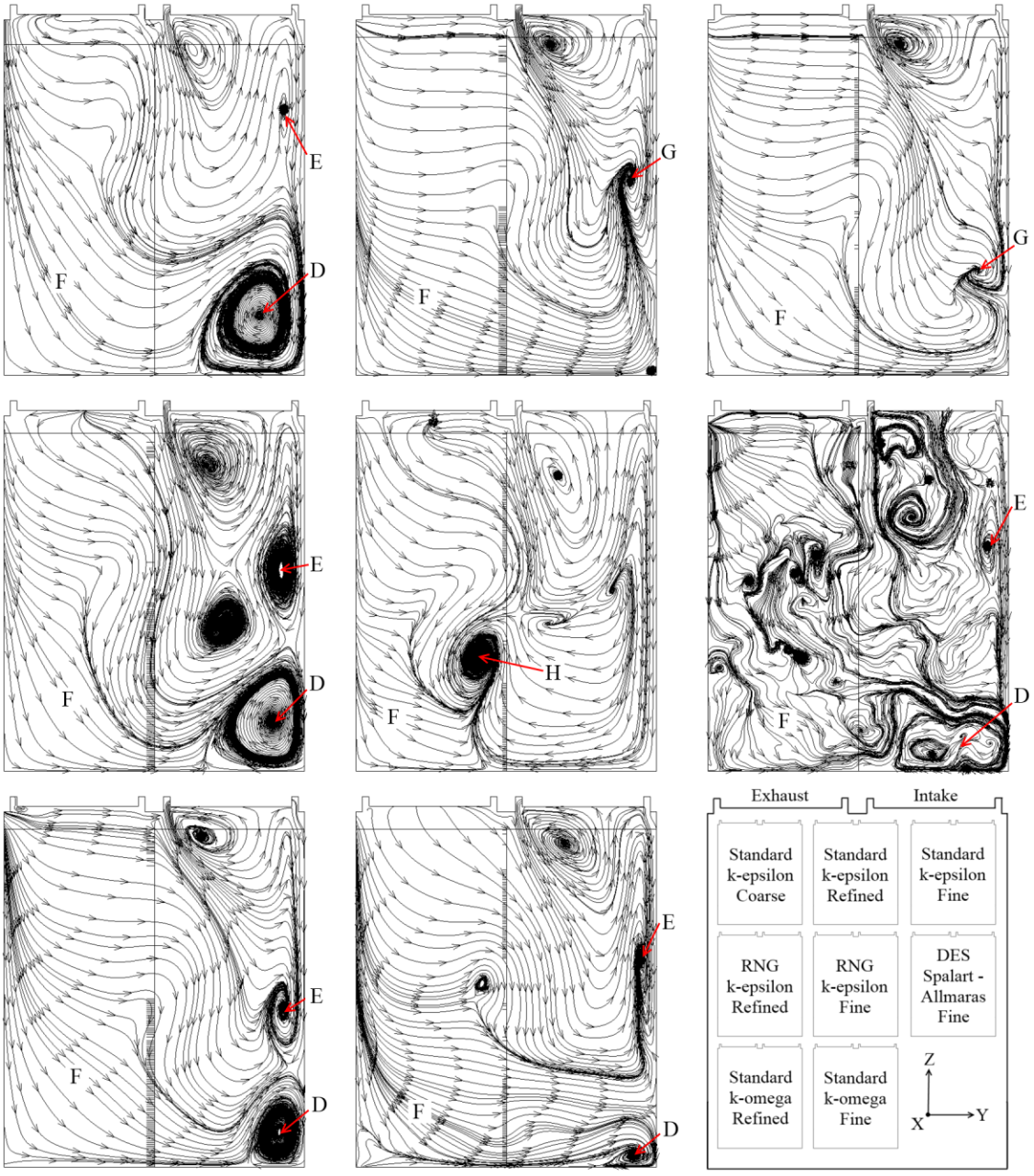

Figure 4.5 – Stream traces of naturally aspirated cases on YZ cut plane at 180 CA (BDC)

The flow structures at the beginning of fuel injection with different turbulence models and mesh sizes are also investigated. Figure 4.6 presents the flow pattern on a plane 5.7 mm offset from the cylinder head. In the coarse standard k-ε model case, symmetric vortices near the intake valve, which are also captured in the small flat piston engine simulations [54], are observed. However, the flow pattern on the cut plane is not symmetric in other cases. Consistency of the pattern is not observed and complexity of

the flow increases by utilizing more computationally expensive turbulence models than the standard k-ε model. Higher velocity is also predicted with the RNG k-ε and the standard k-ω models, but it does not match with the results of the DES.

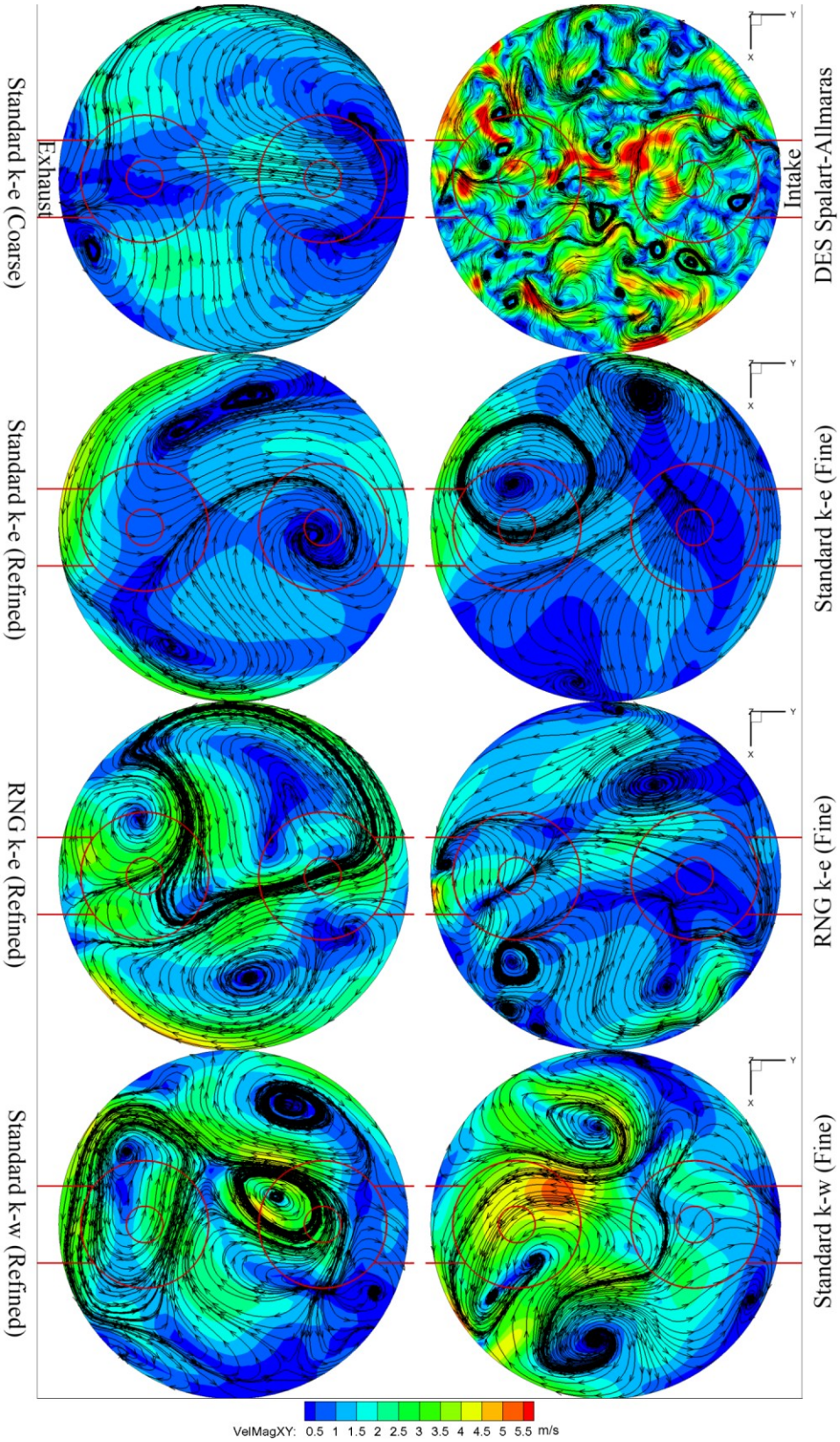

Figure 4.6 – Stream traces of naturally aspirated in-cylinder flow at the beginning of injection on the plane of 5.7 mm offset from the cylinder head

4.1.5. Flow Investigation in the Turbocharged Case

In addition to the naturally aspirated case, turbocharged simulations have also been conducted. The mean in-cylinder pressure curve for the turbocharged case is presented in Figure 4.7. The average peak pressure for all turbulence models is found to be 59.5 bar and all the pressure results are banded within 0.86 % range from the average.

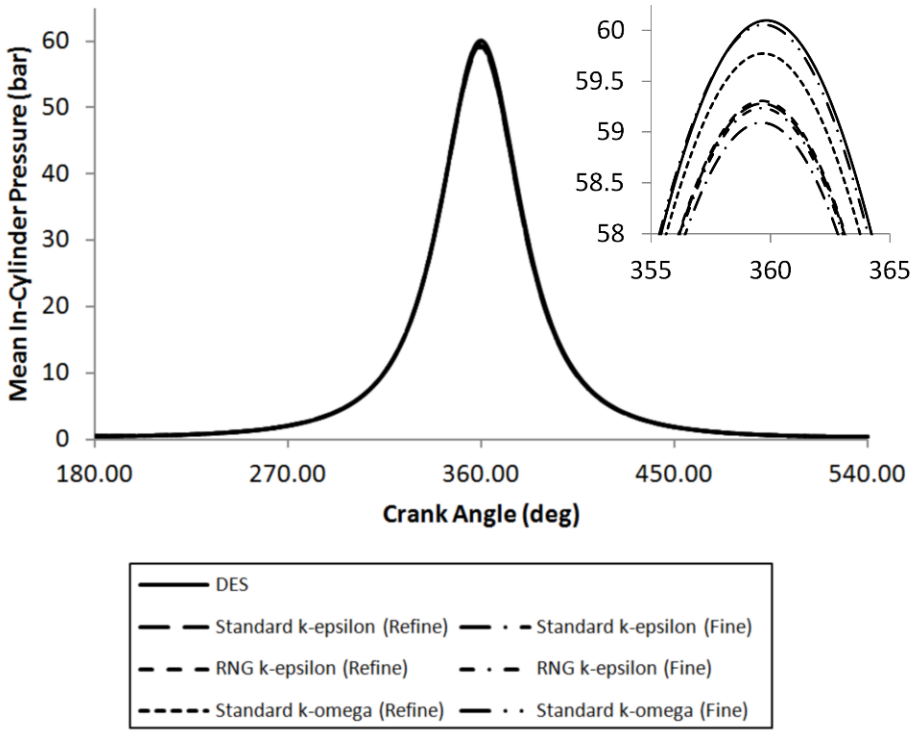

Figure 4.7 – Mean in-cylinder pressure variation of turbocharged case with different turbulence models and mesh sizes

Figure 4.8 shows the stream traces for each turbulence model on the YZ plane at 180 CA (BDC). Similar to the naturally aspirated case, the vortex beneath the intake valve (denoted as "A") is identified at almost the same location in all simulations. Additionally, the flow between the corner of the intake valve and wall (identified as "B") is captured in a hairpin shape and the air at the exhaust side also flows towards the intake side (labeled as "C"). On the other hand, the larger clockwise vortex is found at the bottom-right corner of the cylinder (pointed as "D") in the coarse mesh standard k-ε, both cases of RNG k-ε, and the refined standard k-ω models. The clockwise flow at the bottom-right corner can be captured in the DES model but it is not observed in the refined standard k-ε and the fine standard k-ω models. In the fine standard k-ε model, the vortex

is rotating in counter-clockwise direction due to the early detachment of downward flow from the intake side wall. Separating from the large vortex, the small eddy ("I") is found at the bottom centre in the DES model. Amongst the RANS models, this small eddy is only captured in the RNG k-ε model.

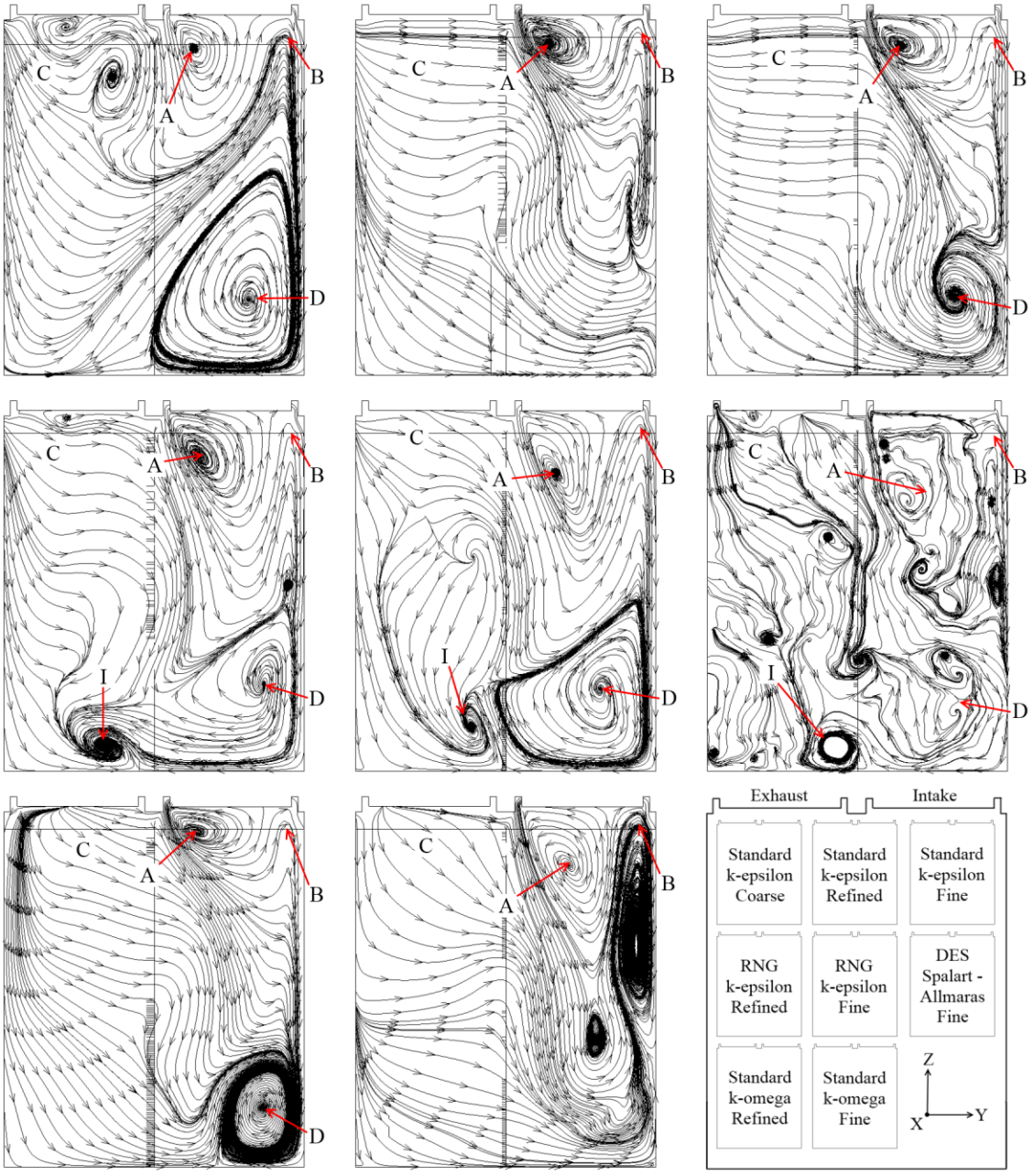

Figure 4.8 – Stream traces of turbocharged cases on YZ cut plane at 180 CA (BDC)

Moreover, turbocharged in-cylinder flows at the beginning of spray injection predicted by different turbulence models and mesh sizes are shown in Fig. 4.9. Similar to

the naturally aspirated case, the symmetry of the flow is only predicted in the coarse standard k-ε model case and not captured in the other simulations. At the same time, the complexity and the velocity magnitude levels are increased in the RNG k-ε and the standard k-ω models. However, the velocity magnitude is not as high as expected by the results of the DES model.

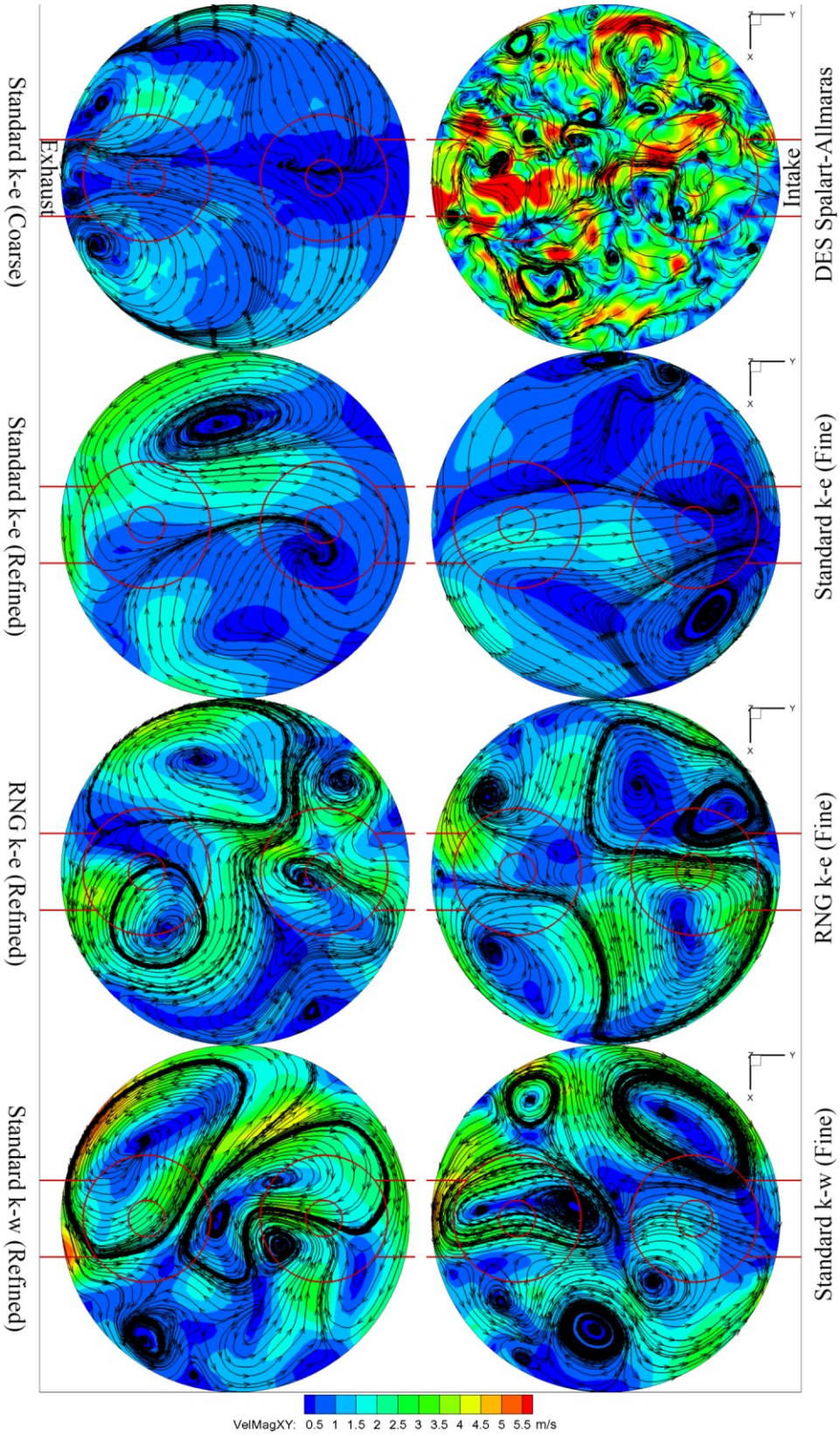

Figure 4.9 – Stream traces of turbocharged in-cylinder flow at the beginning of injection on the plane of 5.7 mm offset from the cylinder head

4.2. Spray Simulations with Ultra-High Injection Pressures using RANS Turbulence Models

Following the validation and investigation of in-cylinder flow, the ultra-high injection pressure sprays are applied to the simulated flow domain of the previous section. For each injection pressure, spray models are set according to the descriptions in Section 3.4. Two breakup models, WAVE and KH-RT, are utilized in this study. To simulate a realistic spray behaviour, the rate of fuel injection is adapted from the work of Zhang et al. [10].

4.2.1. Flow Analysis at the Start of Injection

For the first attempt, the standard k-ε model with the coarse mesh is chosen to examine the effects of the ultra-high injection pressures. Figure 4.10 shows that the sprays emanating from INJ-0 and INJ-180 are exposed to the opposing flow, whereas the spray of INJ-90 will be injected into the downwind and INJ-270 will face a much more complex flow compared to the others. INJ-0 and INJ-180 are sprayed to the upwind flow and fuel injected from INJ-90 and INJ-270 will experience a complex flow pattern with vortices near the wall in the turbocharged case. The cores of the vortices that are captured near the intake port shift to the exhaust port side due to stronger flow by turbocharging.

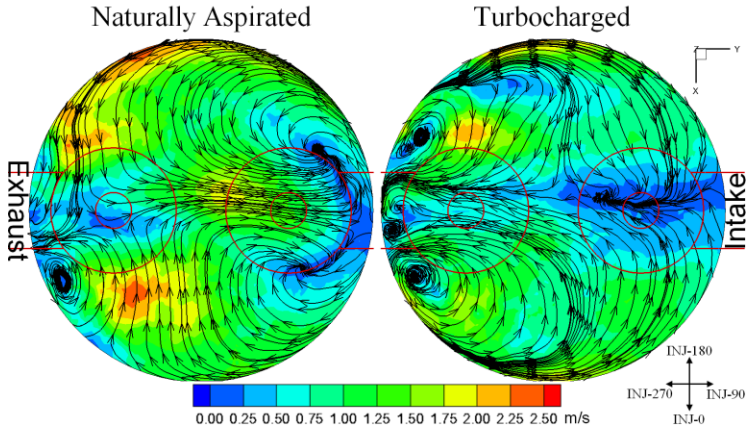

Figure 4.10 – Stream traces superimposed by velocity magnitude contours of naturally aspirated (left) and turbocharged (right) case at the start of injection (-25.5 CA ATDC) on XY plane 5.7 mm offset from the cylinder head surface

4.2.2. In-cylinder Flow and Spray Interaction Analysis

Once the fuel is injected into the chamber, strong flows of the sprays become dominant and build a symmetric flow structure about the axes, as illustrated in Fig. 4.11.

The magnitude of the fuel spray velocity changes linearly by increasing the injection pressure and the backflow is also increased relatively. Hence, our simulations predict higher relative velocity and air entrainment at the edges of sprays, as observed in the experiments of Choi et al [20].

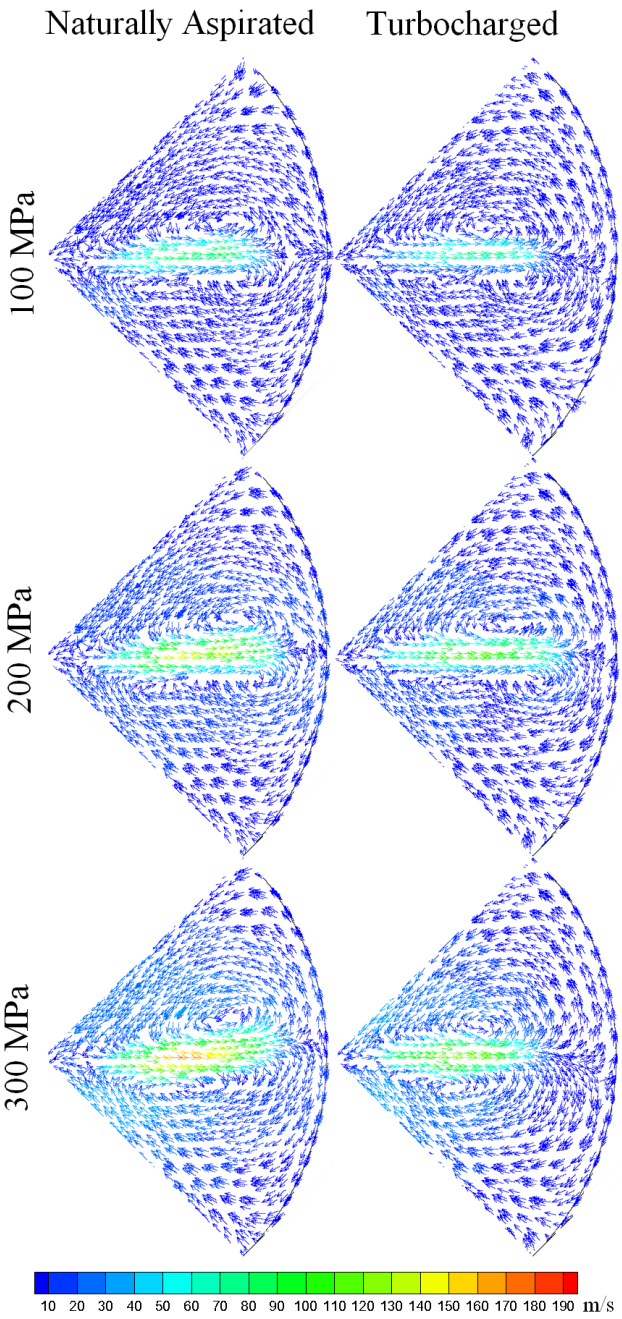

Figure 4.11 – Velocity vector field of INJ-0 superimposed by velocity magnitude contours at 2.5 CA after start of injection (-23.0 CA ATDC) on XY plane 5.7 mm offset from the cylinder head surface

4.2.3. Spray Tip Penetration in Different Conditions

The effects of the breakup models, turbocharging and injection pressures on spray tip penetration are also examined. Figure 4.12 presents the spray tip penetrations from the start of injection (-25.5 CA ATDC) for different injection pressures and densities in the engine model compared with the experimental data of Wang et al. [8] and the simulation in the constant volume chamber as a reference. The similarity between simulation and experimental results in the constant volume case indicates that the spray models are properly set. The reduction of the penetration from the constant volume case to the engine model confirms the effect of the flow inside the cylinder. It is also noticed in Fig. 4.12 that, as expected [17], the KH-RT model cases penetrate slightly less than the WAVE model cases. Since the KH-RT model generally facilitates droplet breakup more quickly, evaporation is induced and penetration is reduced. The smaller droplet size and the effective vaporization generated by the RT mechanism of KH-RT agree with the result of Ricart et al. [55] and Xin et al. [56]. The effect of turbocharging is clearly seen in the slower penetration as shown in Fig. 4.12. As stated in the experimental works [8, 25], high air density induced by turbocharging reduces the spray penetration significantly.

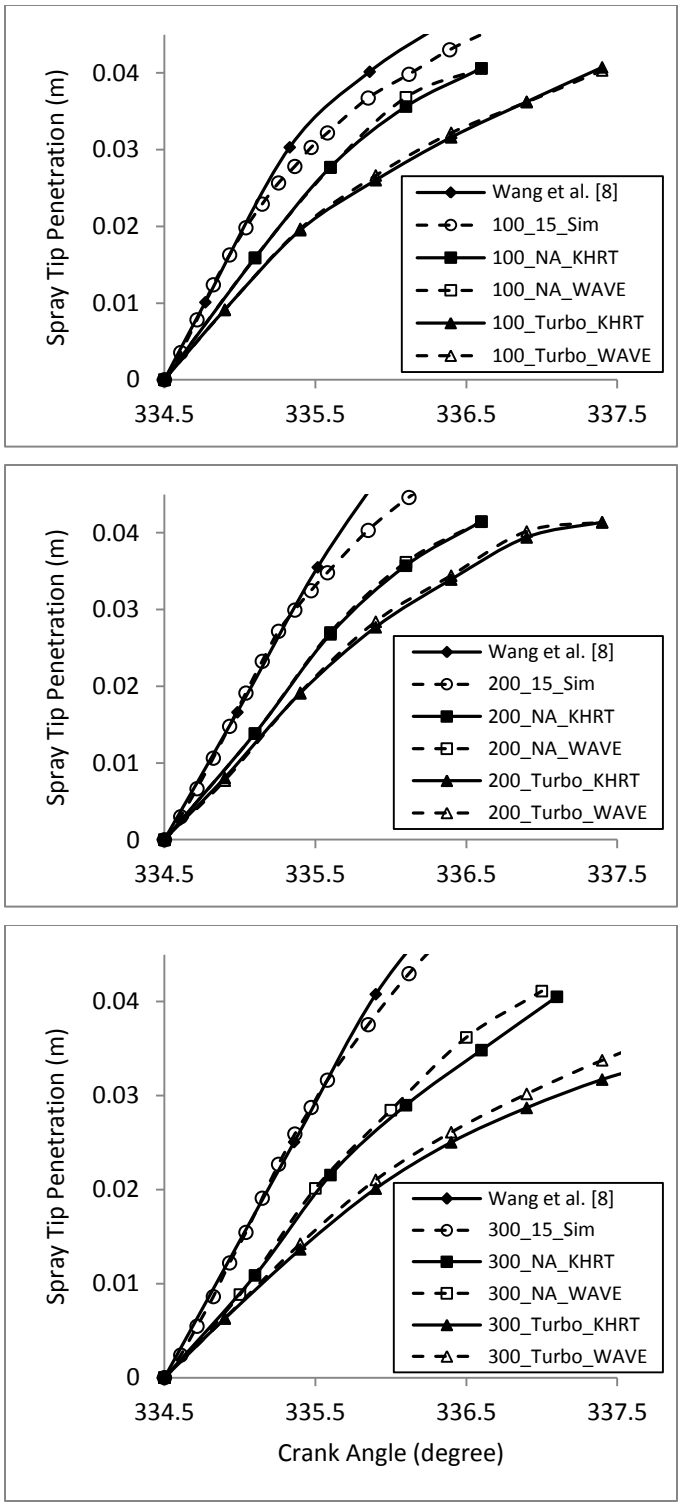

Figure 4.12 – Spray tip penetration variations of INJ-0 at different pressures (100, 200 and 300 MPa) and conditions associated with the comparison between the experiment and simulation in the constant volume vessel

Figure 4.13 presents the variation of each injector's spray penetration in the turbo and non-turbocharged cases. In the naturally aspirated case, as discussed previously in Fig. 4.10, INJ-0 and INJ-180 face upwind flow towards the injection points and hence their penetrations are similar. On the other hand, the penetration of INJ-270 is greatly reduced from the other sprays due to the complexity of the flow and the existence of a vortex near the wall. In the case of turbocharging, the difference is not as large compared to the naturally aspirated case; however, the penetrations of INJ-90 and INJ-270 are reduced since both of them are exposed to a complicated flow. The effect of the vortices on vaporization is consistent with the discussion by Jagus et al. [28]. Also note that the spray penetration at 300 MPa injection pressure is lower than 100 and 200 MPa in the experiment and the computation. Fast atomization induced by higher injection pressure results in droplet vaporization and hence reduces the penetration.

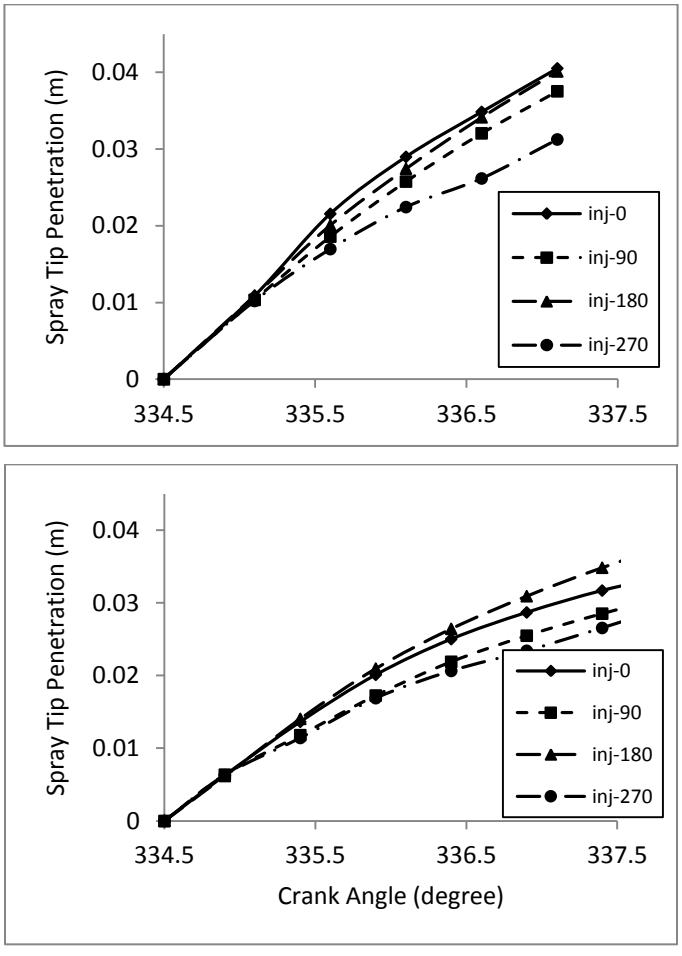

Figure 4.13 – Deviation of spray tip penetration among injectors at 300 MPa injection pressure with naturally aspirated (top) and turbocharged (bottom) cases

4.2.4. Fuel Droplet Size Analysis

The variation of fuel droplet size in time from the start of injection (-25.5 CA ATDC) is presented in Figure 4.14. The result for Sauter mean diameter (SMD) displays a transition of droplet size during the injection. Within 1.0 CA after the start of injection, each model shows rapid decrease of droplet size. The maximum difference of SMD between WAVE and KH-RT models is found to be 19.5% in the 200 MPa turbocharged case. Additionally, the difference between the naturally aspirated and turbocharged cases is not significant since the effect of the air density on SMD is factored by the power 0.06 as defined by the modified SMD correlation of Ejim et al. [57],

$$SMD = 6156\nu^{0.385}\sigma^{0.737}\rho_l^{0.737}\rho_g^{0.06}\Delta P^{-0.54} \quad (39)$$

where SMD is given in μm, kinematic viscosity is in m^2/s, surface tension is in N/m, ρ_l and ρ_g (density of the fuel and air) are in kg/m^3, and ΔP (the pressure difference between injection and ambient pressure) is in bar. Within 1.0 CA after the start of injection, droplet sizes of all models converge to similar diameter and remain constant, as discussed by Nishida et al. [6]. At the 300 MPa injection pressure, the droplets break into smaller size than the SMDs obtained from the Eq. (39) (red-dashed line in Fig. 4.14). Since the equation is developed within 0.5 ms of injection [57], the larger SMDs in the lower injection pressure simulation results are due to the short time period of the breakup process. Nevertheless, the correlation between high spray velocity and small SMD is observed in the results and matches with the study of Post and Abraham [27]. The report by Lee et al. [12] which indicates that no significant change in SMD after 300 MPa of injection pressure is not reproduced in this study since injection pressures higher than 300 MPa have not been considered. However, the reduction of the rate of change in SMD is observed where the rate of reduction from 100 MPa to 200 MPa is 48.9% whereas the change rate from 200 MPa to 300 MPa is 41.8%.

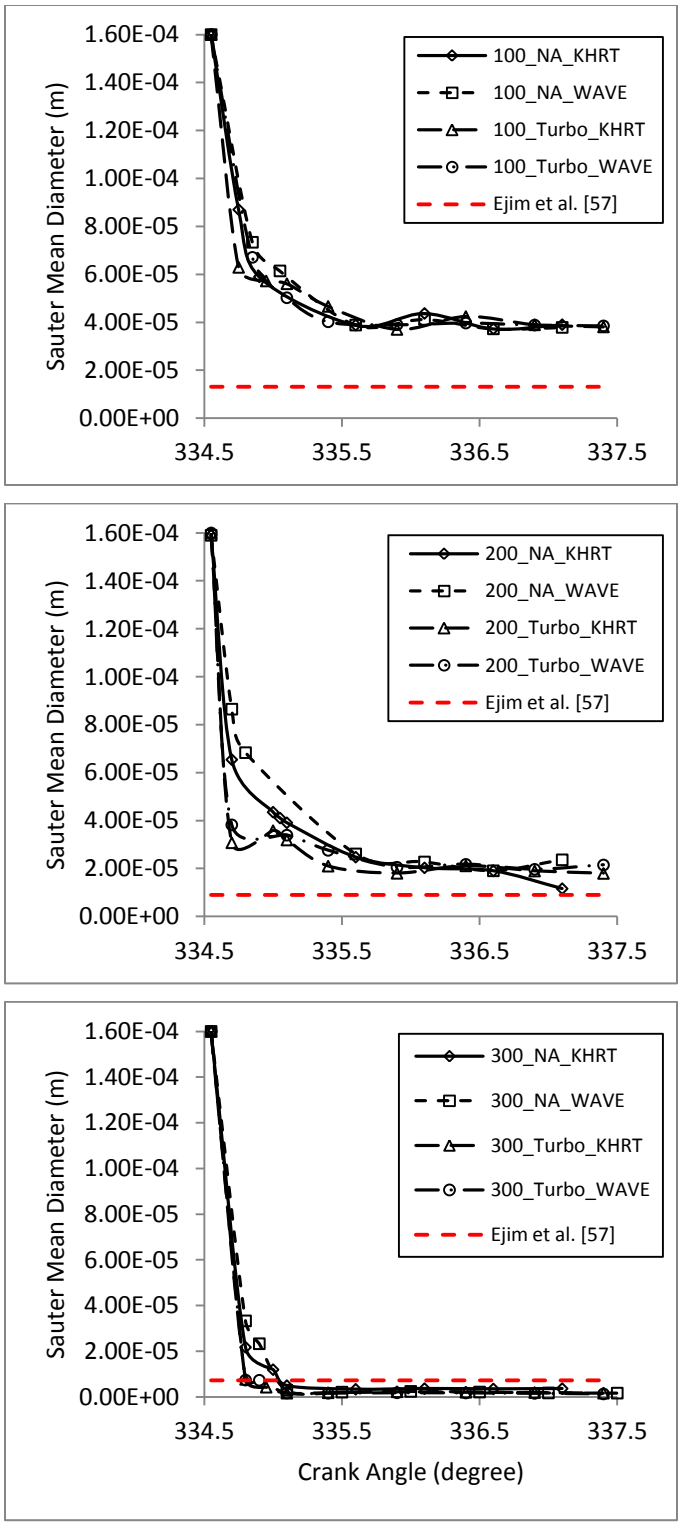

Figure 4.14 – Sauter mean diameter; INJ-0 at different injection pressures (100, 200, and 300 MPa)

4.2.5. Spray Cone Angle Analysis

The dispersion of a spray can be analyzed by the spray cone angles at different conditions. The variation of the cone angle with the injection pressure is shown in Fig. 4.15 and 4.16. The results of larger cone angle at higher injection pressure matches the discussion of Park et al. [58] which indicates that small droplets are found downstream of the cross-flow. In this simulation result the small droplets on the edge of the spray are entrained by the opposing flow, captured by the flow, and enhance the size of the cone angle. The effect of turbocharging is also shown in Fig. 4.15 for the 300 MPa case, which predicts wider cone angle as found by Naber and Siebers [25], whereas no change or even narrower cone angles are found to occur in the 100 and 200 MPa cases. It appears that the sprays are not yet fully developed at 2.5 CA after the start of injection for these cases. The change of cone angle in time shows oscillation during the injection but it is likely to maintain the constant value right after the start of injection, consistent with the study of Naber and Siebers' work [25].

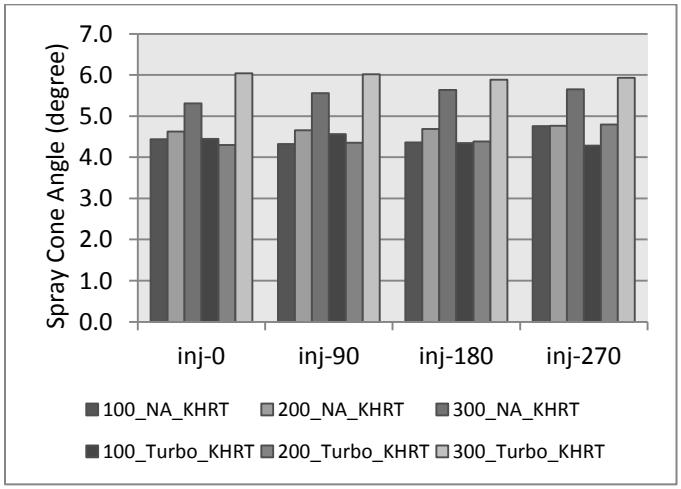

Figure 4.15 – Variations of spray cone angle in different cases and injectors at 2.5 CA after start of injection (-23.0 CA ATDC)

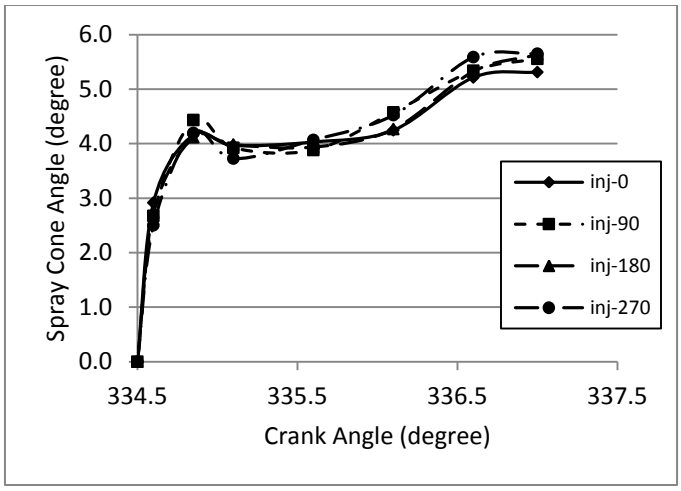

Figure 4.16 –Development of spray cone angle of 300 MPa injection pressure until sprays impinge to the walls

4.2.6. Fuel/Air Mixture Analysis

Finally, the fuel mass fraction for each case is examined. Figure 4.17 shows the sections of XY, YZ, and ZX plane at two different instances. In each set of figures shown, the top image refers to the YZ plane, the left image shows the ZX plane and the right image presents the XY plane, respectively (see the diagram in the bottom right-hand corner). A larger portion of the fuel mass contour in the 300 MPa cases at 2.5 CA after start of injection indicates a fast injection process due to high injection pressure. Fast penetration of spray at high injection pressure was also observed by Tao and Bergstrand [13]. The completion of injection at an early stage results in extra time for fuel-air mixing and contributes to a better mixture formation at combustion as reported by Yokota et al. [4]. The uniform color contours of the high injection pressure cases at TDC indicates an even distributions and lean mixture of fuel in the chamber.

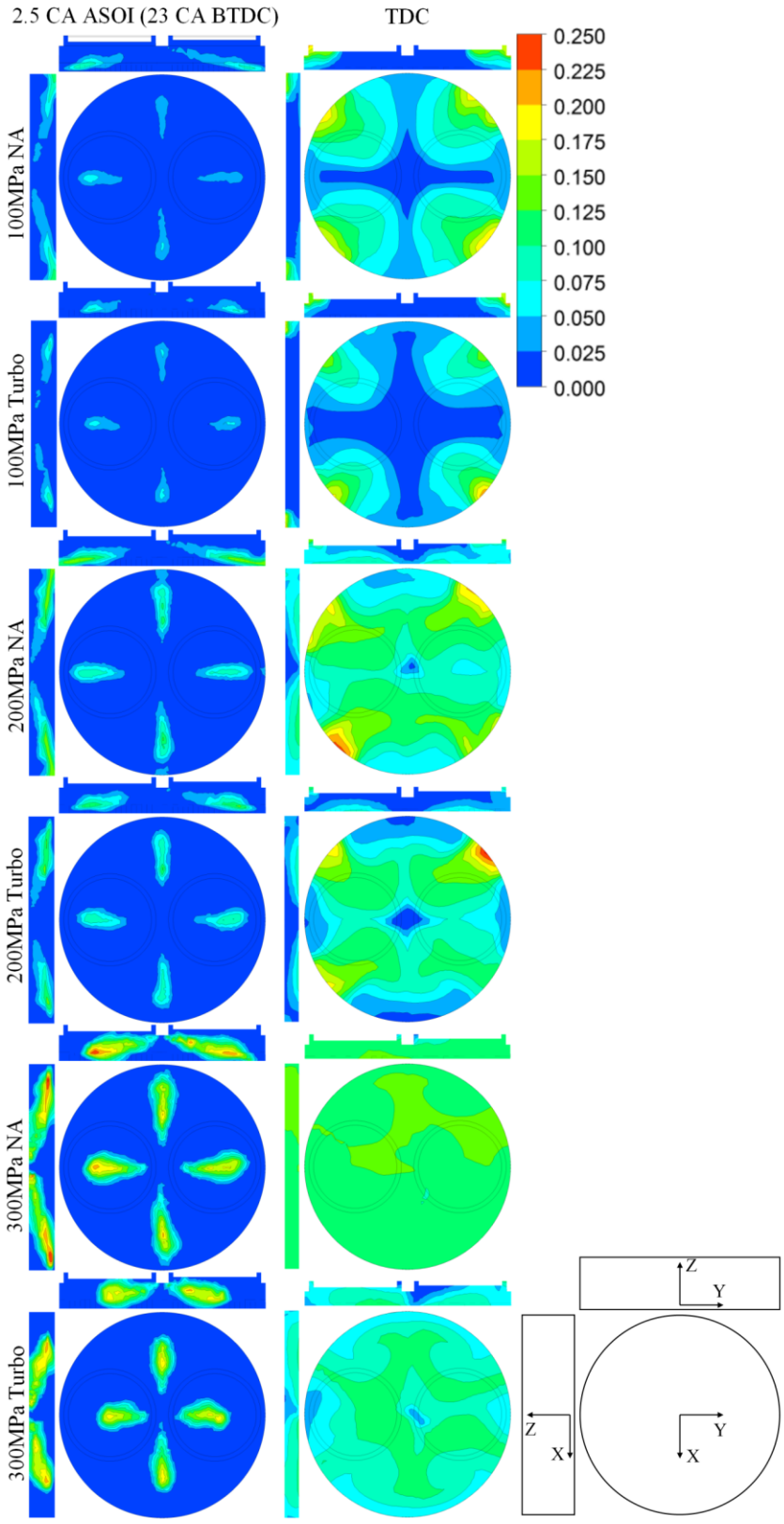

Figure 4.17 – Contours of fuel mass fraction at two different times

4.2.7. Convergence Issues

Following the successful preliminary simulation of the sprays with the coarse mesh standard k-ε model, a divergence issue arose in the spray simulations using the RNG k-ε and the standard k-ω turbulence models. Divergences in species and temperature were detected during the simulations with both of these turbulence models. In an attempt to overcome this problem, finer time-step sizes (1.0, 5.0 and 10.0 μs) were examined in the refined and fine mesh, even though the Courant numbers in both models were already sufficiently lower than one [29]. However, none of the smaller time-step sizes made the simulations successful. In the next section, the convergence issue is investigated in a simple geometry. The principal factors affecting convergence, i.e., the turbulence models, mesh types and mesh sizes are studied.

4.3. Role of Turbulence Models and Mesh Configurations in the Constant Volume Chamber Simulations

As indicated in Section 4.2, the RANS turbulence models other than the standard k-ε diverged. In this section, further investigations on the spray modeling in different type of meshes are carried out. To allow a clear picture of the differentiation of mesh type and size, the constant volume chamber used in the grid independency test is employed herein. The spray model with 300 MPa injection pressure is applied in all cases. The tests are conducted with three turbulence models, the standard k-ε, the RNG k-ε and the standard k-ω model, in two mesh sizes and three mesh types. Two different time-step sizes are also investigated in some cases.

The mesh files are again generated by means of GAMBIT. One structure mesh and two unstructured meshes have been created; one of unstructured meshes is generated by Pave and the other uses the Map Split scheme. Pave is a meshing scheme to create the face mesh in an irregular triangular shape whereas Map Split creates a quadrilateral mesh and splits cells diagonally into triangular elements. The number of structured cells in the simulations is 1.2 million, which has been optimized in the grid independency test. In case of an unstructured mesh, the number of nodes on each edge is reduced because the cell number is eventually increased by utilizing triangular cells (see Fig. 4.18). The coarse unstructured mesh with Map Split scheme has 40 nodal points on each edge whereas the fine mesh has 60 grid points on every edge. The unstructured mesh with

Pave scheme has 80 nodes in the radial direction and 60 nodes in the axial direction. The total cell number becomes 0.32 million for the coarse Map Split mesh, 1.11 million for the fine Map Split mesh, and 1.31 million for the Pave mesh. The summary of the mesh configurations can be found in Table 4.2.

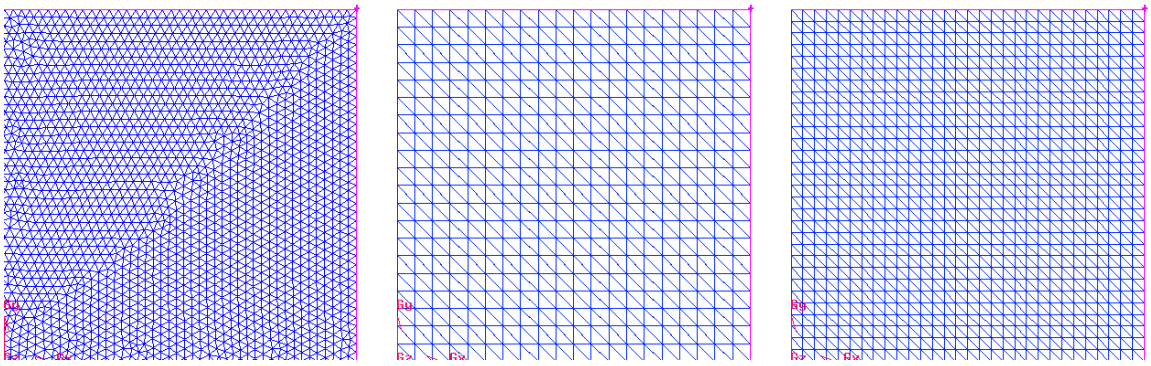

Figure 4.18 – Unstructured mesh in the constant volume chamber with Pave, Map Split (coarse), and Map Split (fine) scheme (view left to right)

Table 4-2 – Summary of tested unstructured mesh sizes

	No. of grid points (W×D×H)	No. of cells
Pave	80 × 80 × 60	1.31 million
Map Split (Coarse)	40 × 40 × 40	0.32 million
Map Split (Fine)	60 × 60 × 60	1.11 million

A summary of the test results are shown in Table 4.3. The simulations are able to be completed in the case of the structured meshes, whereas most of the simulations with unstructured meshes failed. Furthermore, different time-step sizes (0.5 and 0.1 μs) have been applied for the fine Map Split mesh but no improvement was observed.

Table 4-3 – Test summary of turbulence models and mesh qualities

	Quadrilateral	Tetrahedral		
Turbulence models	Structured	Pave (Fine)	Map Split (Coarse)	Map Split (Fine)
Standard k-ε	✓	X	X	X
RNG k-ε	✓	X	X	✓
Standard k-ω	✓	X	X	X

Figures 4.19, 4.20 and 4.21 show the spray tip penetration for each combination of turbulence model and mesh type. Even though all the structured mesh cases and the RNG k-ε model with the fine Map Split mesh case is able to accomplish the transient spray simulation, the simulation results deviate drastically from the experimental data [8] except for the structured mesh standard k-ε model. It is understood that the structured mesh case with the standard k-ε model has the best match with the experiment data since the spray model parameters are set by the turbulence model. The structured mesh with the standard k-ω model is short in penetration and a large cloud of spray is observed even at the early stage of injection. On the other hand, the RNG k-ε model does not induce breakup of droplets and does not even follow the characteristics of the spray tip penetration. None of the unstructured mesh cases are able to represent the true spray characteristics.

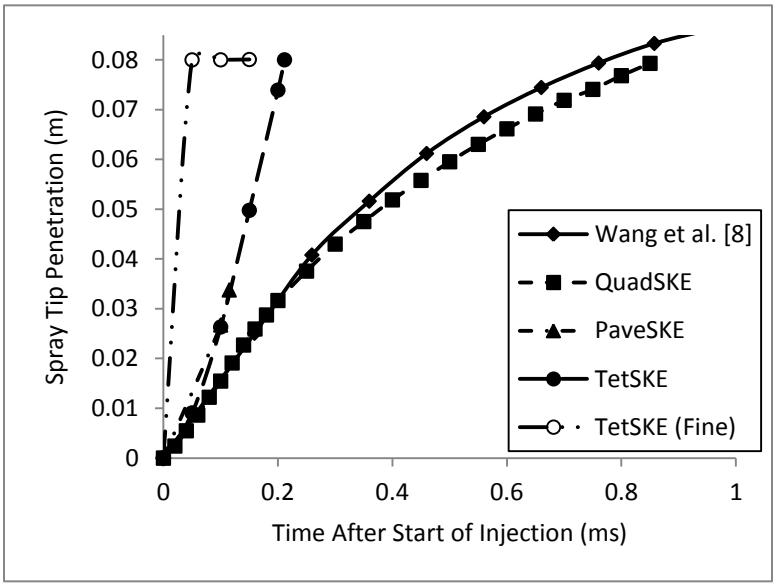

Figure 4.19 – Spray tip penetration using standard k-ε model

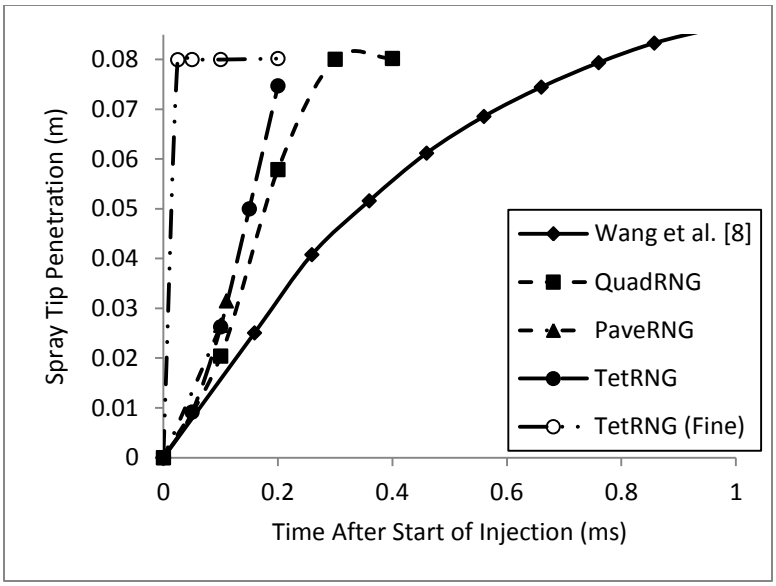

Figure 4.20 – Spray tip penetration using RNG k-ε model

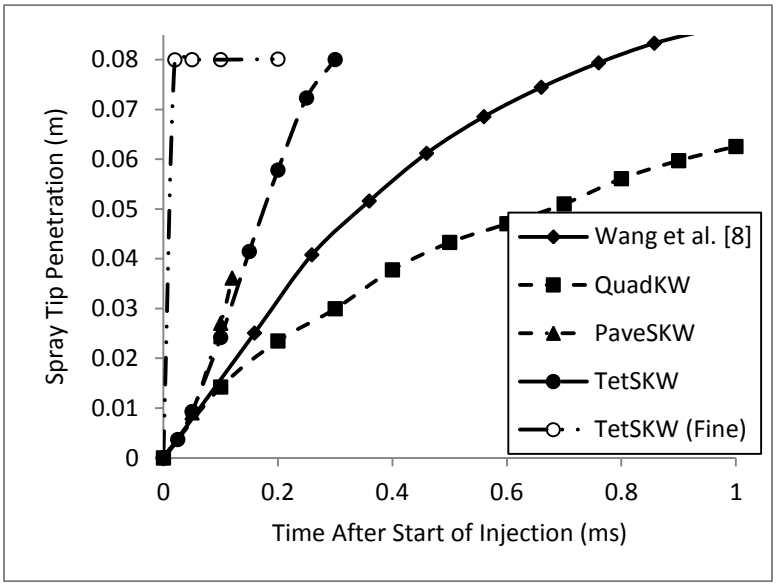

Figure 4.21 – Spray tip penetration using standard k-ω model

Under different combinations of turbulence models, mesh types and mesh sizes, it is noted that the spray model with a tetrahedral mesh does not perform well. A similar issue was reported by Imamori et al. [59] using the KIVA-4 code. It was stated that the gas phase and droplet behaviour are strongly affected by the high-dependency of the Lagrangian-Droplet and Eulerian-Fluid (LDEF) spray model on the mesh [35, 60-62]. Additionally, the breakup model in the RNG k-ε and the standard k-ω models behaves differently compared to the experiment or the standard k-ε model. This implies that the

spray model parameters have to be tuned for each turbulence model to make the simulations reliable to estimate the fuel/air mixture.

4.4. Summary

In this chapter, the flow inside the cylinder and the fuel mixture process with the air has been studied. It has been shown that the standard k-ε model is capable of predicting some key flow characteristics which are also identified in similar experimental studies and LES simulations. The simulations are repeated by utilizing different turbulence models; however, the RNG k-ε and the standard k-ω turbulence models require a finer mesh size to accomplish the end result. The flow features in some turbulence models are captured differently at the bottom two-thirds of the cylinder at BDC but the flow structures at the top one-third are found to be similar to the experiments.

Diesel fuel sprays are incorporated into the flow field at 25.5 CA before TDC. Fuel spray with ultra-high injection pressures presents the benefit of the high pressure for short injection time, long mixing duration and uniform mixture. The spray model is also found to be sensitive to mesh configurations which can influence the possibility of inaccurate results. In conclusion, further study of the mesh dependency in spray modeling is recommended.

Chapter 5. Conclusions

The effects of ultra-high injection pressure sprays are studied in a simplified engine geometry. The engine model is properly set up and different conditions are examined by varying the injection pressure, spray model and inlet pressure. The flow inside the cylinder calculated by RANS models and DES is validated with the experimental data. The simple engine geometry does not induce strong swirl and tumble motion but generates a complicated flow at the time of injection. From this study, in the ultra-high injection pressure cases, the following conclusions regarding spray and flow characteristics can be made, and are in agreement with the results reported by other researchers.

- Eddies near the valve in all RANS models and DES appear to be consistent with those of experimental data. The changes in location, shape and size of eddies in each turbulence model are likely caused by geometrical difference between the experiment and simulation.
- The RNG k-ε and standard k-ω turbulence models require the mesh to be refined compared with the standard k-ε model.
- In the naturally aspirated case, the standard k-ω model estimates the complicated flow inside the cylinder which is also observed in the DES model. However, the magnitude of flow deviates from the calculations in the k-ε and DES models.
- RNG k-ε model, on the other hand, is able to capture some flow features that are present in the DES model in the turbocharged case. The standard k-ε model cannot predict the features properly near the piston wall.
- KH-RT hybrid breakup model estimates smaller droplets and larger dispersion than the WAVE model. However, the spray characteristics calculated by the WAVE model are not significantly different from KH-RT since the breakup constant is found by using the correlation to RT constants.
- Four sprays injected in the chamber are exposed to different flow structures and found to be in good agreement with other studies on spray characteristics such as spray tip penetration, Sauter mean diameter and spray cone angle. The ultra-high

injection pressure breaks droplets to smaller sizes; thus, reducing spray penetration and a higher dispersion rate is predicted. Also, the droplet vaporization is accelerated by the existence of vortices in the direction of the sprays.

- The rate of SMD change is reduced at higher injection pressure, as reported by Lee et al. [12]. However, the SMD limitation which Lee et al. [12] have observed is not detected in this study.
- Turbocharging is found to reduce spray tip penetration and to dissipate the angle of spray. On the other hand, the effect of turbocharging on SMD is not predicted as indicated in the correlation stated by Ejim et al. [57].
- The ultra-high injection pressure promotes a faster and more effective mixture process and allows extending the time to form the mixture of air-fuel.

Divergence has been detected during the engine simulations when the spray model is applied in the RNG k-ε and standard k-ω model simulations. Further investigations into the role of turbulence models and mesh type and size have been carried out. The investigations in the constant volume chamber show that the spray model does not behave as expected with the unstructured meshed zones. On the other hand, RANS model is globally functional to predict the spray characteristics in the structured mesh zones; however, it still requires tunings for each model to achieve good estimation.

In conclusion, it is found that the standard k-ε model is flexible to operate different models in FLUENT. To examine further detail of flow and spray characteristics, more investigations are required to understand the functionality of turbulence models associated with spray injection models and mesh configurations.

As a recommendation for future work, it is suggested to continue the investigations on the interaction between the turbulence model and the spray model with structured mesh in the engine model. Even though a structured mesh has less flexibility and the hybrid mesh is recommended by the software itself, it would be interesting to present results comparing the structured and unstructured meshes. Furthermore, it should also be beneficial to simulate these flows with much more expensive turbulence models, such as Large Eddy Simulation (LES), to study the flow structure in details. Moreover, it would be convenient to have additional experimental data for the in-cylinder flow

investigations to determine the quality of the numerical simulations. Finally, the further analysis in the ultra-high injection pressure higher than 300 MPa is interested in by taking an advantage of CFD capability.

References

[1] *Emission Standards United States.* http://www.dieselnet.com/standards/us/, 2010.

[2] Heywood, J.B. *Internal Combustion Engine Fundamentals*. McGraw-Hill, New York, 1988.

[3] Kato, T., Tsujimura, K., Shintani, M., Minami, T., and Yamaguchi, I. Spray Characteristics and Combustion Improvement of D.I. Diesel Engine with High Pressure Fuel Injection. *SAE Technical Paper 890265*, 1989.

[4] Yokota, H., Kamimoto, T., Kosaka, H., and Tsujimura, K. Fast Burning and Reduced Soot Formation Via Ultra-High Pressure Diesel Fuel Injection. *SAE Paper No. 910225*, 1991.

[5] Kuti, O.A., Xiangang, W.G., Zhang, W., Nishida, K., and Huang, Z.H. Characteristics of the Ignition and Combustion of Biodiesel Fuel Spray Injected by a Common-Rail Injection System for a Direct-Injection Diesel Engine. *Proceeding of the Institution of Mechanical Engineers, Part D: Journal of Automobile Engineering*, 224, pp. 1581-1596, 2010.

[6] Nishida, K., Zhang, W., and Manabe, T. Effects of Micro-Hole and Ultra-High Injeciton Pressure on Mixture Properties of D.I. Diesel Spray. *SAE Paper No. 2007-01-1890*, 2007.

[7] Wang, X., Kuti, O.A., Zhang, W., Nishida, K., and Huang, Z. Effect of Injection Pressure on Flame and Soot Characteristics of the Biodiesel Fuel Spray. *Combustion Science and Technology*, 182, pp. 1369-1390, 2010.

[8] Wang, X., Huang, Z., Kuti, O.A., Zhang, W., and Nishida, K. Experimental and Analytical Study on Biodiesel and Diesel Spray Characteristics under Ultra-High Injection Pressure. *International Journal of Heat and Fluid Flow*, 31, pp. 659-666, 2010.

[9] Wang, X., Huang, Z., Zhang, W., Kuti, O.A., and Nishida, K. Effects of Ultra-High Injection Pressure and Micro-Hole Nozzle on Flame Structure and Soot Formation of Impinging Diesel Spray. *Applied Energy*, 88, pp. 1620-1628, 2011.

[10] Zhang, W., Nishida, K., Gao, J., and Miura, D. An Experimental Study on Flat-Wall-Impinging Spray of Microhole Nozzles under Ultra-High Injection Pressures.

Proceeding of the Institution of Mechanical Engineers, Part D: Journal of Automobile Engineering, 222, pp. 1731-1741, 2008.

[11] Zhang, W., Nishida, K., and Tian, J.P. *Spray-Spray and Spray-Wall Interactions in Diesel Sprays from Micro-Hole Nozzles under Ultra-High Injection Pressures.* 11th Triennial International Annual Conference on Liquid Atomization and Spray SystemsVail, Colorado, 2009.

[12] Lee, S.H., Jeong, D.Y., Lee, J.T., Ryou, H.S., and Hong, K. Investigation on Spray Characteristics under Ultra-High Injection Pressure Conditions. *International Journal of Automotive Technology*, 6(2), pp. 125-131, 2005.

[13] Tao, F., and Bergstrand, P. Effect of Ultra-High Injection Pressure on Diesel Ignition and Flame under High-Boost Conditions. *SAE Paper No. 2008-01-1603*, 2008.

[14] Lin, S.P., and Reitz, R.D. Drop and Spray Formation from a Liquid Jet. *Annual Review of Fluid Mechanics*, 30, pp. 85-105, 1998.

[15] Jiang, X., Siamas, G.A., Jagus, K., and Karayiannis, T.G. Physical Modelling and Advanced Simulations of Gas-Liquid Two-Phase Jet Flows in Atomization and Sprays. *Progress in Energy and Combustion Science*, 36, pp. 131-167, 2010.

[16] Djavareshkian, M.H., and Ghasemi, A. Investigation of Jet Break-up Process in Diesel Engine Spray Modelling. *Journal of Applied Sciences*, 9(11), pp. 2078-2087, 2009.

[17] Hossainpour, S., and Binesh, A.R. Investigation of Fuel Spray Atomization in a DI Heavy-Duty Diesel Engine and Comparison of Various Spray Breakup Models. *Fuel*, 88, pp. 799-805, 2009.

[18] Karrholm, F.P., and Nordin, N. Numerical Investigation of Mesh/Turbulence/Spray Interaction for Diesel Applications. *SAE Paper No. 2005-01-2115*, 2005.

[19] Ghasemi, A., and Djavareshkian, M.H. Investigation of the Effect of Natural Gas Equivalence Ratio and Piston Bowl Flow Field on Combustion and Pollutant Formation of a DI Dual Fuel Engine. *Journal of Applied Sciences*, 10, pp. 1-11, 2010.

[20] Choi, W., and Choi, B.C. Estimation of the Air Entrainment Characteristics of a Transient High-Pressure Diesel Spray. *Proceedings of the Institution of Mechanical Engineers, Part D: Journal of Automobile Engineering*, 219, pp. 1025-1036, 2005.

[21] Desantes, J.M., Arregle, J., Lopez, J.J., and Garcia, J.M. Turbulent Gas Jets and Diesel-Like Sprays in a Crossflow: A Study on Axis Deflection and Air Entrainment. *Fuel*, 85, pp. 2120-2132, 2006.

[22] Mccracken, M.E., and Abraham, J. Characterization of Mixing Enhancement in Swirl-Spray Interactions in Diesel Engines. *Combustion Science and Technology*, 174(10), pp. 93-124, 2002.

[23] Park, S.W., and Lee, C.S. Investigation of Atomization and Evaporation Characteristics of High-Pressure Injection Diesel Spray Using Kelvin-Helmholtz Instability/Droplet Deformation and Break-up Competition Model. *Proceeding of the Institution of Mechanical Engineers, Part D: Journal of Automobile Engineering*, 218(7), pp. 767-777, 2004.

[24] Iyer, V., and Abraham, J. Penetration and Dispersion of Transient Gas Jets and Sprays. *Combustion Science and Technology*, 130, pp. 315-334, 1997.

[25] Naber, J.D., and Siebers, D.L. Effects of Gas Density and Vaporization on Penetration and Dispersion of Diesel Sprays. *SAE Paper No. 960034*, 1996.

[26] Kennaird, D.A., Crua, C., Lacoste, J., Heikal, M.R., Gold, M.R., and Jackson, N.S. In-Cylinder Penetration and Break-up of Diesel Sprays Using a Common-Rail Injection System. *SAE Paper No. 2002-01-1626*, 2002.

[27] Post, S.L., and Abraham, J. Modeling the Outcome of Drop-Drop Collisions in Diesel Sprays. *International Journal of Multiphase Flow*, 28, pp. 997-1019, 2002.

[28] Jagus, K., Jiang, X., Dober, G., Greeves, G., Milanovic, N., and Zhao, H. Assessment of Large-Eddy Simulation Feasibility in Modelling the Unsteady Diesel Fuel Injection and Mixing in a High-Speed Direct-Injection Engine. *Proceedings of the Institution of Mechanical Engineers, Part D: Journal of Automobile Engineering*, 223, pp. 1033-1048, 2009.

[29] Hoffmann, K.A., and Chiang, S.T. *Computational Fluid Dynamics*. Engineering Education System, Kansas, 2004.

[30] Versteeg, H.K., and Malalasekera, W. *An Introduction to Computational Fluid Dynamics the Finite Volume Method.* Pearson Education Limited, UK, 2007.

[31] Spalart, P.R. Detached-Eddy Simulation. *Annual Review of Fluid Mechanics*, 41, pp. 181-204, 2009.

[32] Travin, A.K., Shur, M.L., Strelets, M.K., and Spalart, P.R. Detached-Eddy Simulations Past a Circular Cylinder. *Flow, Turbulence and Combustion*, 63, pp. 293-313, 1999.

[33] *ANSYS FLUENT Theory Guide.* ANSYS, Inc., Canonsburg, PA, 2010.

[34] Nijdam, J.J., Guo, B., Fletcher, D.F., and Langrish, T.a.G. Lagrangian and Eulerian Models for Simulating Turbulent Dispersion and Coalescence of Droplets within a Spray. *Applied Mathematical Modelling*, 30, pp. 1196-1211, 2006.

[35] Schmidt, D.P., and Rutland, C.J. A New Droplet Collision Algorithm. *Journal of Computational Physics*, 164, pp. 62-80, 2000.

[36] Sazhin, S.S. Advanced Models of Fuel Droplet Heating and Evaporation. *Progress in Energy and Combustion Science*, 32, pp. 162-214, 2006.

[37] O'rourke, P.J., and Amsden, A.A. The Tab Method for Numerical Calculation of Spray Droplet Breakup. *SAE Technical Paper 872089*, 1987.

[38] Reitz, R.D. Modeling Atomization Processes in High-Pressure Vaporizing Sprays. *Atomisation and Spray Technology*, 3, pp. 309-337, 1987.

[39] Hwang, S.S., Liu, Z., and Reitz, R.D. Breakup Mechanisms and Drag Coefficients of High-Speed Vaporizing Liquid Drops. *Atomization and Sprays*, 6, pp. 353-376, 1996.

[40] Lee, C.S., Kim, H.J., and Park, S.W. Atomization Characteristics and Prediction Accuracies of Hybrid Break-up Models for a Gasoline Direct Injection Spray. *Proceeding of the Institution of Mechanical Engineers, Part D: Journal of Automobile Engineering*, 218(9), pp. 1041-1053, 2004.

[41] Patterson, M.A., and Reitz, R.D. Modeling the Effects of Fuel Spray Characteristics on Diesel Engine Combustion and Emission. *SAE Paper No. 980131*, 1998.

[42] Liu, A.B., Mather, D., and Reitz, R.D. Modelling the Effects of Drop Drag and Breakup on Fuel Sprays. *SAE Paper No. 930072*, 1993.

[43] Liu, F.-S., Zhou, L., Sun, B.-G., Li, Z.-J., and Harold, J.S. Validation and Modification of Wave Spray Model for Diesel Combustion Simulation. *Fuel*, 87, pp. 3420-3427, 2008.

[44] Levich, V.G. *Physicochemical Hydrodynamics.* Prentice Hall, New Jersey, 1962.

[45] Hiroyasu, H., and Arai, M. Structures of Fuel Sprays in Diesel Engines. *SAE Paper No. 900475*, 1990.

[46] Senecal, P.K. *Development of a Methodology for Internal Combustion Engine Design Using Multi-Dimensional Modeling with Validation through Experiments.* Ph.D., University of Wisconsin - Madison, Madison, Wisconsin, 2000.

[47] Amsden, A.A. *KIVA-3V: A Block-Structured KIVA Program for Engines with Vertical or Canted Valves.* Los Alamos National Laboratory, 1997.

[48] Abraham, J., and Magi, V. Computations of Transient Jets: RNG k-e Model Versus Standard k-e Model. *SAE Paper NO. 970885*, pp. 113-123, 1997.

[49] Sone, K., and Menon, S. Effect of Subgrid Modeling on the in-Cylinder Unsteady Mixing Process in a Direct Injection Engine. *Journal of Engineering for Gas Turbines and Power*, 125, pp. 435-443, 2003.

[50] Jonnalagedda, S., Nguyen, A.T., Zhou, B., and Sobiesiak, A. *Numerical Studies on HCCI Engine Combustion.* CFD Society of Canada 2010London, Ontario, Canada, 2010.

[51] Jeng, Y.L., Chen, R.C., and Chang, C.H. Studies of Tumbling Motion Generated During Intake in a Bowl-in-Piston Engine. *Journal of Marine Science and Technology*, 7(1), pp. 52-64, 1999.

[52] Krishna, B.M., and Mallikarjuna, J.M. Comparative Study of in-Cylinder Tumble Flows in an Internal Combustion Engine Using Different Piston Shapes - an Insight Using Particle Image Velocimetry. *Experiments in Fluids*, 48, pp. 863-874, 2010.

[53] Krishna, B.M., and Mallikarjuna, J.M. Effect of Engine Speed on in-Cylinder Tumble Flows in a Motored Internal Combustion Engine - an Experimental

Investigation Using Particle Image Velocimetry. *Journal of Applied Fluid Mechanics*, 4(1), pp. 1-14, 2011.

[54] Bianchi, G.M., Cantore, G., Parmeggiani, P., and Michelassi, V. On Application of Nonlinear k-e Models for Internal Combustion Engine Flows. *Journal of Engineering for Gas Turbines and Power*, 124, pp. 668-677, 2002.

[55] Ricart, L.M., Reitz, R.D., and Dec, J.E. Comparisons of Diesel Spray Liquid Penetration and Vapor Fuel Distributions with in-Cylinder Optical Measurements. *Journal of Engineering for Gas Turbines and Power*, 122(4), pp. 588-595, 2000.

[56] Xin, J., Ricart, L., and Reitz, R.D. Computer Modeling of Diesel Spray Atomization and Combustion. *Combustion Science and Technology*, 137, pp. 171-194, 1998.

[57] Ejim, C.E., Fleck, B.A., and Amirfazli, A. Analytical Study for Atomization of Biodiesels and Their Blends in a Typical Injector: Surface Tension and Viscosity Effects. *Fuel*, 86, pp. 1534-1544, 2007.

[58] Park, S.W., Kim, S., and Lee, C.S. Breakup and Atomization Characteristics of Mono-Dispersed Diesel Droplets in a Cross-Flow Air Stream. *International Journal of Multiphase Flow*, 32, pp. 807-822, 2006.

[59] Imamori, Y., Hiraoka, K., Murakami, S., Endo, H., Rutland, C.J., and Reitz, R.D. *Effect of Mesh Structure in the KIVA-4 Code with a Less Mesh Dependent Spray Model for DI Diesel Engine Simulations.* International Multidimensional Engine Modeling User's Group Meeting at the SAE CongressDetroit, MI, 2009.

[60] Lebas, R., Blokkeel, G., Beau, P.A., and Demoulin, F.X. Coupling Vaporization Model with the Eulerian-Lagrangian Spray Atomization (ELSA) Model in Diesel Engine Conditions. *SAE Technical Paper 2005-01-0213*, 2005.

[61] Lippert, A.M., Chang, S., Are, S., and Schmidt, D.P. Mesh Independence and Adaptive Mesh Refinement for Advanced Engine Spray Simulations. *SAE Technical Paper 2005-01-0207*, 2005.

[62] Xue, Q., Kong, S.C., Torres, D.J., Xu, Z., and Jianwen, Y. DISI Spray Modeling Using Local Mesh Refinement. *SAE Technical Paper 2008-01-0967*, 2008.

Appendix A Time Series of In-cylinder Flow Structure Development in Each Turbulence Model

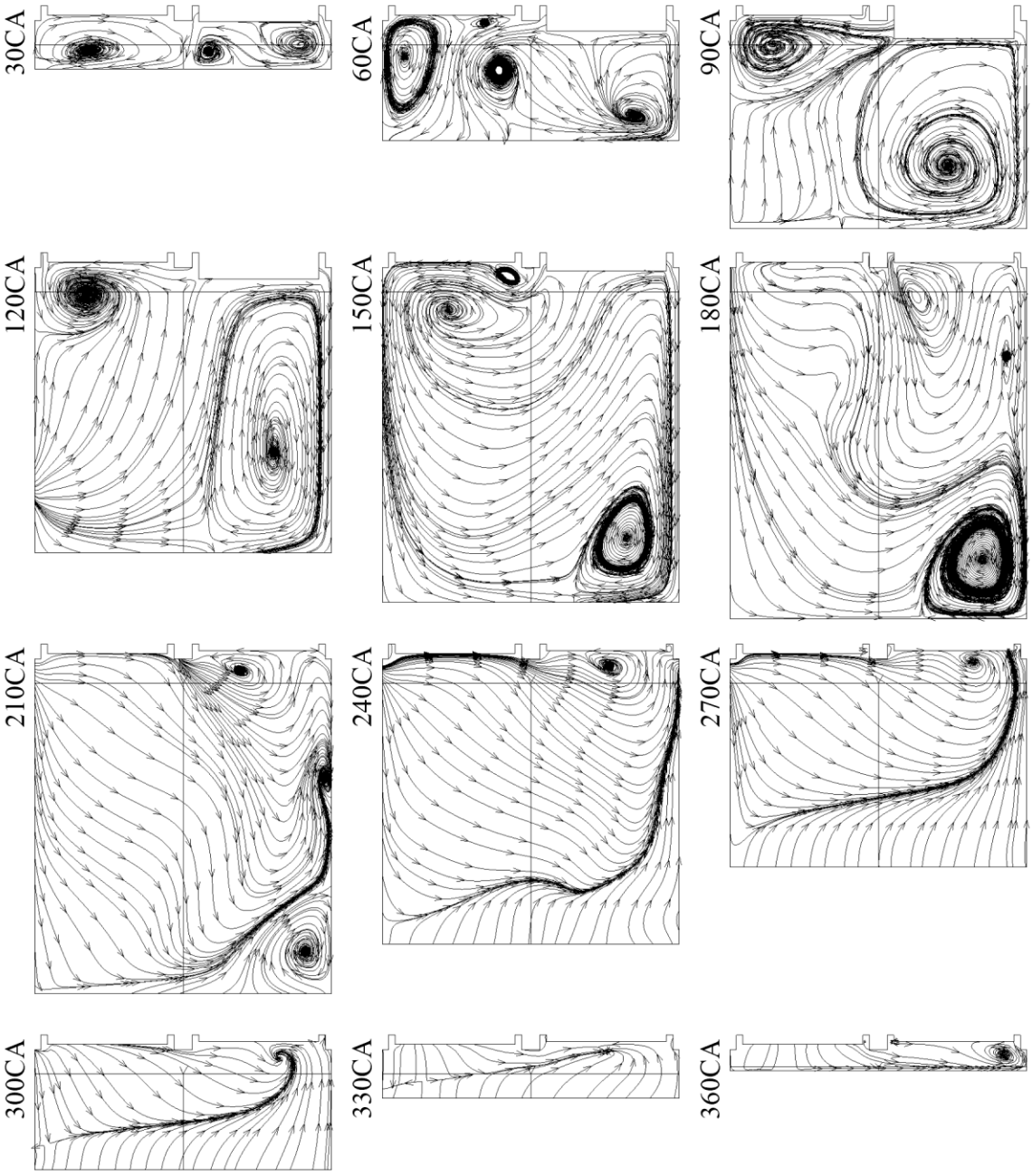

Figure A.1 – Naturally aspirated in-cylinder flow structure development by the standard k-ε model with coarse mesh

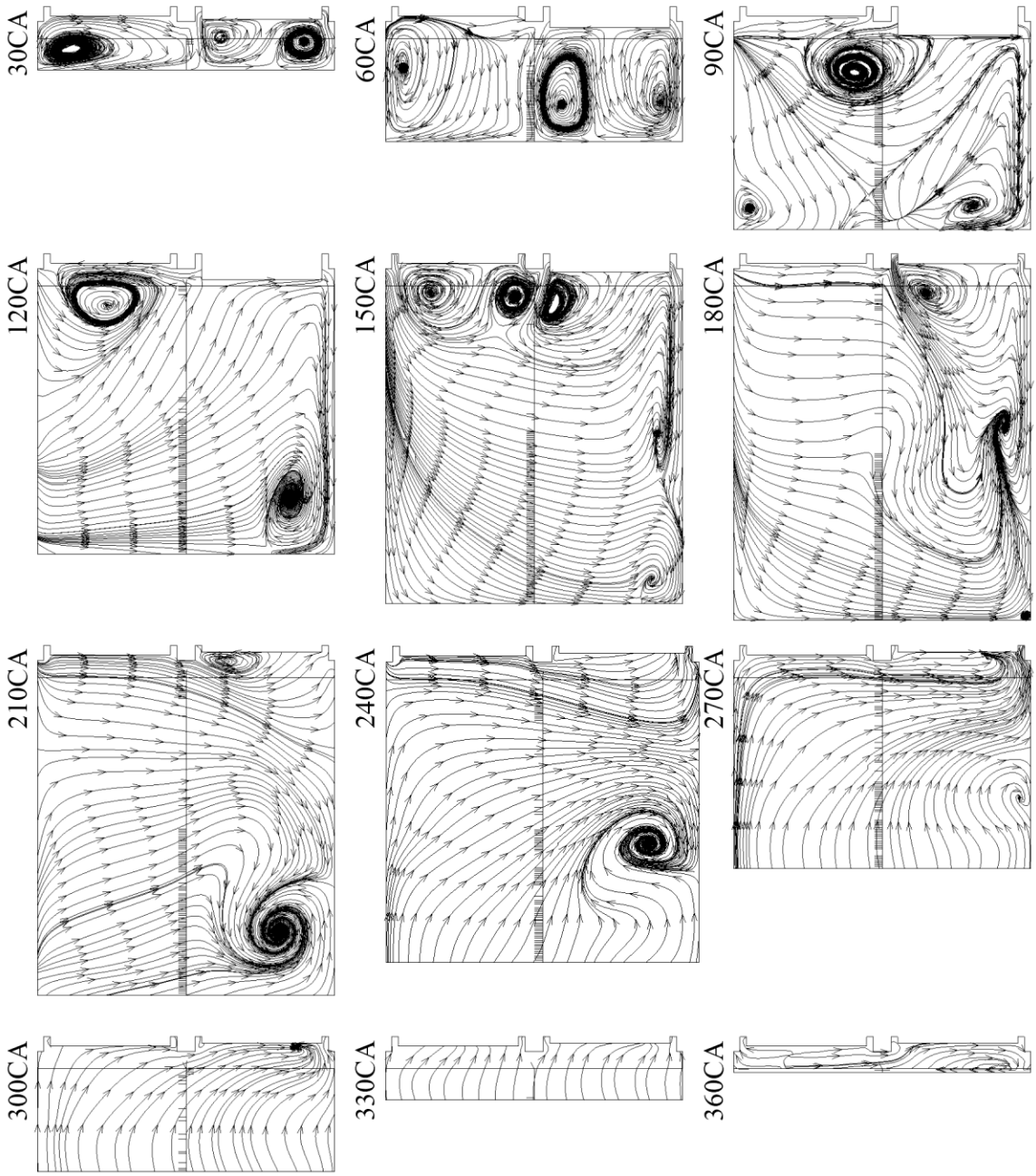

Figure A.2 – Naturally aspirated in-cylinder flow structure development by the standard k-ε model with refined mesh

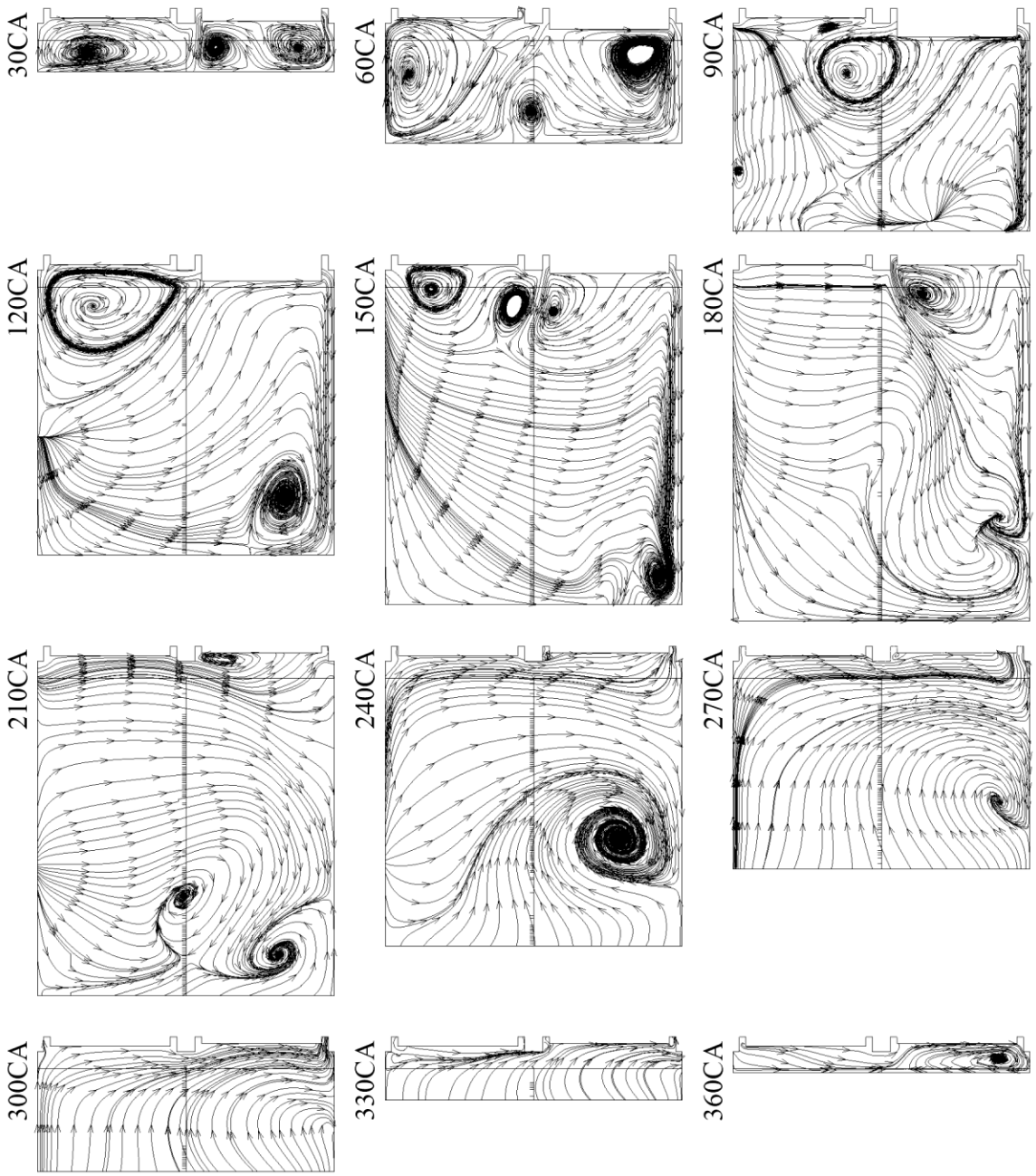

Figure A.3 – Naturally aspirated in-cylinder flow structure development by the standard k-ε model with fine mesh

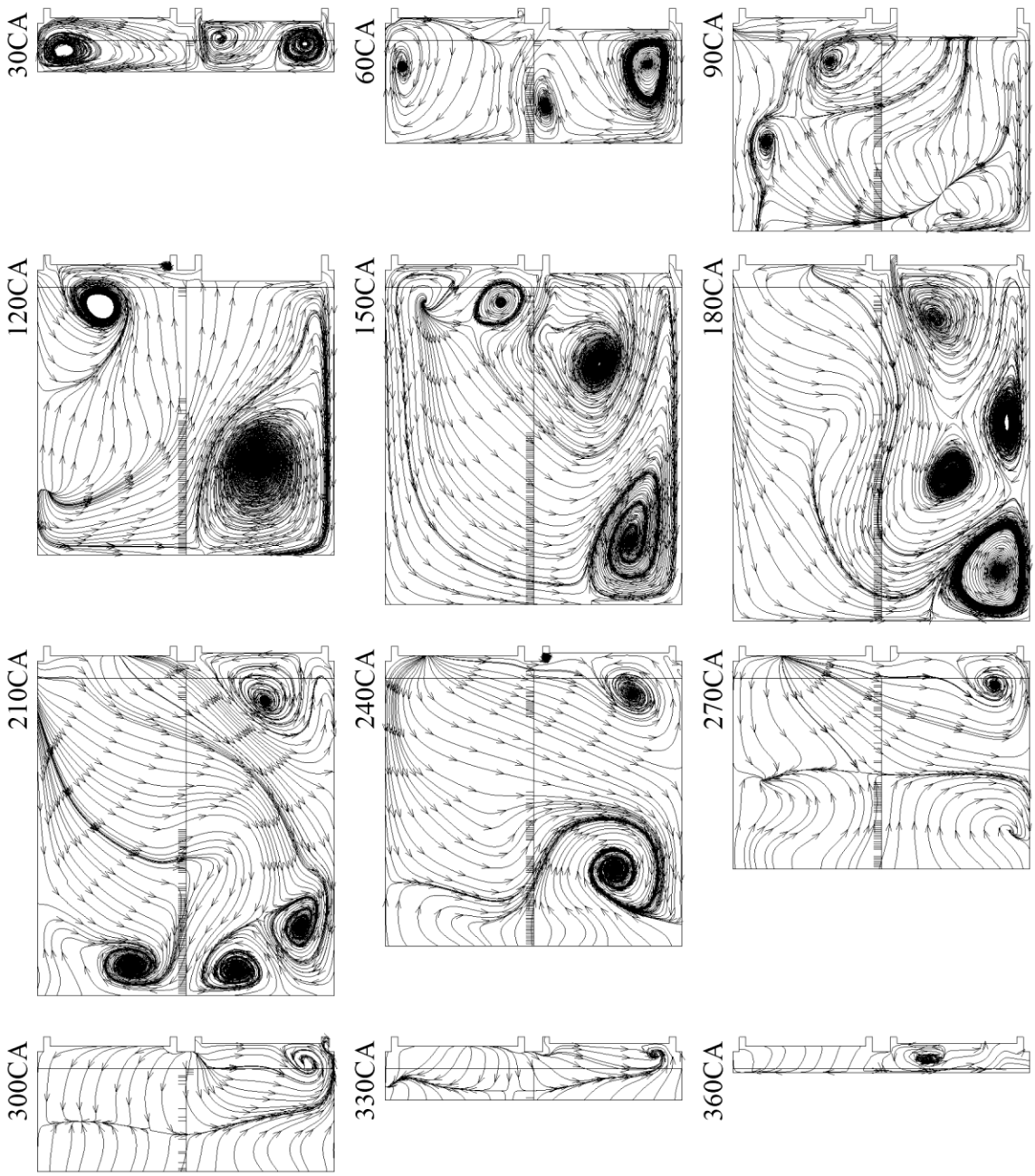

Figure A.4 – Naturally aspirated in-cylinder flow structure development by the RNG k-ε model with refined mesh

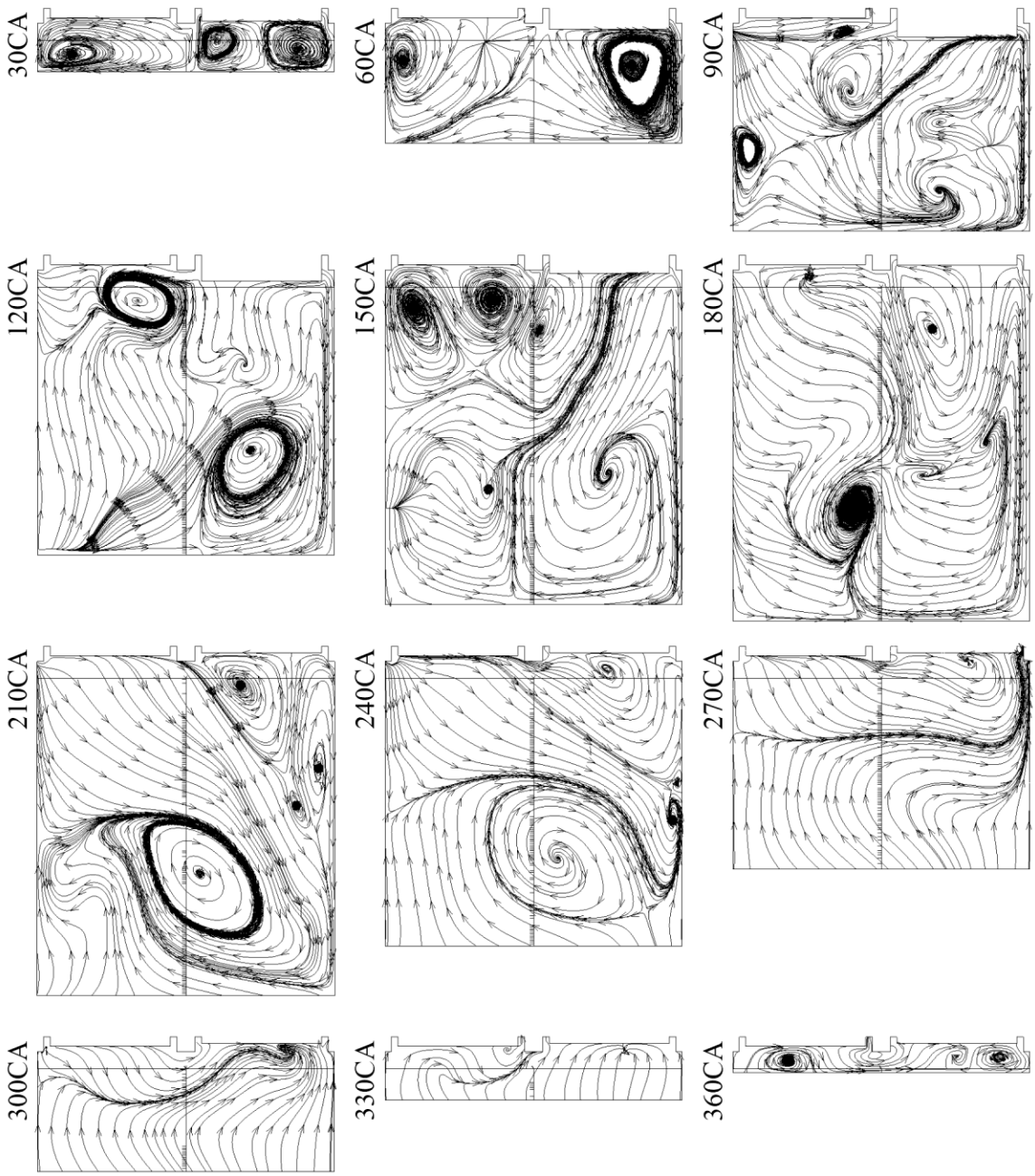

Figure A.5 – Naturally aspirated in-cylinder flow structure development by the RNG k-ε model with fine mesh

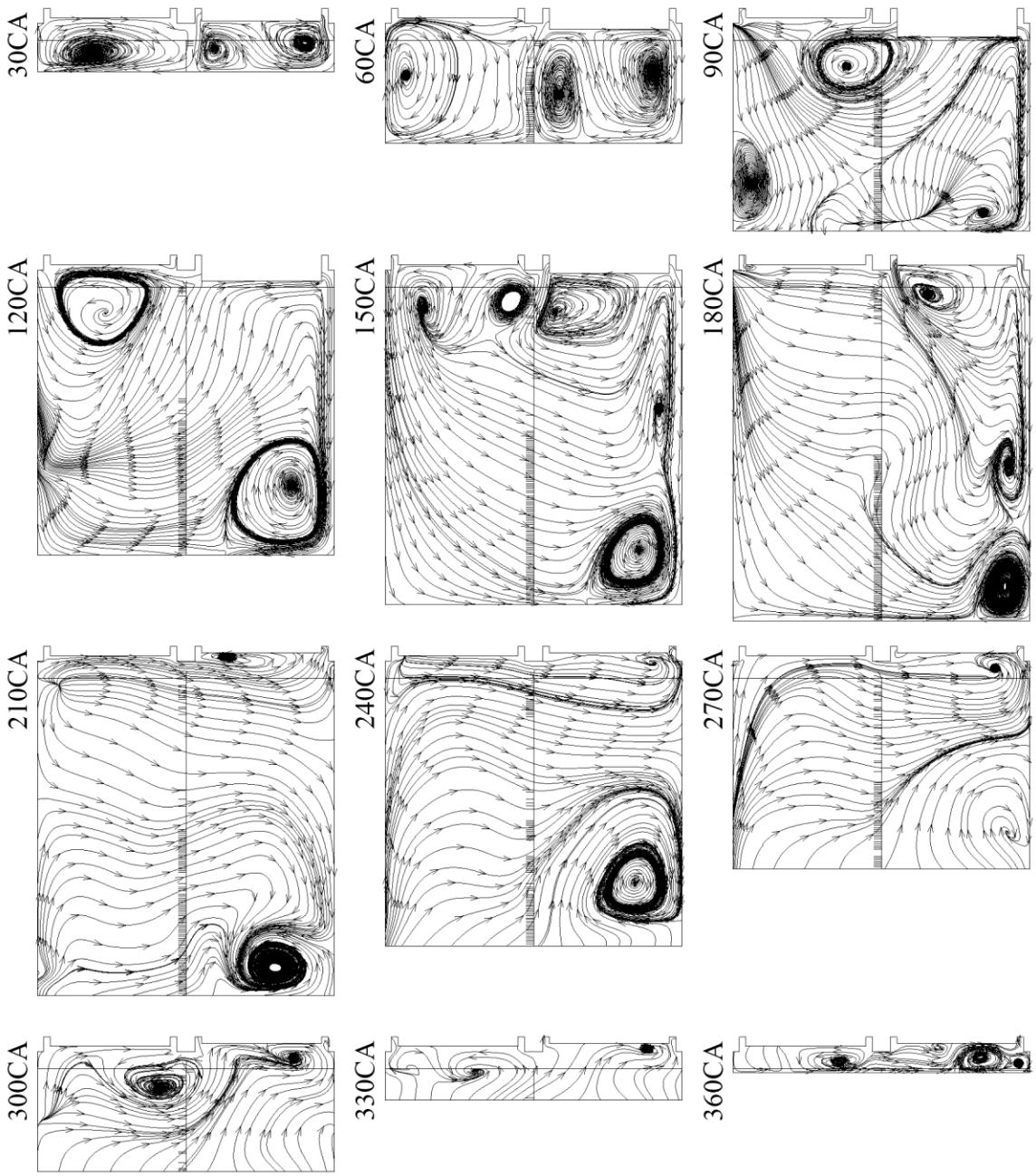

Figure A.6 – Naturally aspirated in-cylinder flow structure development by the standard k-ω model with refined mesh

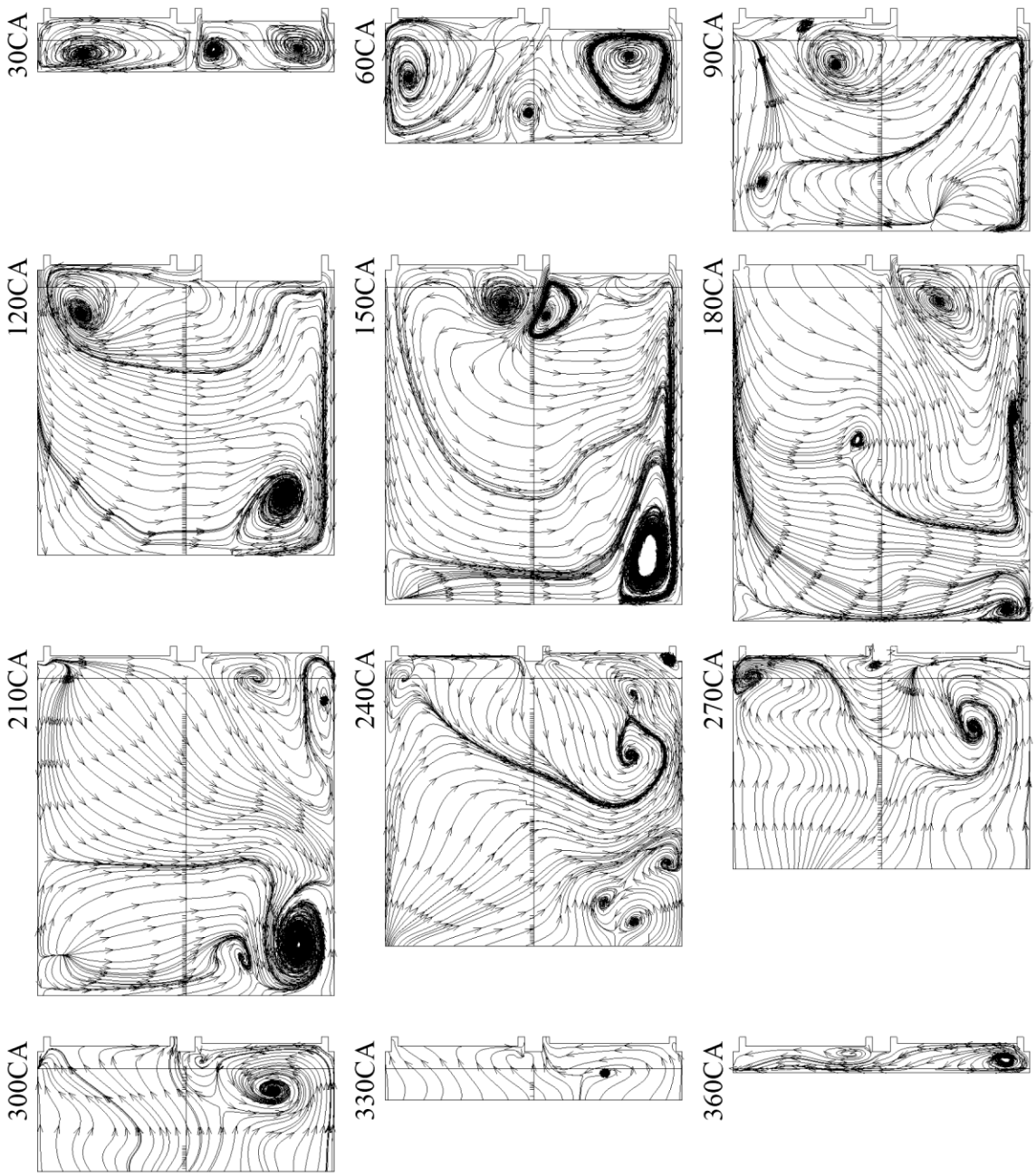

Figure A.7 – Naturally aspirated in-cylinder flow structure development by the standard k-ω model with fine mesh

Figure A.8 – Naturally aspirated in-cylinder flow structure development by the DES Spalart-Allmaras model with fine mesh

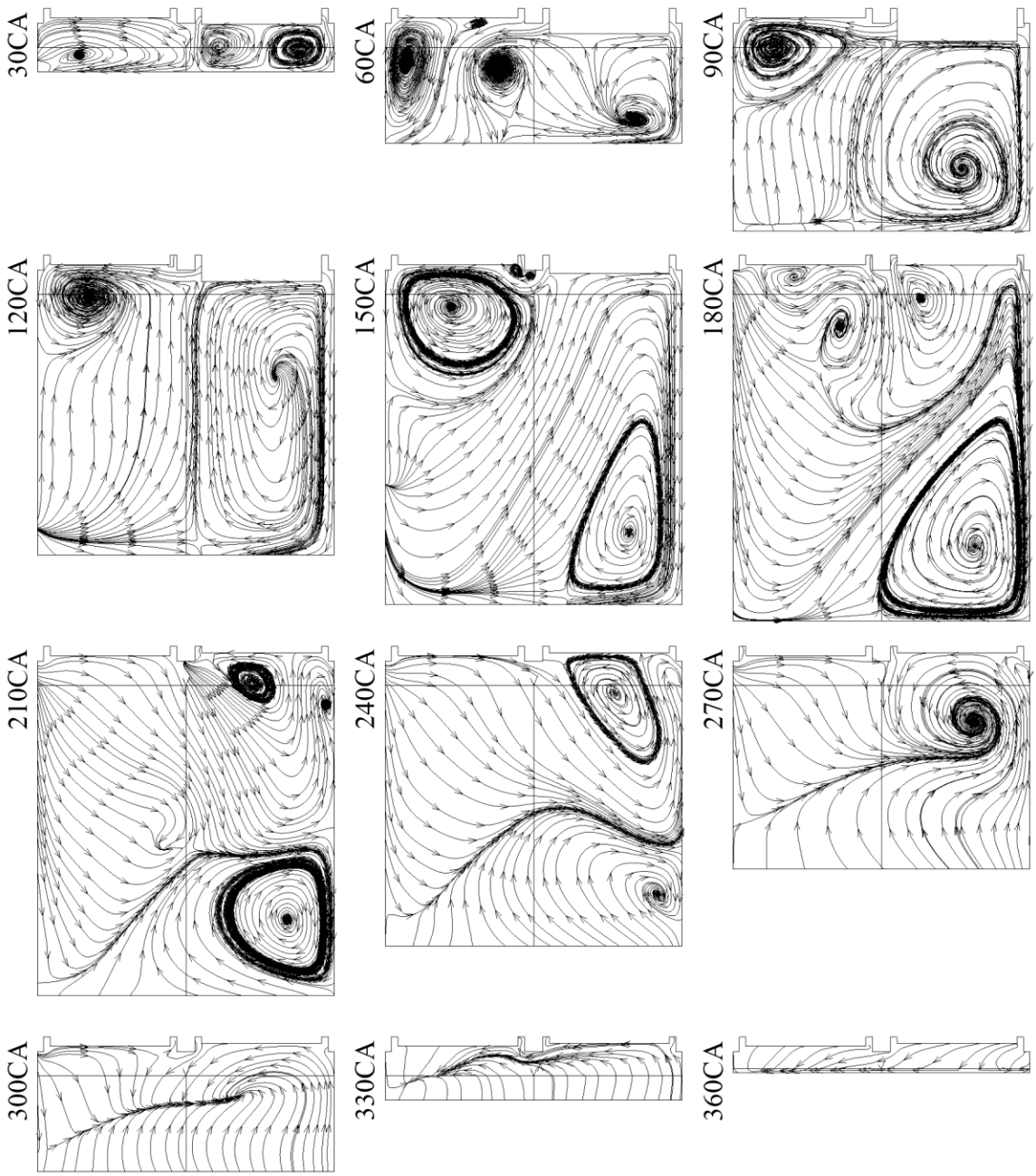

Figure A.9 – Turbocharged in-cylinder flow structure development by the standard k-ε model with coarse mesh

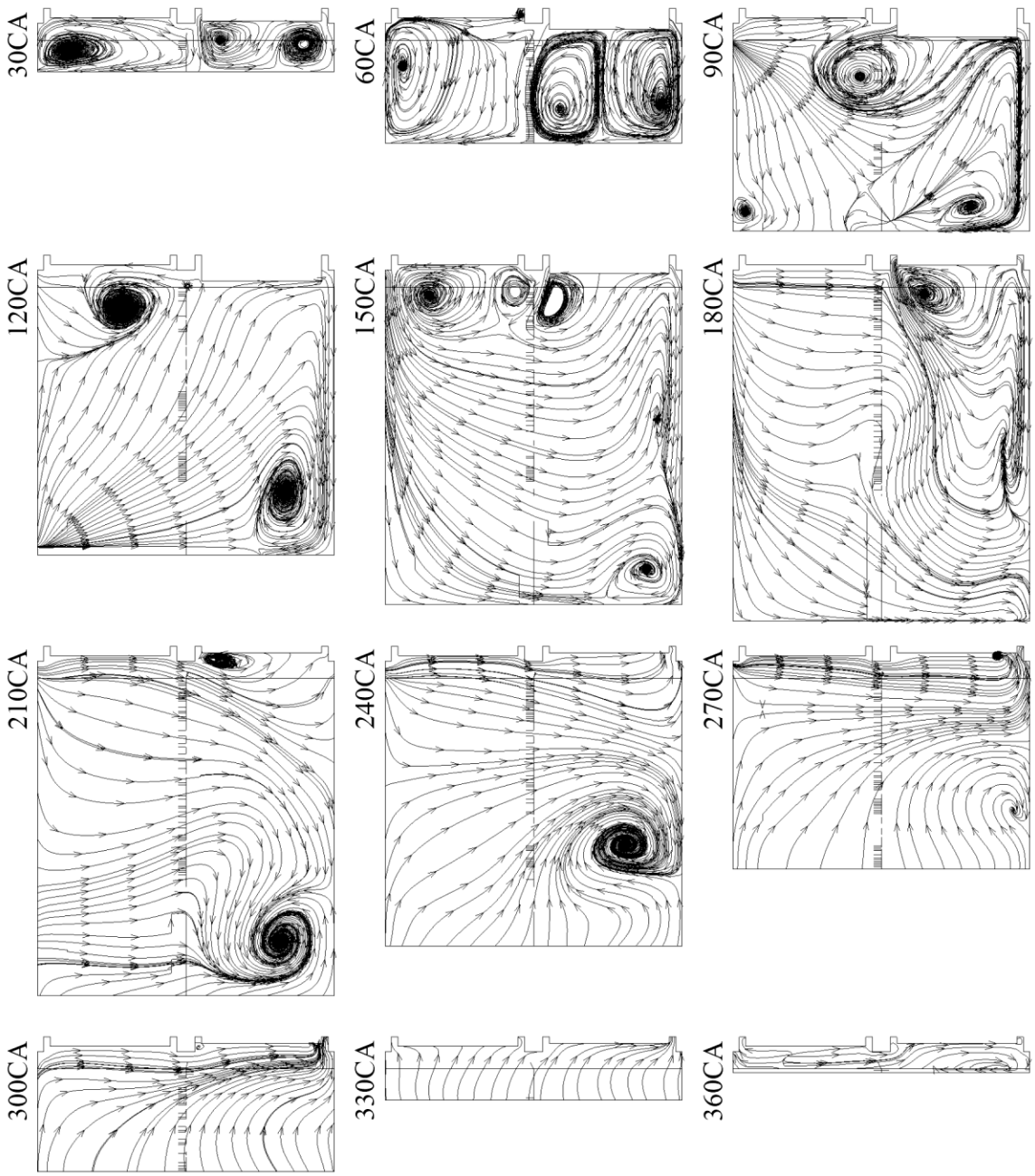

Figure A.10 – Turbocharged in-cylinder flow structure development by the standard k-ε model with refined mesh

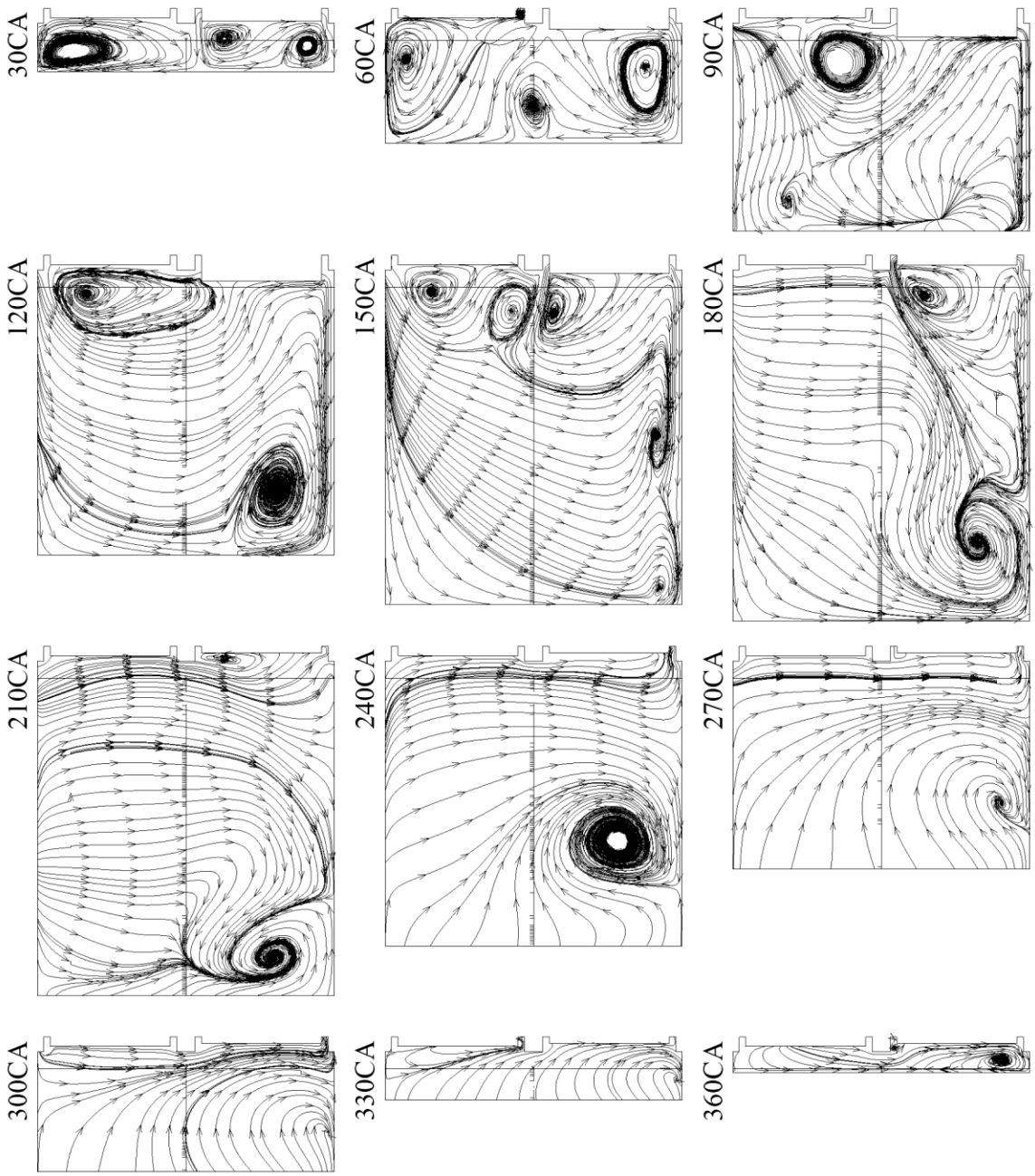

Figure A.11 – Turbocharged in-cylinder flow structure development by the standard k-ε model with fine mesh

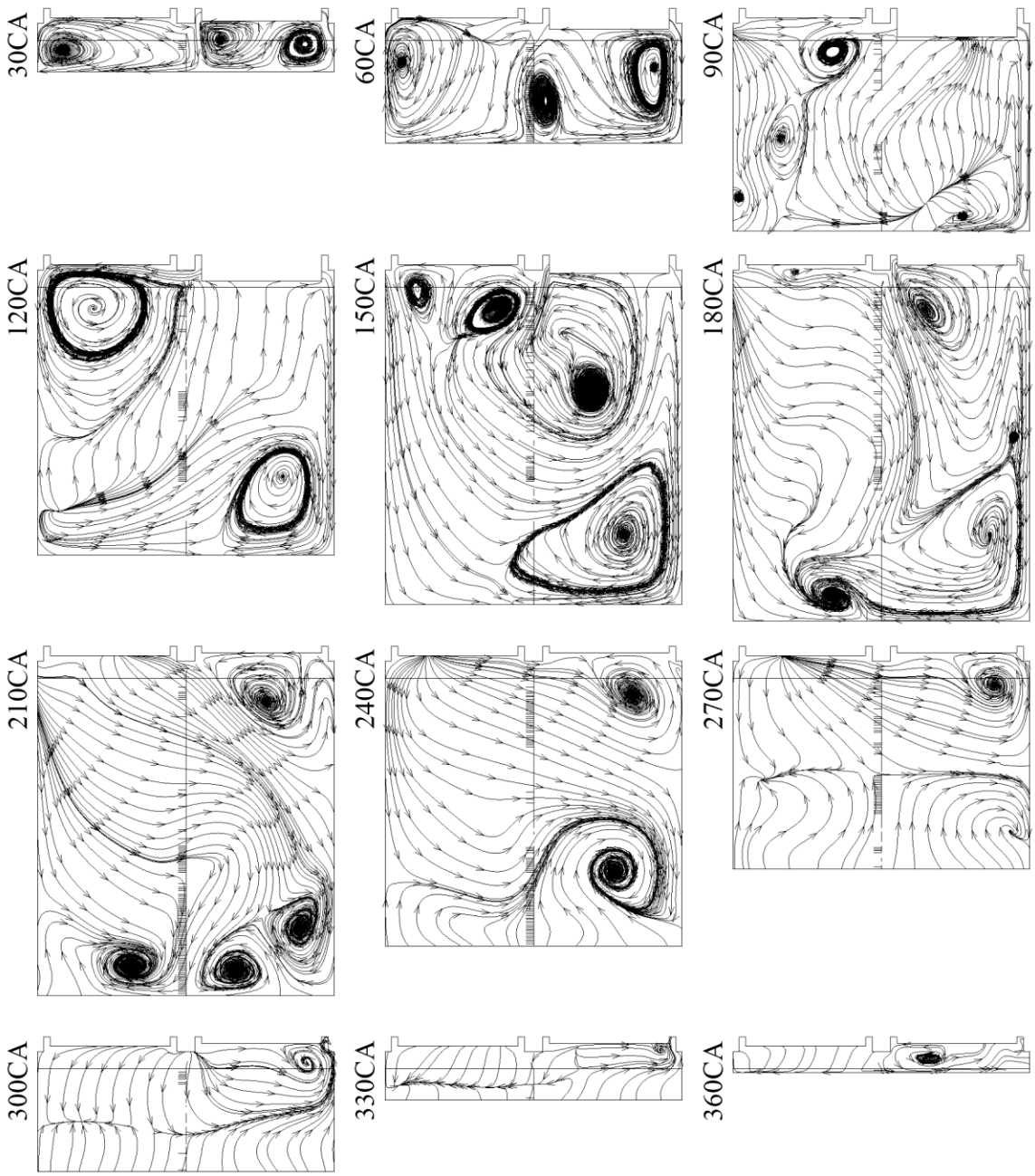

Figure A.12 – Turbocharged in-cylinder flow structure development by the RNG k-ε model with refined mesh

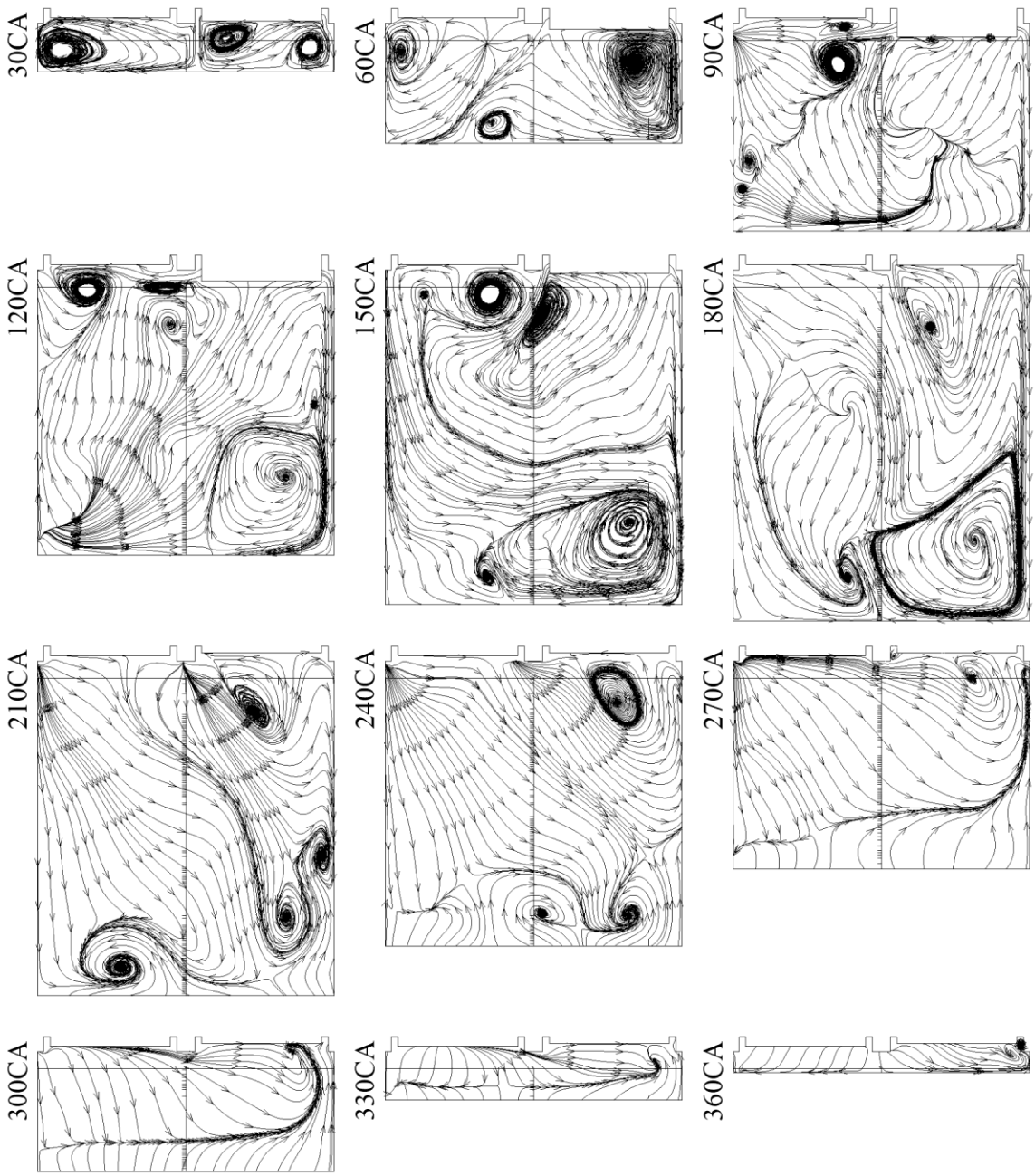

Figure A.13 – Turbocharged in-cylinder flow structure development by the RNG k-ε model with fine mesh

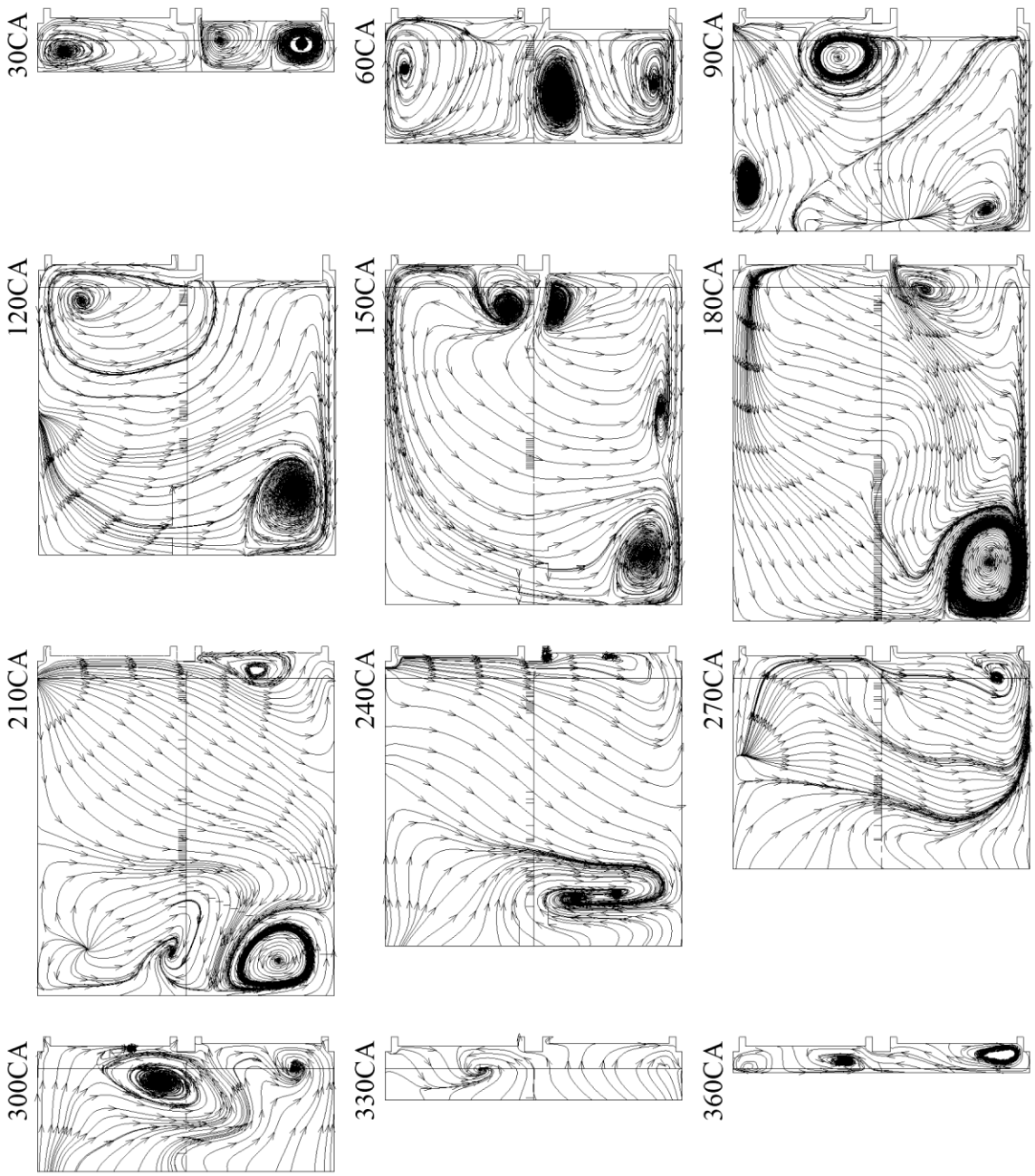

Figure A.14 – Turbocharged in-cylinder flow structure development by the standard k-ω model with refined mesh

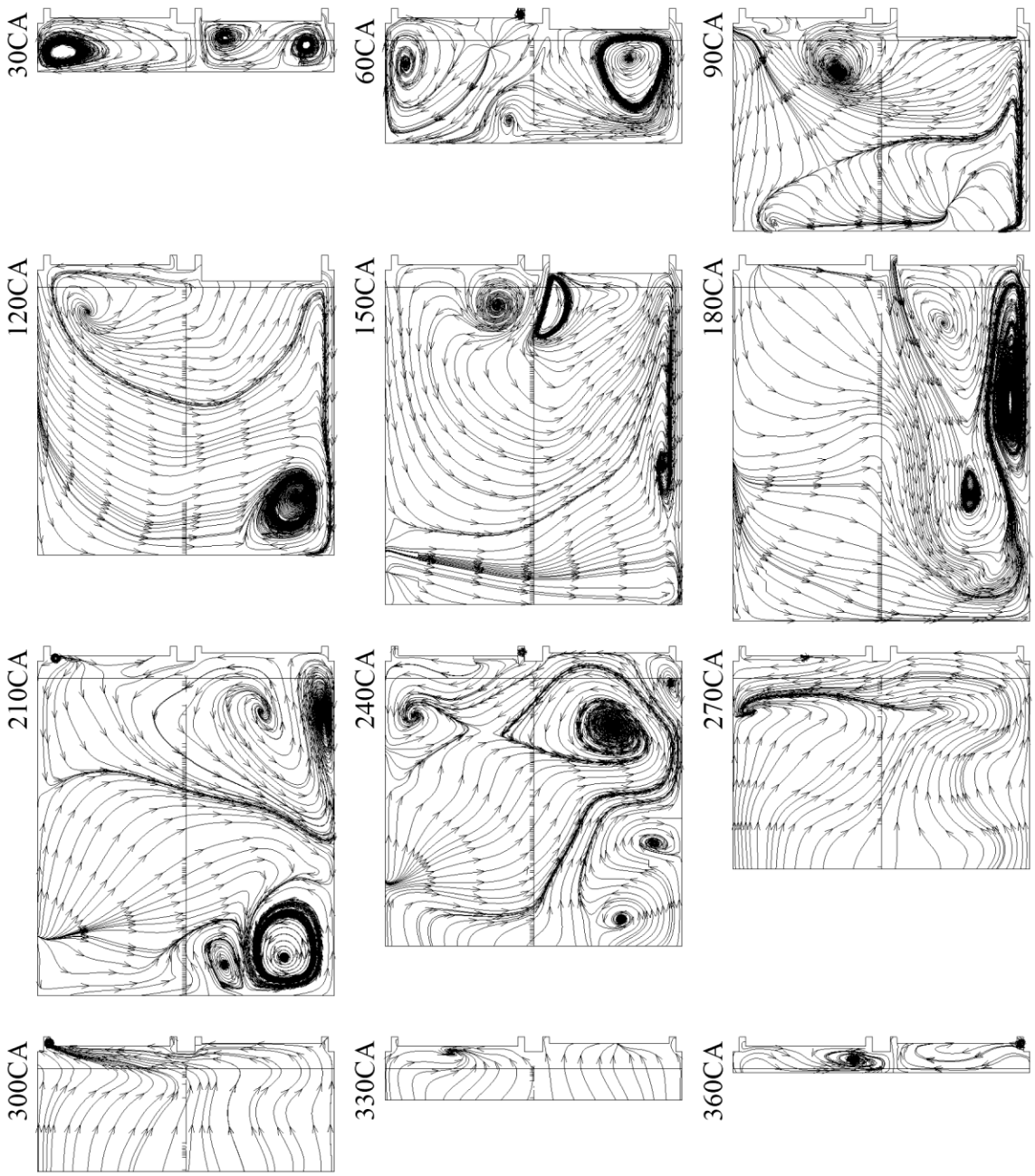

Figure A.15 – Turbocharged in-cylinder flow structure development by the standard k-ω model with fine mesh

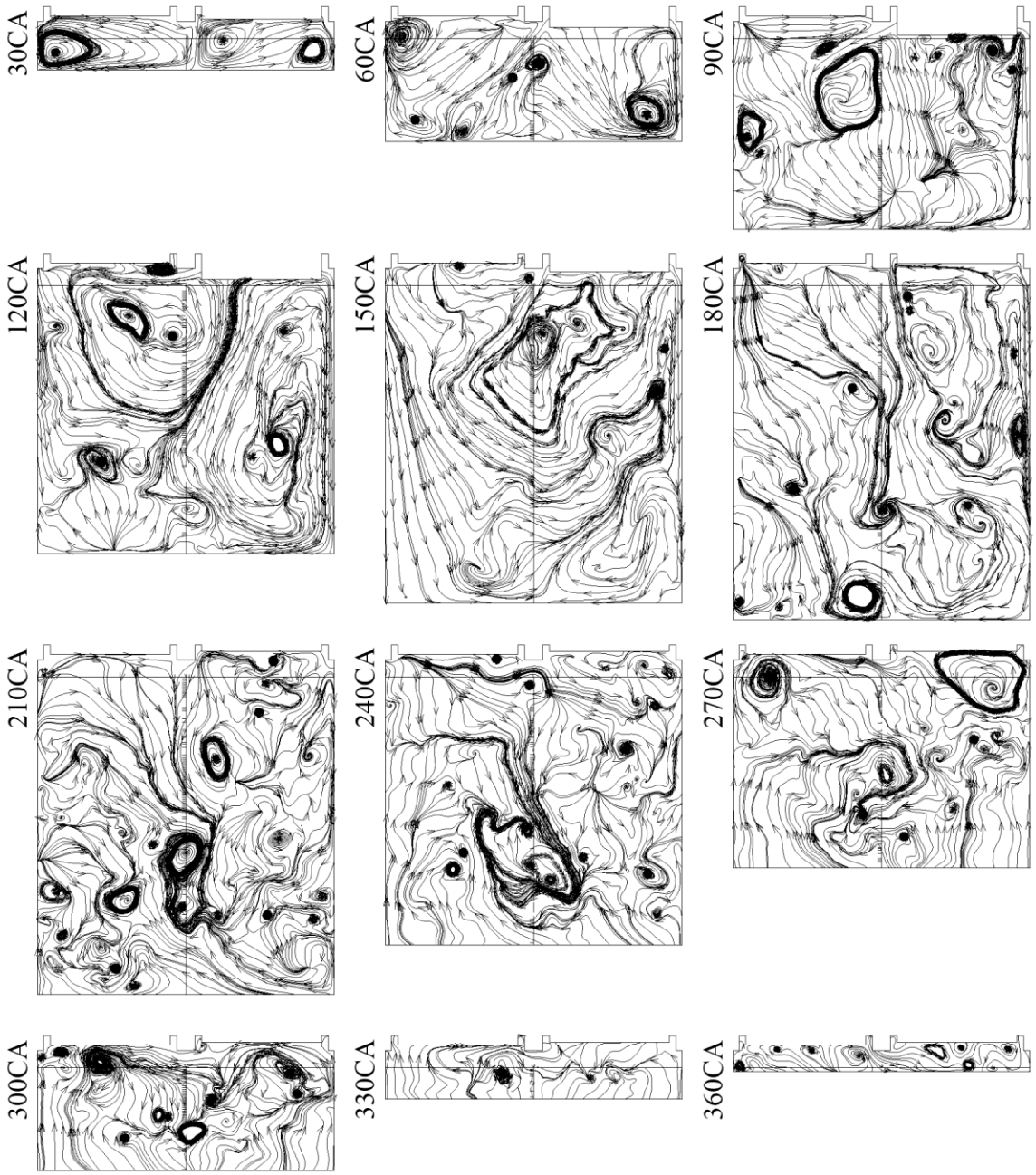

Figure A.16 – Turbocharged in-cylinder flow structure development by the DES Spalart-Allmaras model with fine mesh

Appendix B FLUENT In-Cylinder Model Setup Procedure

Due to the complexity of the geometry associated with moving boundaries, an engine simulation in FLUENT requires a lot of parameters to be set up. In this appendix, the configurations of in-cylinder models are discussed using one of the engine simulation cases utilized in the thesis work. Also, some useful tips in FLUENT are provided for this type of problem. The texts with border indicate an option selected from the FLUENT menu. Note that the following information is based on FLUENT 6.3. Some changes may have been made in the later versions. Please follow the manual by the developer.

B.1. Models

Main equations to be used to solve a problem are selected in this model definition. Models for chemical reactions, multiphase flow, discrete phases, etc., are activated here.

Define → Models → Solver…

Time: Unsteady

Define → Models → Viscous…

Model: k-epsilon (2 eqn.)

Define → Models → Energy…

Enable Energy Equation

B.1.1. Materials

Materials of fluids and solids can be defined here. FLUENT has a library of materials and a user can also modify these properties to adjust to a problem condition.

Name: air

Density: ideal-gas

B.1.2. Boundary Conditions

Groups of boundary types that were assigned in Gambit will be reflected as boundary conditions. If no boundary type was specified in Gambit, all boundaries will be set to wall.

Define → Boundary Conditions…

Set each boundary condition as follow.

- **inlet**

  pressure-inlet

    Gauge Total Pressure (pascal): 0 constant

    Supersonic/Initial Gauge Pressure (pascal): 0 constant

    Direction Specification Method: Direction Vector

    Coordinate System: Cartesian (X, Y, Z)

    X-Component of Flow Direction: 0 constant

    Y-Component of Flow Direction: -0.866 constant

    Z-Component of Flow Direction: -0.5 constant

  Turbulence

    Specification Method: Intensity and Hydraulic Diameter

    Turbulent Intensity (%): 1

    Hydraulic Diameter (mm): 23.64

  Thermal

    Total Temperature (k): 318 constant

Direction of inlet flow and hydraulic diameter is shown below.

Direction Specification Method

Direction of inlet flow is parallel to intake runner wall which has 30 degree angle to the horizontal plane. Therefore,

$$\mathrm{Y} = -\cos 30° = -0.866$$

$$\mathrm{Z} = -\sin 30° = -0.5$$

Hydraulic Diameter

Hydraulic diameter is defined as area divided by perimeter. Since the inlet is 33.522 mm high and 18.2375271916 mm wide, the hydraulic diameter will become,

$$D_h = \frac{4A}{P} = \frac{4 \times 33.522\text{mm} \times 18.2375271916\text{mm}}{2 \times 33.522\text{mm} + 2 \times 18.2375271916\text{mm}} = 23.64\text{mm}$$

- **outlet**

  pressure-outlet

  Momentum

  Gauge Pressure (pascal): 0 constant

  Backflow Direction Specification Method: From Neighbouring Cell

  Turbulence

  Specification Method: Intensity and Hydraulic Diameter

  Backflow Turbulent Intensity (%): 1

  Backflow Hydraulic Diameter (mm): 23.64

  Thermal

  Backflow Total Temperature (k): 318 constant

- **cylinder-head (Wall)**

  Thermal

  Thermal Conditions: Temperature

  Temperature (k): 360 constant

Using "copy to" option allows users to assign the same boundary conditions to all the other walls.

B.1.3. Grid Interface

Interfaces created in the pre-processor are connected in this section.

Define → Grid Interfaces…

Name	Interface Zone 1	Interface Zone 2
exhaust-interface	exhaust-interface-ob	exhaust-interface-ib
intake-interface	intake-interface-ob	intake-interface-ib

B.1.4. Dynamic Mesh

In-cylinder model is activated to specify engine configurations and to control the simulation by crank-angle instead of time. Piston position is also defined by crank-angle, connecting rod length and piston stroke. Piston stroke cutoff is specified if the piston layer were impaired by valves reaching into the layer. Cutoff is designed to move the piston layer by the number specified above; therefore, not allowing valves to cross the face between the piston layer and chamber zone.

Define → Dynamic Mesh → Parameters…

Enable Dynamic Mesh and In-Cylinder in Models list. Enable Smoothing, Layering, and Remeshing in Mesh Methods list. The detailed theory about dynamic meshing has been discussed in the subsections of Section 2.4.

Smoothing

Parameter	Value
Spring Constant Factor	0.9
Boundary Node Relaxation	0.2
Convergence Tolerance	0.001
Number of Iterations	20

Layering (Ratio)

Parameter	Value
Split Factor	0.4
Collapse Factor	0.4

Remeshing (Local Cell & Region Face)

Parameter	Value
Minimum Length Scale (mm)	0.5
Maximum Length Scale (mm)	0.7
Maximum Skewness	0.85
Maximum Cell Skewness	0.7
Size Remesh Interval	10

In-Cylinder

Parameter	Value
Crank Shaft Speed (rpm)	1500
Starting Crank Angle (deg)	360
Crank Period (deg)	720
Crank Angle Step Size (deg)	0.5
Piston Stroke (mm)	92.075
Connecting Rod Length (mm)	174
Piston Stroke Cutoff (mm)	2
Minimum Valve Lift (mm)	0.5

B.1.5. Valve Profile

Valve motion can be controlled by either User Defined Function (UDF) or a profile written in a certain format using any word processor. If a profile is used, the file extension has to be changed to ".prof". For instance, valve profile can be written as following:

```
((ex-valve 5 point)
(angle 240 270 300 330 360)
(lift 0 0.0038395 0.007679 0.0038395 0))
((in-valve point 5)
(angle 360 410 460 510 560)
(lift 0 0.0037185 0.007437 0.0037185 0))
```

The profile can be plotted by entering a command in Text User Interface (TUI) as,

```
> define/models/dynamic-mesh-controls

/define/models/dynamic-mesh-controls> icp

/define/models/dynamic-mesh-controls/in-cylinder-parameter> ppl
#f
Lift Profile:(1) [()] ex-valve
Lift Profile:(2) [()] in-valve
Lift Profile:(3) [()]
Start: [360]
End: [1080]
Increment: [10]
Plot lift? [yes]
```

B.1.6. Dynamic Mesh Zones

Each zone that is allocated to the dynamic mesh is set up in this section. Moving boundaries such as piston and valves are assigned to rigid body zone and the motions of them are specified by each profile. Piston-limit profile is selected if the cutoff is used. Deforming zones are used in the zone which experiences deformation by the result of the boundary motions.

Define → Dynamic Mesh → Zone…

Deforming

Zone Names	Type	Geometry Definition			Meshing Options		
chamber	Deforming	**Definition**			**Methods**	Smoothing and Remeshing	
		Cylinder Radius (mm)			**Zone Parameters**	**Minimum Length Scale (mm)**	0.5
		Cylinder Origin	**X**			**Maximum Length Scale (mm)**	0.7
			Y				
			Z			**Maximum Skewness**	0.8
		Cylinder Axis	**X**				
			Y				
			Z				
exhaust-interface-ob	Deforming	**Definition**	cylinder		**Methods**	Smoothing and Remeshing	
		Cylinder Radius (mm)		16.67	**Zone Parameters**	**Minimum Length Scale (mm)**	0.5
		Cylinder Origin	**X**	0		**Maximum Length Scale (mm)**	0.9
			Y	-21			
			Z	2.645		**Maximum Skewness**	0.6
		Cylinder Axis	**X**	0			
			Y	0			
			Z	1			
intake-interface-ob	Deforming	**Definition**	cylinder		**Methods**	Smoothing and Remeshing	
		Cylinder Radius (mm)		16.67	**Zone Parameters**	**Minimum Length Scale (mm)**	0.5
		Cylinder Origin	**X**	0		**Maximum Length Scale (mm)**	0.9
			Y	21			
			Z	3.025		**Maximum Skewness**	0.6
		Cylinder Axis	**X**	0			
			Y	0			
			Z	1			

Rigid Body

Zone Names	Type	Motion Attributes				Meshing Options
		Motion UDF/Profile	Valve/Piston Axis			Cell Heights (mm)
			X	Y	Z	
exhaust-stem-low	Rigid Body	ex-valve	0	0	1	0.5
exhaust-valve	Rigid Body	ex-valve	0	0	1	0.5
exhaust-valve-layer	Rigid Body	ex-valve	0	0	1	
exhaust-valve-side	Rigid Body	ex-valve	0	0	1	0.5
exhaust-valve-top	Rigid Body	ex-valve	0	0	1	0.5
intake-stem-low	Rigid Body	in-valve	0	0	1	0.5
intake-valve	Rigid Body	in-valve	0	0	1	0.5
intake-valve-layer	Rigid Body	in-valve	0	0	1	
intake-valve-side	Rigid Body	in-valve	0	0	1	0.5
intake-valve-top	Rigid Body	in-valve	0	0	1	0.5
piston	Rigid Body	piston-full	0	0	1	0.5
piston-layer	Rigid Body	piston-limit	0	0	1	

Stationary

Zone Names	Type	Meshing Options
		Cell Heights (mm)
cylinder-head:001	Stationary	0.6
default-interior:032 (interior between ex-port and exhaust-valve-layer)	Stationary	0.6

The cell heights in rigid body and stationary boundaries are critical for dynamic layering. The height may decide the order to generate a new layer of cells because it is assumed that FLUENT uses either the cell height of a stationary boundary (e.g., default-

interior:032) or moving boundary (e.g., exhaust-valve), and both cell heights could be set the same. To avoid the issue, it is recommended to run a mesh motion test beforehand.

B.1.7. Dynamic Events

Dynamic mesh events list activated and deactivated zones during the simulation. It is convenient to deactivate the port for which the valve is fully closed so that port cells are rejected from the calculation. However, this option is not available in parallel processing.

Define → Dynamic Mesh → Events…

Number of Events: 8

Name	Crank Angle	Setup Description	
ex-valve-open	240	**Type**	Create Sliding Interface
		Interface Name	exhaust-interface
		Interface Zone 1	exhaust-interface-ob
		Interface Zone 2	exhaust-interface-ib
in-valve-open	360	**Type**	Create Sliding Interface
		Interface Name	intake-interface
		Interface Zone 1	intake-interface-ob
		Interface Zone 2	intake-interface-ib
ex-valve-close	360	**Type**	Delete Sliding Interface
		Interface Name	exhaust-interface
in-valve-close	560	**Type**	Delete Sliding Interface
		Interface Name	intake-interface
active-exhaust-port	239	**Type**	Active Cell Zone
		Zone(s)	exhaust
deactivate-exhaust-port	361	**Type**	Deactivate Cell Zone
		Zone(s)	exhaust
active-intake-port	359	**Type**	Active Cell Zone
		Zone(s)	intake
deactivate-intake-port	561	**Type**	Deactivate Cell Zone
		Zone(s)	intake

For the above case, piston position at 360 degree is at Top Dead Centre (TDC) and the engine cycle starts from 360 degree. Moreover, it is not necessary to have the valves at fully closed position in the real engine case. The option of deactivating port zones is only functional when serial processing is utilized. It does not work out with parallel processing.

B.1.8. Controls

Relaxation factors, pressure-velocity coupling and discretization are to be set up.

Solve → Controls → Solutions…

Under-Relaxation Factors	
Pressure	0.1
Density	1
Body Forces	1
Momentum	0.7
Turbulent Kinetic Energy	0.8
Turbulent Dissipation Rate	0.8
Turbulent Viscosity	1
Energy	1
Pressure-Velocity Coupling	SIMPLE
Discretization	
Pressure	Standard
Density	First Order Upwind
Momentum	First Order Upwind
Turbulent Kinetic Energy	First Order Upwind
Turbulent Dissipation Rate	First Order Upwind
Energy	First Order Upwind

B.1.9. Initialization

Initial condition of flow domain needs to be defined before the calculation begins.

Solve → Initialize → Initialize…

Compute From	blank
Gauge Pressure (pascal)	0
X Velocity (m/s)	0
Y Velocity (m/s)	0
Z Velocity (m/s)	0
Turbulent Kinetic Energy (m2/s2)	0.01
Turbulent Dissipation Rate (m2/s3)	0.01
Temperature (k)	318

B.1.10. Execute Command

Execute command is a useful function to run commands at every specified iteration or time-step. For example, besides using the animation function in FLUENT, images of contours can be captured and saved to a directory in a variety of formats. Below is the list used to capture velocity vectors and contours of each section view at

every five time-step. Available commands can be found in the TUI manual or simply hit the Enter key to show options in the FLUENT console.

Solve → Execute Commands…

Defined Commands: 19

Name	Every	When	Command
command-1	5	Time Step	disp set-window 1
command-2	5	Time Step	disp set contours surfaces 37
command-3	5	Time Step	disp cont velo-mag 0 100
command-4	5	Time Step	disp view res-view view-1
command-5	5	Time Step	disp hard-copy "TEST-TDC10a-velo-mag-%t.tif"
command-6	5	Time Step	disp set-window 2
command-7	5	Time Step	disp surface-grid 37
command-8	5	Time Step	disp view res-view view-0
command-9	5	Time Step	disp hard-copy "TEST-TDC10a-gird-%t.tif"
command-10	5	Time Step	disp set-window 3
command-11	5	Time Step	disp set contours surfaces 38
command-12	5	Time Step	disp contour velo-mag 0 100
command-13	5	Time Step	disp view res-view view-xz
command-14	5	Time Step	disp hard-copy "TEST-TDC10a-velo-mag-xz-%t.tif"
command-15	5	Time Step	disp set-window 4
command-16	5	Time Step	disp set contours surfaces 39
command-17	5	Time Step	disp contour velo-mag 0 100
command-18	5	Time Step	disp view res-view view-xy
command-19	5	Time Step	disp hard-copy "TEST-TDC10a-velo-mag-xy-%t.tif"

By default, files will be stored on the desktop. By specifying a path for the save folder, for example, “C:\Users\NAME\Documents\3D ENGINE\Velocity-%t.tif”, all files will be saved to the directory specified. Note that files can only be saved in an existing folder. Also, it is required to change the setting of hardcopy to the set up done above.

File → Hardcopy…

Format	Coloring
TIFF	Color

Vita Auctoris

NAME:	Kohei Fukuda
PLACE OF BIRTH:	Sapporo, Japan
YEAR OF BIRTH:	1977
EDUCATION:	University of Windsor, Windsor
	2005-2008 B.A.Sc